

**STRUCTURE AND HYDRATION PROPERTY OF LOW
MOLECULAR WEIGHT HYALURONIC ACID BY
MOLECULAR DYNAMICS SIMULATIONS**



Mr. Panyakorn Taweecat

จุฬาลงกรณ์มหาวิทยาลัย
CHULALONGKORN UNIVERSITY

**A Thesis Submitted in Partial Fulfillment of the Requirements
for the Degree of Master of Science in Chemistry
Department of Chemistry
FACULTY OF SCIENCE
Chulalongkorn University
Academic Year 2019
Copyright of Chulalongkorn University**

โครงสร้างและสมบัติไฮดรเจนของกรดไฮยาลูโรนิกมวลโมเลกุลต่ำโดยการจำลองพลวัตเชิง
โมเลกุล



วิทยานิพนธ์นี้เป็นส่วนหนึ่งของการศึกษาตามหลักสูตรปริญญาวิทยาศาสตรมหาบัณฑิต
สาขาวิชาเคมี ภาควิชาเคมี
คณะวิทยาศาสตร์ จุฬาลงกรณ์มหาวิทยาลัย
ปีการศึกษา 2562
ลิขสิทธิ์ของจุฬาลงกรณ์มหาวิทยาลัย

ปัญญากร ทวีชาติ : โครงสร้างและสมบัติไฮเดรชันของกรดไฮยาลูโรนิกมวลโมเลกุล
ต่ำโดยการจำลองพลวัตเชิงโมเลกุล. (STRUCTURE AND
HYDRATION PROPERTY OF LOW MOLECULAR
WEIGHT HYALURONIC ACID BY MOLECULAR
DYNAMICS SIMULATIONS) อ.ที่ปรึกษาหลัก : ศ. ดร.พรเทพ
สมพรพิสุทธิ์

กรดไฮยาลูโรนิก (HA) เป็นโพลีเมอร์ของน้ำตาลโมเลกุลคู่ที่เชื่อมกันด้วยพันธะไกลโคซิดิกแบบบีตา (1,3) และบีตา (1,4) ซึ่งมีการประยุกต์ใช้งานอย่างแพร่หลายในทางการแพทย์ โภชนาการ และเครื่องสำอาง การศึกษาด้วยการจำลองพลวัตเชิงโมเลกุล (MD) ในสถานะสารละลายน้ำเปิดเผยถึงความผันแปรของคอนฟอร์เมชันที่มีความเกี่ยวข้องกับความยืดหยุ่นของการเชื่อมพันธะไกลโคซิดิกซึ่งขึ้นอยู่กับจำนวนหน่วยซ้ำของน้ำตาลโมเลกุลคู่ สายของ HA ที่มีความสั้นประมาณ 1-10 หน่วยจะดำรงอยู่ด้วยคอนฟอร์เมชันรูปแท่งที่มีความแข็งแกร่ง การเปลี่ยนแปลงคอนฟอร์เมชันจากรูปแท่งเป็นคอยล์อิสระถูกพบเมื่อสายของโมเลกุลยาวขึ้นประมาณ 20-50 หน่วย ผลการคำนวณจาก MD และ DFT แสดงให้เห็นว่าน้ำตาลโมเลกุลคู่ที่มีตัวเชื่อมแบบบีตา (1,4) มีความยืดหยุ่นของคอนฟอร์เมชันมากกว่าตัวเชื่อมแบบบีตา (1,3) การแปรผันของรัศมีไจเรชันและการผันผวนของคอนฟอร์เมชันแสดงให้เห็นว่า ตัวเชื่อมแบบบีตา (1,4) พร้อมด้วยความยาวของสาย HA เป็นสิ่งที่เพิ่มความโค้งงอของคอนฟอร์เมชันทั้งหมดและทำให้เกิดความยืดหยุ่นของสายพอลิเมอร์ นอกจากนี้พันธะไฮโดรเจนระหว่างโมเลกุลของน้ำตาลแล้ว ยังพบว่าไฮเดียมไอออนชอบที่จะยึดเหนี่ยวกับพันธะบีตา (1,4) มากกว่า ปริมาณน้ำที่ล้อมรอบโมเลกุล HA จะเพิ่มขึ้นตามความยาวของสาย HA แต่ปริมาณน้ำที่ล้อมรอบต่อหนึ่งหน่วยน้ำตาลโมเลกุลคู่จะยังคงมีปริมาณคงที่ ณ ความยาวต่างๆ นอกจากนี้การคำนวณพลังงานเสรีชี้ให้เห็นถึงกำแพงพลังงานศักย์สำหรับ HA ที่ต้องใช้เพื่อข้ามผ่านชั้นเมมเบรนของสิ่งมีชีวิต

สาขาวิชา เคมี

ลายมือชื่อนิติ

ปีการศึกษา 2562

ลายมือชื่อ อ.ที่ปรึกษาหลัก

6071961423 : MAJOR CHEMISTRY

KEYWORD: Hyaluronic acid, Low molecular weight, Molecular dynamic, DFT calculation, Conformation, Hydration, Membrane, Potential of mean force

Panyakorn Taweecat : STRUCTURE AND HYDRATION PROPERTY OF LOW MOLECULAR WEIGHT HYALURONIC ACID BY MOLECULAR DYNAMICS SIMULATIONS. Advisor: Prof. PORNTHEP SOMPORNPIST, Ph.D.

Hyaluronic acid (HA) is a biopolymer of disaccharide with two alternate glycosidic bonds, $\beta(1,3)$ and $\beta(1,4)$. It has a wide-range of applications in medicine, nutrition and cosmetics. A molecular dynamics (MD) study in aqueous condition presented here unveiled conformational variability in association with the flexibility of the glycosidic linkers, which depends on the number of disaccharide units. HA chain maintains a rigid rod-like conformation with short chain lengths i.e. with 1 to 10 disaccharide units. Crossover from a rod-like to a random-coil conformation is observed with increasing the chain length i.e. with 20-50 disaccharide units. MD and DFT calculations demonstrated that a disaccharide unit with the $\beta(1,4)$ linkage has more conformational flexibility than that with the $\beta(1,3)$ linkage. Variation of the radius of gyration and conformational fluctuation showed that the $\beta(1,4)$ linkers along with the HA chain length enhance the overall conformational flexibility and therefore elastic response of the polymer chain. Besides the inter-saccharide hydrogen bonding, Na^+ binds preferably at the $\beta(1,4)$ site. The hydration number of HA increases as an increase in the chain length while the hydration per disaccharide unit remains constant with the chain length. Moreover, free energy calculations indicated an energy barrier for HA transferring across biological membranes.

Field of Study: Chemistry
Academic Year: 2019

Student's Signature
.....
Advisor's Signature
.....

ACKNOWLEDGEMENTS

I would like to express the deepest appreciation to my advisor, Professor Dr. Pornthep Sompornpisut, for all his consultant and encouragement throughout this research. He taught me a lot of knowledge about computational chemistry including skills to solve the research problems.

I would like to thank Professor Dr. Ras B. Pandey, Department of Physics and Astronomy, University of Southern Mississippi, for his valuable suggestions in this research and contribution for our manuscript and publication.

In addition, I am grateful to thesis committee: Associate Professor Dr. Vudhichai Parasuk, Professor Dr. Supot Hannongbua, Associate Professor Dr. Somsak Pianwanit and Dr. Uracha Ruktanonchai for their comment to my thesis.

Finally, this work was support by Center of Excellence in Computational Chemistry (CECC) group and obtained the research fund from Development and Promotion of Science and Technology Talents Project (DPST).

Panyakorn Taweecat

TABLE OF CONTENTS

	Page
.....	iii
ABSTRACT (THAI)	iii
.....	iv
ABSTRACT (ENGLISH).....	iv
ACKNOWLEDGEMENTS.....	v
TABLE OF CONTENTS.....	vi
LIST OF TABLES.....	viii
LIST OF FIGURES	ix
CHAPTER 1 INTRODUCTION.....	1
1.1 Hyaluronic acid (HA).....	1
1.2 Applications of hyaluronic acid.....	2
1.3 Conformation of hyaluronic acid.....	3
1.4 Hydration of hyaluronic acid.....	6
1.5 Interaction between HA and phospholipid membrane	7
1.6 Inspiration of this research.....	9
1.7 Objectives of research.....	10
CHAPTER 2 THEORY.....	11
2.1 Molecular dynamics (MD) simulation.....	11
2.2 Steered molecular dynamics (SMD) simulation.....	14
2.3 Analysis from MD results.....	14
2.4 Density functional theory (DFT)	16
CHAPTER 3 METHODOLOGY.....	18
3.1 Computational software.....	18
3.2 Preparation of HA structure.....	19
3.3 MD simulations in vacuum.....	20

3.4 MD simulations in water	21
3.5 Transfer of HA across membranes	25
CHAPTER 4 RESULTS AND DISCUSSION.....	29
4.1 MD simulation in water	29
4.1.1 Conformational flexibility of the two glycosidic linkers	29
4.1.2 Structure and flexibilities of HA chains	35
4.1.3 Hydrations and solvation energy	39
4.1.4 Cation binding	41
4.1.5 Distribution of torsion angles	44
4.2 Transfer of HA across membranes	48
4.2.1 Stability of HA1 near the membrane center	48
4.2.2 Stability of HA1 near the lipid-water interface	49
4.2.3 Stability of HA5	50
4.2.4 Free energy of transfer of HA across membranes.....	51
CHAPTER 5 CONCLUSION.....	53
REFERENCES	55
APPENDICES	59
<i>Supplementary data</i>	59
<i>Publication from Current Trends in Polymer Science</i>	71
VITA.....	81

LIST OF TABLES

	Page
Table 1.1 Water content within the first hydration shell for various sizes of HA	6
Table 3.1 The simulated systems, initial structures, periodic boundary sizes and number of atoms for MD simulations.....	22
Table 3.2 The simulated systems, initial position of the HA center of mass, periodic boundary sizes and number of atoms for MD simulations.	27
Table 4.1 Distances and angles of inter-saccharide H-bonds at glycosidic bonds of HA1 obtained from MD simulations and from DFT geometry optimizations. X = H-bond donor or acceptor atoms.....	34
Table 4.2 Overlay structures before (blue) and after (green) optimization, H-bonds (dash lines), relative energies, net atomic charges and population ratios from 5 representative structure of the clusters.....	47

LIST OF FIGURES

	Page
Figure 1.1 Structure of hyaluronic acid	1
Figure 1.2 A guide of tissue formation by HA based scaffold [6].....	2
Figure 1.3 The rate of skin penetration at various sizes of HA [10].....	3
Figure 1.4 The four glycosidic torsion angles for elucidating conformation of HA	4
Figure 1.5 (a) Shape of HA in solid state with PDB code 2HYA [13].....	5
Figure 1.6 Decrease of radius of gyration for three type of HA20 [25]	5
Figure 1.7 Phase diagram of the HA–water system. (◆) DSC data; (x) sorption calorimetric data. The dashed line to the right side of the phase diagram corresponds to the sub-Tg endotherm. The phase boundary between the flexible polymer and the two- phase region, solution and crystals, is a nonequilibrium transition. [28].....	7
Figure 1.8 π/A –isotherms of DPPC on subphases containing sodium and calcium chloride ($[NaCl] = 155 \text{ mM}$, $[CaCl_2] = 10 \text{ mM}$). The concentration of HA was 0.5 mg /mL. [29].....	8
Figure 1.9 The MD trajectories: left-hand side shows HA (green) starting to be absorbed by vesicle (blue) and right-hand side shows HA absorbed completely by vesicle. The red points are phosphate groups in lipid structures. [30].....	9
Figure 1.10 A snapshot of a final stage of simulation with pulling forces presented as black arrows. The figure presents capstan-like mechanism of the soft matter HA-phospholipid system. [31].....	9
Figure 2.1 bond length (R^{AB}), bond angle (θ_{ABC}), improper angle or out-of-plane angle (χ) and torsion angle (ϕ_{ABCD}).....	12
Figure 2.2 Periodic boundary condition [34]	13
Figure 2.3 Criteria of H-bond between two molecules, θ is DHA angle.	15
Figure 3.1 Structures of (a) HA1- β (1,3) isomer (b) HA1- β (1,4) isomer (c) HA10 and (d) HA30 that are built by CHARMM software from PDB 2BVK structure (cyan, blue, red, and grey colors are carbon, nitrogen, oxygen and hydrogen, respectively. Structures were drawn by VMD 1.9.3).....	20

Figure 3.2 Model of HA20 solvated by water in rectangular box	21
Figure 3.3 (a) Model of HA5 in center of membrane and (b) Model of HA5 in membrane interface, yellow structure and blue point are lipid and water, respectively.	26
Figure 4.1 RMSD relative to the starting structure, RMSD and R _g as a function of time for HA1 chains for (a) $\beta(1,3)$ isomer and (b) $\beta(1,4)$ isomer.	30
Figure 4.2 The (ϕ , ψ) distribution plots showing the favorable region of the conformation at glycosidic linkages (a) $\beta(1,3)$ linkage and (b) $\beta(1,4)$ linkage, both graph were extracted from 10,000 snapshots of HA1 and the populated fraction is indicated by contour colors.	31
Figure 4.3 The occupancies of H-bonds between two saccharide rings connected together via glycosidic bonds of HA1 (displayed in stick representation) (a) $\beta(1,3)$ and (b) $\beta(1,4)$ isomers.	32
Figure 4.4 (a) and (b) show the structure fluctuations during the simulations of HA5 and HA30, respectively.	36
Figure 4.5 (a) The ratio of the R _g of equilibrated structures to the straight-chain conformation (b) The linear regressions between $\ln R_g$ and $\ln N$ (N = units of HA) fitted with two datasets: HA1-HA20 and HA20-HA50.	37
Figure 4.6 (a) The average RMSF compared to average structure of HA from last 20 ns for all systems. (b) The occupancies of the $\beta(1,3)$ and $\beta(1,4)$ major H-bonds for all HA systems.	38
Figure 4.7 The normalized radial pair distribution functions between all sizes of HA and water that were calculated by (a) hydrogen of water and oxygen of HA and (b) oxygen of water and hydrogen from hydroxy group of HA. (c) The number of hydrated water molecules per disaccharide unit and free energies of solvation of HA per disaccharide unit	40
Figure 4.8 The radial pair distribution functions of (a) Na-COO of HA and (b) Na-OH of HA of all studied systems.	41
Figure 4.9 (a) Na-COO and Cl-COO for HA50 (b) The numbers of Na ⁺ per disaccharide unit counted within 3 Å of HA, the value of HA1 is mean from both isomers.	42
Figure 4.10 The binding mode of the $\beta(1,3)$ (a) and $\beta(1,4)$ (b) isomers to Na ⁺ . (c) The percent proportion of Na ⁺ found within 5 Å of glycosidic oxygen atom.	43

Figure 4.11 The (ϕ , ψ) distribution of all positions of $\beta(1,4)$ linker of (a) HA5 (50,000 data) and (b) HA40 (400,000 data) (c) Representative conformations of region A, B, C and D.	45
Figure 4.12 (a) Plots of z-position of the center of mass of examined molecules as a function of time and (b) the magnified graph showing the first 100 ps from figure (a) including 200 ps from equilibration step, the initial position of the molecules was set at center of membrane. The center of mass of phospholipid bilayers were the origin of the coordinate and the membrane region corresponds to the distance values between -20 to +20 Å.	49
Figure 4.13 Plots of z-position of the center of mass of focused organic as a function of time, the initial position of organic molecules was set at phosphate group or membrane surface (partial membrane region). The center of mass of phospholipid bilayers were the origin of the coordinate and the membrane region corresponds to the distance values between -20 to +20 Å.	50
Figure 4.14 Plots of z-position of the center of mass of HA5 as a function of time, the initial positions of HA5 was set at center of membrane (black color) and phosphate group or membrane surface (red color). The center of mass of phospholipid bilayers were the origin of the coordinate and the membrane region corresponds to the distance values between -20 to +20 Å.	51
Figure 4.15 PMF of benzene, limonene and HA1	52

CHAPTER 1

INTRODUCTION

1.1 Hyaluronic acid (HA)

Hyaluronic acid (HA), also known as hyaluronan is a naturally occurring linear polysaccharide of a glycosaminoglycan class with its molecular weight ranging from 10^4 to 10^7 units [1-2]. HA can be found in some bacteria and most of connective tissues of higher type of animals including humans. It is naturally synthesized by Class I hyaluronan synthases [3]. The repeating units are disaccharides consisting of β -D-glucuronic acid (GlcA) and β -D-N-acetylglucosamine (GlcNAc) joined alternately by $\beta(1,3)$ and $\beta(1,4)$ glycosidic bonds (Figure 1.1) [4]. So, HA is a polymer with unbranched chain.

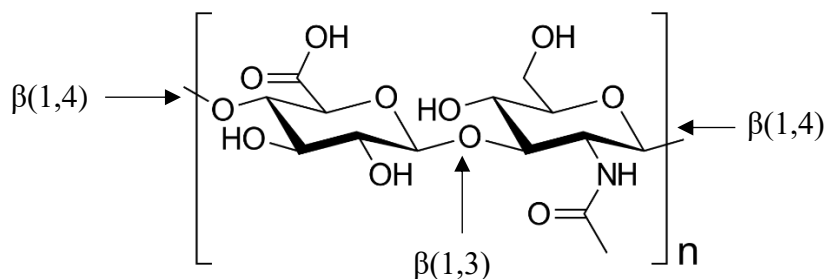


Figure 1.1 Structure of hyaluronic acid

Hyaluronic acid plays a significant role in a variety of biological processes, including cell signaling, wound healing, tissue regeneration, morphogenesis, matrix organization and pathobiology. It is an important component of skin, cartilage, connective, epithelial, and neural tissues. Its unique physico-chemical properties such as biocompatibility, biodegradability and high water retention have made hyaluronic acid an ideal substance used in medical, pharmaceutical, nutritional and cosmetic applications [4-6].

1.2 Applications of hyaluronic acid

The roles of HA for tissue formation and wound healing have been applied in tissue engineering based on scaffold function [6]. The scaffold is defined as a temporary supporting material for growing cell and tissues [7]. HA structure can perform a porous scaffolding material that works together with growth factors and bioactive signals to provide the mechanical support for tissue growth (Figure 1.2). There have been many fabrications of HA based scaffolding materials by chemical modifications and crosslinking of HA for medical applications [8].

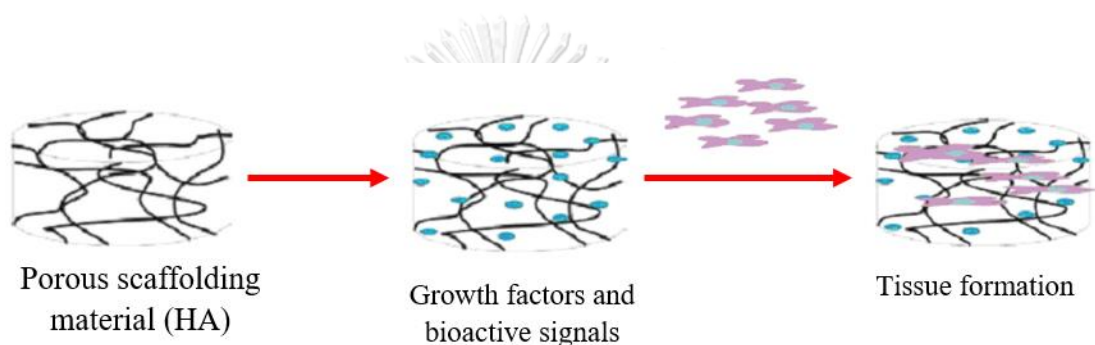


Figure 1.2 A guide of tissue formation by HA based scaffold [6]

Another property of HA is the excellent water adsorption ability because HA is highly hydrophilic due to the presence of abundant acid (COO⁻) and hydroxyl (OH⁻) groups in disaccharide units. So, HA is a key ingredient in many moisturizers, skincare products and other cosmetics [9-10]. The mass production of HA for commercial or industrial applications is done by using bacteria biosynthesis, animal tissues or the cell-free technologies [11]. In 2008, Farwick and group studied the effect of HA size to membrane permeation property [10]. They found HA with lower than 50 kDa or low molecular weight HA (LMW-HA) have the best skin penetration (Figure 1.3), the first and second bar graphs were measured after 5 and 22 hours, respectively. In addition, they also studied the anti-wrinkle effect. They tested by applying HA to human faces for 8 weeks and measured the disappearance of wrinkle. HA with size 50 kDa also have the best elimination of wrinkle.

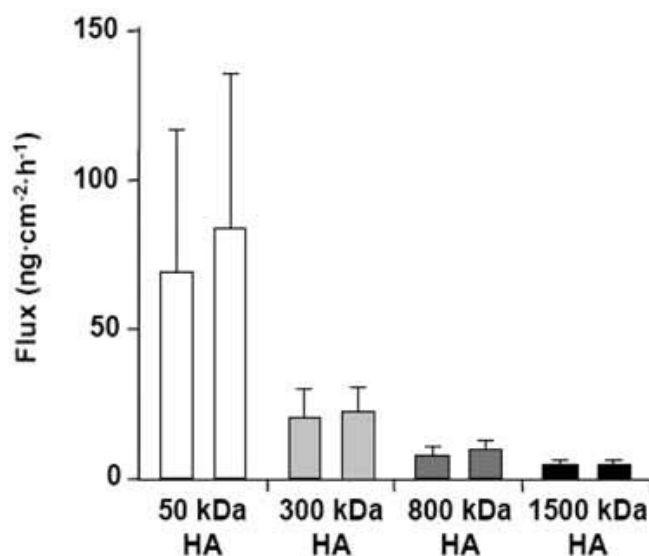


Figure 1.3 The rate of skin penetration at various sizes of HA [10]

1.3 Conformation of hyaluronic acid

Structures of HA have been studied over many years because they provide the fundamental basis for investigating functional mechanisms and biological activities related to health and diseases. The first successful information about atomic structure of HA was reported by Atkins and group in 1972 [12-13]. They studied the solid-state conformation of HA 4 units in acid form by using X-ray diffraction. The crystal structure indicated the extended 2-fold helical shape. After that, they studied the ionized form of HA with different counter ions. If cations are sodium or potassium ions, the shape of HA will be left-handed 4-fold helix. And the shape will change to left-handed 3-fold helix for calcium ion [14]. Thus, pH of solution and type of cations influence to conformation of HA.

There were several publications studying three dimensional structure of HA in solution by using NMR spectroscopy for experiment and molecular dynamics (MD) simulations for theoretical studies [15-17]. Some researches studied the conformation by Monte-Carlo simulation [18] and quantum mechanical methods [19-20]. According to several researches, the glycosidic bonds of HA adopt conformations with preferred ranges in the ϕ and angles, Figure 1.4 analogous to the Ramachandran plot of protein backbone torsions.

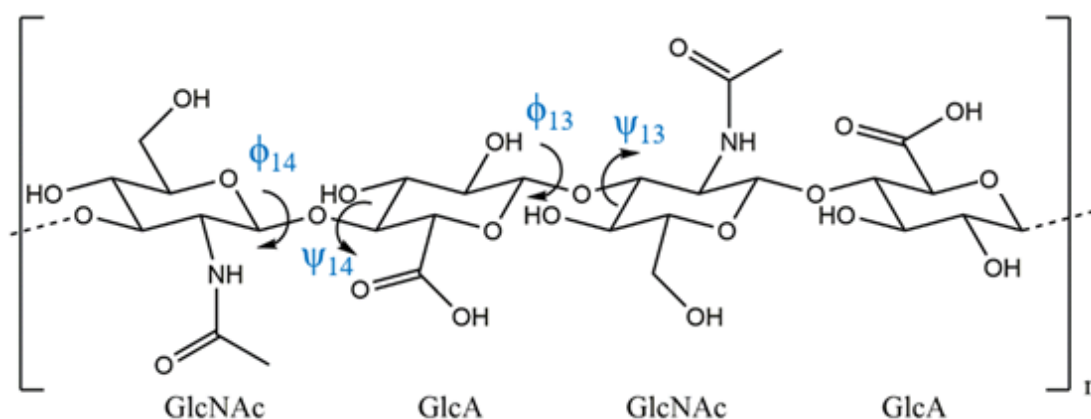


Figure 1.4 The four glycosidic torsion angles for elucidating conformation of HA

$\phi_{13} = \text{H1(GlcA)-C1(GlcA)-O-C3(GlcNAc)}$, $\psi_{13} = \text{C1(GlcA)-O-C3(GlcNAc)-H3(GlcNAc)}$, $\phi_{14} = \text{H1(GlcNAc)-C1(GlcNAc)-O-C4(GlcA)}$ and $\psi_{14} = \text{C1(GlcNAc)-O-C4(GlcA)-H4(GlcA)}$, where GlcA is glucuronic acid and GlcNAc is N-acetylglucosamine

In 2006, Almond and group proposed the conformation of HA with 4 disaccharide units in solution by combining data from NMR spectroscopy and MD simulations [21]. They reported the structure with PDB code, 2BVK. The structure also had left-handed 4-fold helical shape but it's more flexible than solid-state structure (Figure 1.5). The average dihedral angles at glycosidic bond from 2BVK structure are $(\phi_{13}, \psi_{13}) = (50.7^\circ, 9.7^\circ)$ and $(\phi_{14}, \psi_{14}) = (47.9^\circ, 8.0^\circ)$. However, the radius of gyration (R_g) per disaccharide monomer unit decreases as the HA chain length increases and HA conformations adopt non-linear form [22-24]. At high molecular weights, HA takes on the form of random coiled conformation. Cilurzo and group showed R_g of three type of HA with 20 disaccharide units (HA20) decrease during MD simulations [25]. HA20S5 and HA20S20 from Figure 1.6 are derivatives of HA20 modified by adding sulfate groups at carboxylate groups with 5 and 20 degrees of modification, respectively. They also studied skin permeation of HA by using Confocal Laser Scanner Microscopy (CLSM) and the results illustrated that HA20 are better than HAs with higher sizes.

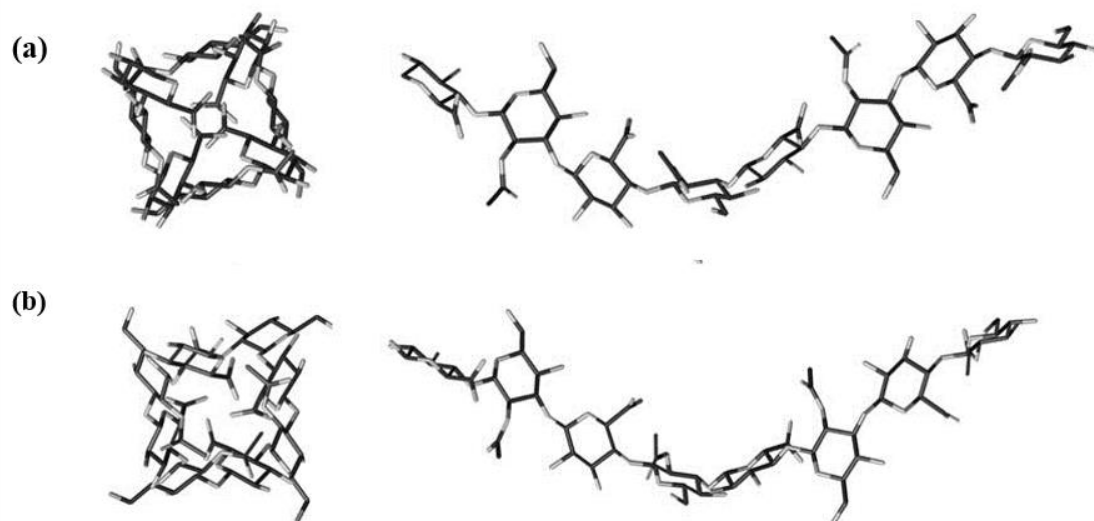


Figure 1.5 (a) Shape of HA in solid state with PDB code 2HYA [13]

(b) Shape of HA in solution with PDB code 2BVK [21]

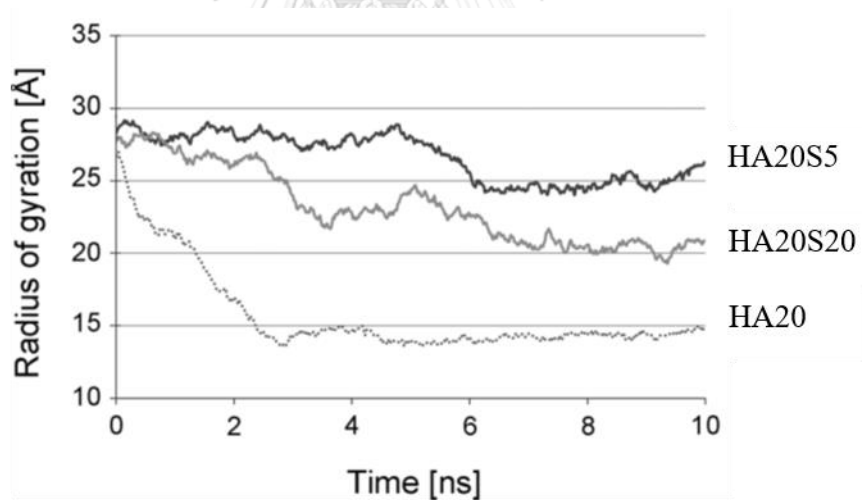


Figure 1.6 Decrease of radius of gyration for three type of HA20 [25]

1.4 Hydration of hyaluronic acid

Recently, there were a lot of publications studying amount of water adsorbed to HA molecule by experiments such as Differential Scanning Calorimetry (DSC), Polarization-resolved femtosecond-infrared spectroscopy, and Small Angle X-ray Scattering (SAXS) [26-28]. Průšová and group did the experiment to study the water content within the first hydration shell of HA by using traditional DSC and freezing DSC [26]. The results indicate that the freezing DSC is better to predict water content in room temperature. The amount of binding water is temperature dependent so the number of water molecules surrounding HA will decrease at high temperature for traditional DSC. The information about water content of HA from freezing DSC technique is shown in [Table 1.1](#). Low molecular weight HA has better water adsorption ability than high molecular weight HA.

Table 1.1 Water content within the first hydration shell for various sizes of HA

Molecular weight of HA (kDa)	Gram of water per one gram of HA	Number of water molecule per one HA molecule
3.5	0.82	17.2
100	0.74	16.5
254	0.74	16.5
740	0.74	16.5

Alber and group proposed a binary phase diagram of HA-water system [28]. Sodium hyaluronate with molecular weight 17 kDa was used to study hydration and thermodynamic properties of HA by using SAXS, DSC and isothermal sorption calorimetry. [Figure 1.7](#) shows that dry HA is in amorphous glassy state. HA demonstrates a glass transition at 25 wt% water and starts to crystallize at 34 wt% water. HA dissolves and becomes one-phase solution above 42 wt% water. The glass transition temperature (T_g) of HA is about -20 °C. Crystallization at high water contents is endothermic while it is exothermic for low water contents and high temperature. They also measured the hydrated water surrounding the first hydration

shell of HA by freezing DSC and got 0.62 gwater/gHA or 15 water molecules per disaccharide unit.

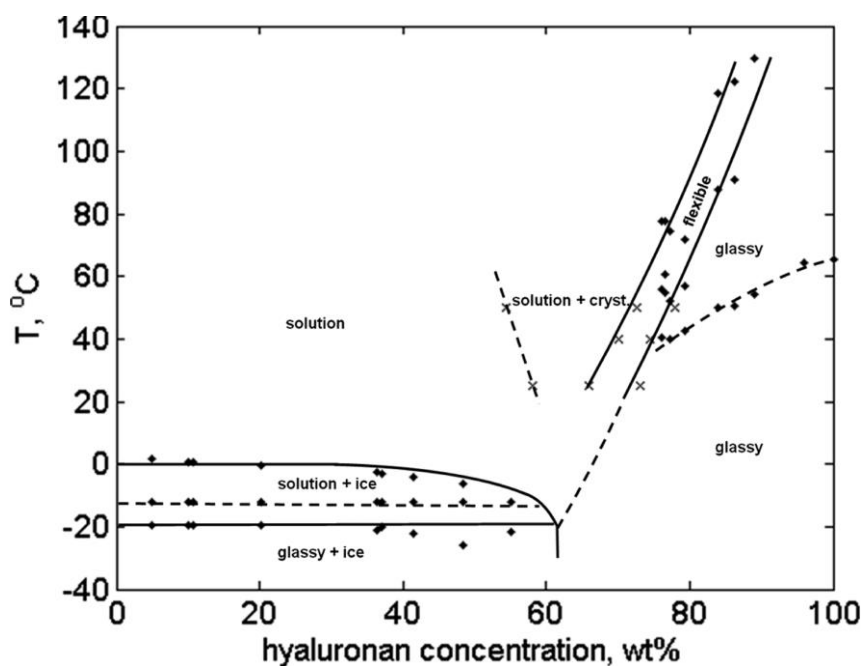


Figure 1.7 Phase diagram of the HA– water system. (◆) DSC data; (x) sorption calorimetric data. The dashed line to the right side of the phase diagram corresponds to the sub-Tg endotherm. The phase boundary between the flexible polymer and the two- phase region, solution and crystals, is a nonequilibrium transition. [28]

1.5 Interaction between HA and phospholipid membrane

There are few publications studying about interaction between HA and phospholipid membrane. Recently, Wieland and group studied DPPC-HA interfacial layers with different molecular weight of HA by using X-ray reflectivity (XRR) and grazing incidence diffraction (GID) for measurements of the Langmuir layers [29]. The data reveals an influence of HA on DPPC Langmuir layer induced by presence of calcium ions, and the strength of this effect increases with decreasing molecular weight of HA (Figure 1.8). Moreover, X-ray reflectivity measurements indicate that HA can be adsorbed to the hydrophilic part of DPPC.

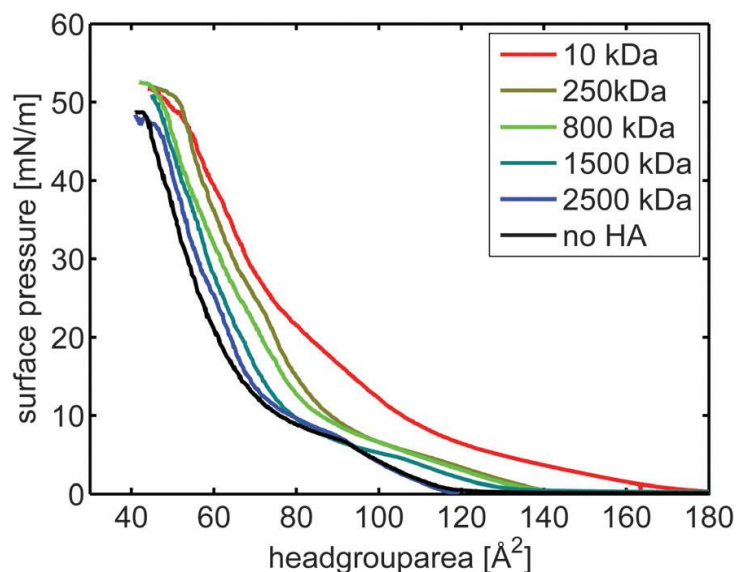


Figure 1.8 π/A -isotherms of DPPC on subphases containing sodium and calcium chloride ($[\text{NaCl}] = 155 \text{ mM}$, $[\text{CaCl}_2] = 10 \text{ mM}$). The concentration of HA was 0.5 mg/mL . [29]

Siódmiak and group studied the pH effect and HA-lipid interaction with LMW-HA by MD simulations [30]. The results indicated that R_g of HA is both pH- and phospholipid concentration-dependent. DPPC induces hydrophobic interactions in the system, causing LMW-HA to shrink and be absorbed into phospholipid vesicles at high concentration of vesicle (Figure 1.9). An increased pH also decreases R_g of HA. This observation can be applied in tribological surgical adjuvant design for osteoarthritis. Furthermore, Beldowski and group proposed that long chains of HA have an interaction with vesicle by capstan-like mechanism [31]. They used the steered molecular dynamics (SMD) to force HA molecule to be able to contact the vesicle through the simulation (Figure 1.10). The results show the efficiency of rotation from intermolecular bond creation and annihilation and the slide-to-roll relation of the movement of the attached molecules. In 2019, Herzog and group studied effect of high molecular weight HA (HMW-HA) on phospholipid model membranes by experiment such as DSC, fluorescence spectroscopy and small-angle X-ray scattering [32]. The data exhibits that there are not any significant interactions between HMW-HA and lipid.

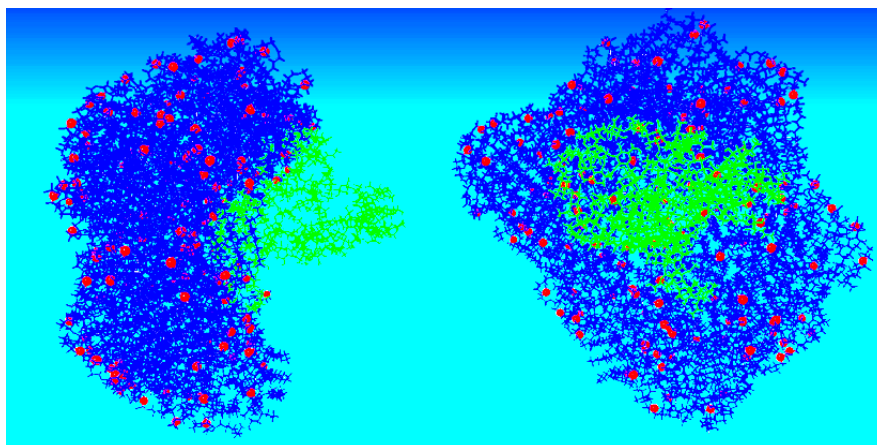


Figure 1.9 The MD trajectories: left-hand side shows HA (green) starting to be absorbed by vesicle (blue) and right-hand side shows HA absorbed completely by vesicle. The red points are phosphate groups in lipid structures. [30]

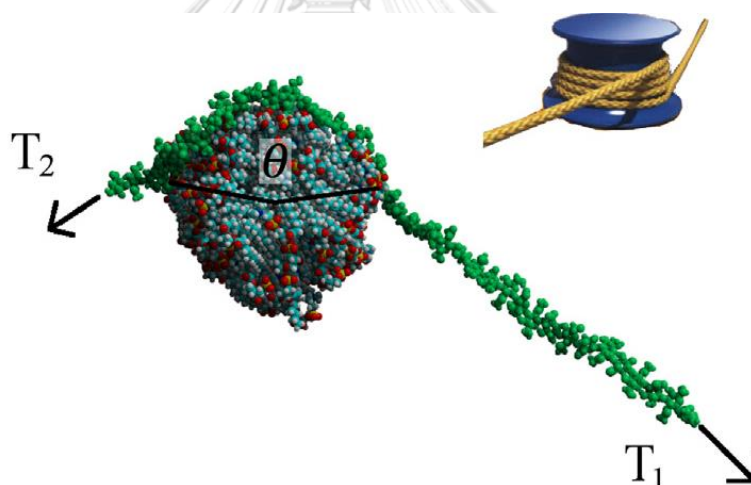


Figure 1.10 A snapshot of a final stage of simulation with pulling forces presented as black arrows. The figure presents capstan-like mechanism of the soft matter HA-phospholipid system. [31]

1.6 Inspiration of this research

High water adsorption capacity is a unique characteristic property of HA that makes it very valuable in cosmetics industry. The commercial HA-containing product should have high water adsorption with efficient skin permeation. It has been reported that low molecular weight HA (HA, MW < 50 kDa or the repeating disaccharide unit

< 125 units) have a better moisturizing ability with efficient skin penetration than that of the high molecular weight HA [10]. Because of a wide-range of applications, characterization of HA's conformation, interactions and hydration are essential to elucidate insight into its roles in biological applications. However, this has proven to be a challenge both experimentally and theoretically, due in part to uncertainty over the conformation of the HA polymer. Structural insights into the intrinsic flexibility in hyaluronan polymer are hence important to gain a better understanding of its biological function. In this study, structure, dynamics and hydration properties of low molecular weight HA are investigated by MD simulations in aqueous solution. Analysis of MD data such as radius of gyration, flexibility of glycosidic-bond, hydrogen-bond and cation interactions provides the basis for understanding of the relationships between their structure and properties. Furthermore, we also study permeability of HA through phospholipid bilayer by MD simulations in HA-membrane systems.

1.7 Objectives of research

- 1) To study conformation and hydration of LMW-HA by MD simulations and investigate the effect of size of HA to water absorption ability.
- 2) To study interaction and stability of HA with phospholipid membrane by MD simulations.

CHAPTER 2

THEORY

2.1 Molecular dynamics (MD) simulation

To investigate molecular properties of biological molecules in atomic level, MD simulation is one of most useful techniques in theoretical studies. This method can simulate molecular movement based on Newton's second law ($F = ma$). The force (F) is a negative value of the first derivative of potential energy (U) with position (r) and acceleration (a) is the second derivative of position (r) and time (t). Thus, equation (1) is a main equation in MD simulation, where $i = 1, 2, \dots, N$ atom [33-34].

$$-\frac{dU_i}{dr_i} = m \frac{d^2r_i}{dt^2} \quad (1)$$

The differential equation (1) can be solved by velocity-Verlet algorithm to find the relation between positions of every atom and arbitrary time, and finally generate the frame rate of molecular movement or MD trajectory [35].

2.1.1 Force fields [34]

The interatomic potential energy function of each atom, $U(r_i)$, has been developed by idea of bonded and non-bonded interactions as shown in equation (2).

$$U_{\text{total}} = U_{\text{bonded}} + U_{\text{non-bonded}} \quad (2)$$

$$= (U_{\text{str}} + U_{\text{bend}} + U_{\text{imp}} + U_{\text{tor}} + U_{\text{cross}}) + (U_{\text{vdw}} + U_{\text{elec}}) \quad (3)$$

The energy in bonded term is comprised of stretching energy (U_{str}), bending energy (U_{bend}), improper bending or out-of-plane bending term (U_{imp}), cross terms (U_{cross}) and torsional energy (U_{tors}). And non-bonded energy is calculated from van der waals energy (U_{vdw}) and electrostatic energy (U_{el}). The cross terms are coupling energies from stretching and bending term. The equation (4) is full expansion of each term from equation (3).

$$\begin{aligned}
 U_{\text{total}} = & \sum_{\text{str}} k^{AB} (R^{AB} - R_0^{AB})^2 + \sum_{\text{bend}} k^{ABC} (\theta^{ABC} - \theta_0^{ABC})^2 \quad (4) \\
 & + \sum_{\text{bend}} k^{\text{imp}} \chi^2 + \sum_{\text{tors},n} k_n^{ABCD} [\cos(n\phi^{ABCD})] + U_{\text{cross}} \\
 & + \sum_{\text{vdw}} 4 \epsilon \left[\left(\frac{\sigma}{r_{AB}} \right)^{12} - \left(\frac{\sigma}{r_{AB}} \right)^6 \right] + \sum_{\text{elec}} \frac{q_A q_B}{r_{AB}}
 \end{aligned}$$

The elastic potential energy from classical mechanics is used to calculate bonded terms. The torsional energy is written as a Fourier series. The parameters k^{AB} , k^{ABC} , k^{imp} and k^{ABCD} are force constants for stretching, bending, improper bending and torsional terms, respectively. The van der waals energy is usually calculated from Lennard-Jones potential and coulomb's equation is used for electrostatic term. R^{AB} , θ^{ABC} , χ and ϕ^{ABCD} are arbitrary bond length, bond angle, improper angle and torsion angle, respectively (Figure 2.1). R_0^{AB} and θ_0^{ABC} are bond length and bond angle at stationary phase. r_{AB} is non-bonded distance and q_i is atomic charge for atom i .

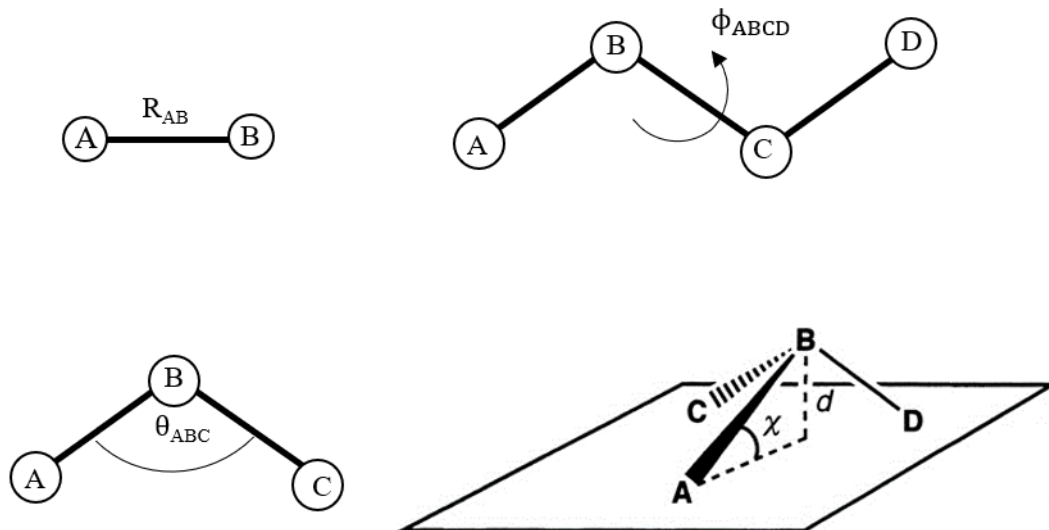


Figure 2.1 bond length (R^{AB}), bond angle (θ^{ABC}), improper angle or out-of-plane angle (χ) and torsion angle (ϕ^{ABCD})

The parameters k^{AB} , k^{ABC} , k^{ABCD} , ϵ , σ and q_i are called force field parameters which are unique for each atom and molecule. There are a lot of publications developing the force field parameters for biomolecules. CHARMM force fields are ones of popular force fields for carbohydrate, protein, lipid and nucleic acid [36-39]. The parameters for water depend on water model. TIP3P water is usually used in MD simulation [40].

2.1.2 Periodic boundary conditions (PBCs) and ensembles

In real system, there are tremendous number of biomolecules solvated in solution. It takes very long time to simulate the realistic model. To save a simulation time, PBCs are normally employed (Figure 2.2). PBCs are a set of boundary condition which are often chosen for approximating a large (infinite) system by using a small part called a unit cell. The solvent molecules are modeled as a suitable box. This box is duplicated in all directions, so a central box is surrounded by 26 another duplicated boxes [34]. In computer simulations, only one of infinite unit cells is simulated and the other cells are copied.

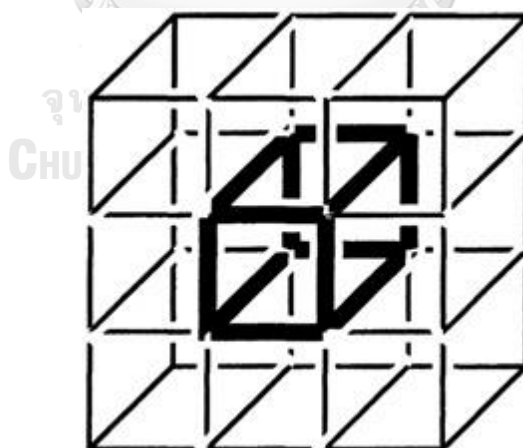


Figure 2.2 Periodic boundary condition [34]

The thermodynamic quantities of system in PBCs are calculated by statistical mechanics. Ensemble is an idealization composed of many or infinite virtual copies of a system and each of them represents a possible state reflecting the real system [33].

So, PBC is a molecular ensemble. There are several types of ensemble. Biological system is usually studied by the isothermal-isobaric ensemble (NPT ensemble) and the canonical ensemble (NVT ensemble).

2.2 Steered molecular dynamics (SMD) simulation

Molecular movements from traditional MD simulation is based on internal forces from potential energy. However, some studies need to apply an external force to systems for more observation. Steered Molecular Dynamics (SMD) is a MD simulation that applies an external force to biomolecules in a chosen direction [41]. So, the equation motion for atom applied an external force is written as

$$F_{\text{ext}} - \frac{dU_i}{dr_i} = m \frac{d^2r_i}{dt^2} \quad (5)$$

A lot of important applications of SMD are in the field of drug discovery and biomolecular sciences. For example, SMD was used to investigate the stability of Alzheimer's protofibrils to study the protein ligand interaction [42-43].

2.3 Analysis from MD results

2.3.1 Root mean square deviation (RMSD)

RMSD is a parameter used to follow structural fluctuation, compared to a reference structure. The first step of calculation, two corresponded atoms from both molecules are fitted by least-square method. After that, RMSD will be calculated as equation (6), where m_i is atomic mass of i^{th} atom, r_{1i} is position of i^{th} atom from reference structure and r_{2i} is position of i^{th} atom from selected structure. If the reference structure is average structure, it will be called RMSF.

$$\text{RMSD} = \sqrt{\frac{1}{\sum_{i=1}^N m_i} \sum_{i=1}^N m_i \|r_{1i} - r_{2i}\|^2} \quad (6)$$

2.3.2 Radius of Gyration (Rg)

If a structure is estimated to be like a sphere, the radius of that sphere is called radius of gyration (Rg). Rg can be calculated by equation (7), where r_i is the position of i^{th} atom and \bar{r} is the position of center of mass.

$$R_g = \sqrt{\frac{1}{\sum_{i=1}^N m_i} \sum_{i=1}^N m_i \|r_i - \bar{r}\|^2} \quad (7)$$

2.3.3 Radial pair distribution function (RDF)

The radial pair distribution function (RDF, $g(r)$) describes how density of two pair atoms as a function of distance. And the number integral $\int_0^r \rho g(r) r^2 dr$ means all pairs of atoms in the two selections, where ρ is a constant.

2.3.4 Hydrogen bond (H-bond)

The geometric criteria for determining a H-bond includes the distance between hydrogen donor and acceptor atoms (D...A) of less than 3.5 Å and the $D\hat{H}A$ angle of greater than 120 degrees ($180^\circ \pm 60^\circ$), see [Figure 2.3](#).

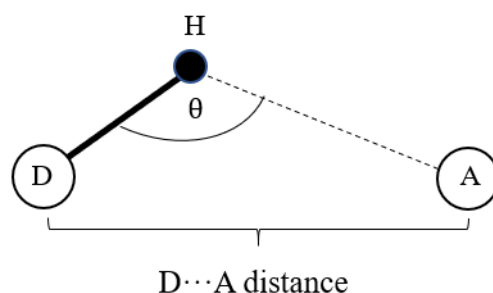


Figure 2.3 Criteria of H-bond between two molecules, θ is $D\hat{H}A$ angle.

2.3.5 Potential of mean force (PMF)

The potential of mean force (PMF) is a method to obtain how the free energy changes as a function of a coordinate of the system. This method can calculate the free energy from the average force based on statistical mechanics [44]. PMF of a system with N particles is constructed by the potential giving the average force over all the configurations of all the $n+1, \dots, N$ particles acting on a particle j at any fixed configuration keeping fixed a set of particles $1, 2, 3, \dots, n$. The average force is defined as shown in equation (8).

$$-\nabla_j w^{(n)} = \frac{\int e^{-\beta V} (-\nabla_j V) dq_{n+1} \dots dq_N}{\int e^{-\beta V} dq_{n+1} \dots dq_N}, j = 1, 2, 3, \dots, n \quad (8)$$

Where $\beta = \frac{1}{k_B T}$, the $-\nabla_j w^{(n)}$ is the average force and $w^{(n)}$ is the PMF. Therefore, $w^{(2)}(r_{12})$ describes the interaction between two molecules at a fixed distance (r) when the remaining $N - 2$ molecules are canonically averaged over all configurations.

2.4 Density functional theory (DFT)

To study the electronic properties, we need a high accurate method. Ab Initio and DFT methods are acceptable. The ground state electronic energy of DFT method is determined completely by the electron density function, $\rho(r)$, while Ab Initio methods use wave function approach [34]. A general DFT energy expression can be written as following equation.

$$E_{\text{DFT}}[\rho] = T[\rho] + E_{\text{ne}}[\rho] + J[\rho] + K[\rho] + E^{\text{corr}} \quad (9)$$

$$= T[\rho] + E_{\text{ne}}[\rho] + J[\rho] + E_{\text{xc}}[\rho] \quad (10)$$

From derivation, kinetic energy ($T[\rho]$), attraction term between electrons and nuclei ($E_{\text{ne}}[\rho]$) and coulomb integral term ($J[\rho]$) are still like Hartree-Fock theory. The main problems are exchange integral term ($K[\rho]$) and correlation term (E^{corr}). Thus, the accuracy of DFT method depends on the level of theory that calculates the exchange-correlation term.

2.4.1 B3LYP method

B3LYP is a hybrid functional to calculate exchange-correlation energy (E_{xc}). This method uses Local spin density approximation (LSDA), Hartree-Fock theory and Generalized gradient approximation (GGA) to calculate exchange energies. The GGA functional in B3LYP method is Becke (B or B88) functional [45]. The correlation energies are calculated by LSDA functional and LYP functional [46-47]. The overall equation contains three parameters (a, b and c) as shown in equation (11).

$$E_{xc}^{B3LYP} = (1 - a)E_x^{LSDA} + aE_x^{HF} + b\Delta E_x^{B88} + (1 - c)E_c^{LSDA} + cE_c^{LYP} \quad (11)$$

2.4.2 Basis set

Some terms of energies in DFT method are obtained by Ab initio method, so DFT calculation needs parameters from basis set. The basis functions are introduced as wave functions of atomic orbitals because Schrödinger equations of many electron systems cannot be solved. There are two types of basis functions: *Slater-Type Orbitals* (STOs) and *Gaussian-Type Orbitals* (GTOs). The GTOs are more extensively used, and the primitive function can be written as equation (12),

$$g(x, y, z) = N x^{l_x} y^{l_y} z^{l_z} e^{-\xi r^2} \quad (12)$$

where N is normalizing constant. l_x , l_y and l_z are angular momentums. ξ is orbital exponent depending on atom type and $r^2 = x^2 + y^2 + z^2$.

Since the electrons on inner shell and outer shell have different environment, the *contracted basis sets* are introduced to separate core orbitals and valence orbitals. The atomic orbitals are contracted gaussian type orbitals (CGTOs) being linear combination of primitive gaussian function. Pople style basis sets are one of most common basis sets usually used in calculation, for example, 6-31G basis set [48]. The atomic orbitals in core shell of this type of basis set are linear combination of six primitive gaussian functions, $G = d_1g_1 + d_2g_2 + d_3g_3 + d_4g_4 + d_5g_5 + d_6g_6$.

CHAPTER 3

METHODOLOGY

3.1 Computational software

3.1.1 CHARMM [49]

Chemistry at Harvard Macromolecular Mechanics (CHARMM) is the name of a widely used set of force fields for molecular dynamics, and the name for the molecular dynamic simulation and analysis computer software package. CHARMM has a lot of data base of natural biomolecular structures and their force field parameters and it also has the web-based graphical user interface (CHARMM-GUI) to predict the force field parameters of unknown molecules [50].

3.1.2 VMD [51]

Visual Molecular Dynamics (VMD) is a molecular visualization program for displaying, animating, and analyzing large biomolecular systems using 3-D graphics and built-in scripting. VMD supports computers running MacOS X, Unix, or Windows, is distributed free of charge, and includes source code. VMD is a free program that is developed by Theoretical and Computational Group in University of Illinois and available on the web page, (<http://www.ks.uiuc.edu/Research/vmd/>).

3.1.3 NAMD [52]

Nanoscale Molecular Dynamics (NAMD) is a parallel molecular dynamics code designed for high-performance simulation of large biomolecular systems. NAMD uses the popular molecular graphics program VMD for simulation setup and trajectory analysis. NAMD is a free software developed by the Theoretical Biophysics Group in the Beckman Institute for Advanced Science and Technology at the University of Illinois at Urbana-Champaign, (<http://www.ks.uiuc.edu/Research/namd/>).

3.1.4 Gaussian 09 [53]

Gaussian is a general computational chemistry software package initially released in 1970 by John People. This software can calculate single point energy, optimize molecular structure, and predict many electronic properties.

3.2 Preparation of HA structure

HA models with various chain length were built based on the structure of with Protein Data Bank code 2BVK [21]. Structure models consisting of 1, 5, 10, 20, 30, 40, 50, 60, 80 and 100 disaccharide units of HA (denoted as HA1, HA5, HA10, HA20, HA30, HA40, HA50, HA60, HA80 and HA100 respectively) were built by cutting or replicating the PDB 2BVK structure using CHARMM software with CHARMM36 carbohydrate topology [49]. For HA1 only, there exists two structural isomers, in which the two monosaccharides are linked together by $\beta(1,3)$ or by $\beta(1,4)$ glycosidic bonds. The corresponding disaccharide sequences of $\beta(1,3)$ and $\beta(1,4)$ isomers are GlcA-GlcNAc and GlcNAc-GlcA, respectively. As shown in Figure 3.1a, b, each linker proceeds two torsion angles, ϕ_{13} and ψ_{13} for the $\beta(1,3)$ bonds and ϕ_{14} and ψ_{14} for the $\beta(1,4)$ bonds, which determine the relative orientation of the two saccharide rings. The structures of HA with long chains have linear shapes with left-handed 4-fold helixes (Figure 3.1c, d).

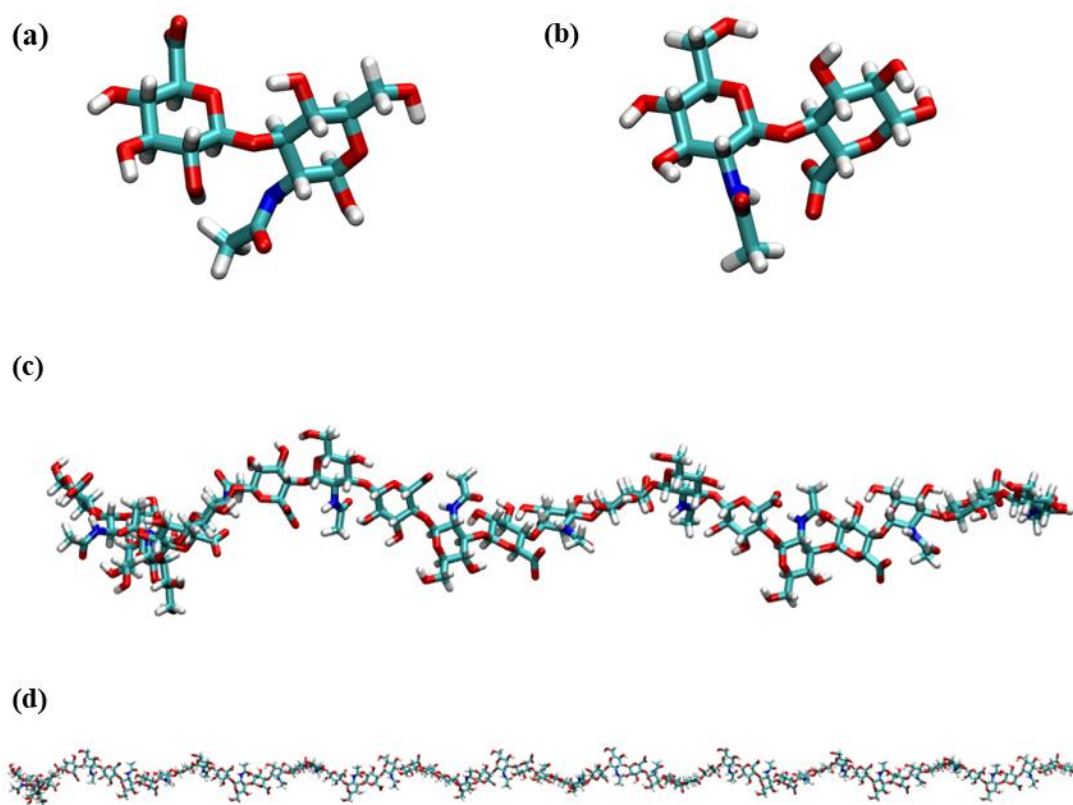


Figure 3.1 Structures of (a) HA1- β (1,3) isomer (b) HA1- β (1,4) isomer (c) HA10 and (d) HA30 that are built by CHARMM software from PDB 2BVK structure (cyan, blue, red, and grey colors are carbon, nitrogen, oxygen and hydrogen, respectively. Structures were drawn by VMD 1.9.3)

3.3 MD simulations in vacuum

From [Figure 3.1d](#), end-to-end distance of HA30 is very long, so linear structures of long chain HA aren't good initial structures for MD simulations in water. Many publications reported long chain HA behave random coil conformations [22-25]. Thus, we needed to pre-equilibrate some of HA structures to obtain the random coil shapes before the MD simulations in water. We performed 50 ns MD simulations on a straight chain of HA5, HA10, HA20, HA30, HA40, HA50, HA60, HA80 and HA100 in vacuum by using NAMD software [52] with CHARMM36 carbohydrate force field parameters [39]. All the carboxyl groups are fully dissociated because its pKa is 3-4 at pH 7 and we assumed the simulations carried out at neutral condition. Temperature of systems is 300 K and pressure is 1 atm. The trajectories are investigated by measuring

RMSD and Rg. The RMSDs relative to the initial structure were calculated for heavy atoms of HA chains. We measured the average Rg from last 20 ns of each system and select the snap shots that HA structures correspond to average Rg to be the starting structures for MD simulations in explicit water solvent.

3.4 MD simulations in water

3.4.1 System set up

Both $\beta(1,3)$ and $\beta(1,4)$ isomers of HA1 are simulated in aqueous condition. For HA5 and HA10, we used both straight chain and random-coiled configuration as starting conformations for MD simulations while HA20-50 are used only random-coiled configuration as initial structures. All the carboxyl groups are also fully ionized. Each model system was solvated with TIP3P water molecules in a rectangular box with 0.1 M NaCl. [Figure 3.2](#) shows model of HA20 solvated by water within $150 \times 130 \times 120$ Box size (\AA^3). The simulation box size and number of atoms used in each system are summarized in [Table 3.1](#). The process for setting up the systems was achieved through TCL scripts in VMD 1.9.3 [\[51\]](#).

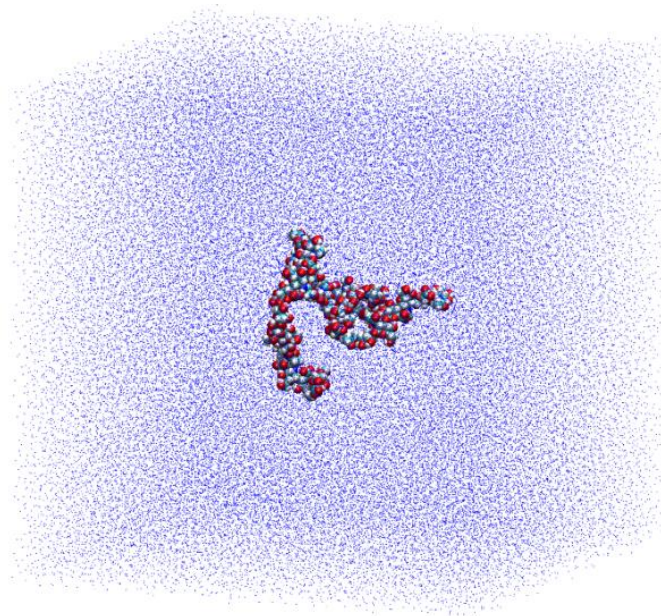


Figure 3.2 Model of HA20 solvated by water in rectangular box

Table 3.1 The simulated systems, initial structures, periodic boundary sizes and number of atoms for MD simulations.

System	Initial structure	Box size (\AA^3)	Total number of atoms
HA1	$\beta(1,3)$ isomer	$40 \times 40 \times 40$	5,919
	$\beta(1,4)$ isomer	$40 \times 40 \times 40$	5,919
HA5	Linear	$65 \times 75 \times 60$	27,784
	Random-coiled	$54 \times 60 \times 58$	16,238
HA10	Linear	$110 \times 110 \times 110$	127,439
	Random-coiled	$105 \times 100 \times 100$	101,252
HA20	Random-coiled	$150 \times 130 \times 120$	227,352
HA30	Random-coiled	$170 \times 130 \times 130$	278,276
HA40	Random-coiled	$145 \times 185 \times 160$	415,920
HA50	Random-coiled	$190 \times 190 \times 180$	632,589

3.4.2 MD simulations

MD simulations were carried out using NAMD software [52] with CHARMM36 carbohydrate force field parameters [39]. The simulations were performed in NPT ensemble with periodic boundary conditions. All covalent bonds to hydrogen atoms were kept rigid using the 131 LINCS algorithm [54]. The water geometry was constrained as rigid using the SETTLE method [55]. A distance cutoff of 12 \AA was employed for electrostatic and van der Waals interactions. Electrostatic interactions were calculated with particle mesh Ewald summation. The temperature of all systems is 300 K. Langevin thermostat with a damping coefficient of 1 ps^{-1} was used to maintain a constant temperature of 300 K. Pressure was kept constant at 1 atm using the Nose – Hoover Langevin piston method. Energy minimization was performed to remove bad contacts between atoms. The HA chains were initially kept fixed to their initial positions while water and counterion were allowed to equilibrate for about 1 ns. Then, the systems were equilibrated by 1 ns MD simulations with position restraints on HA atoms. Subsequently, 100-200ns of MD simulations were performed for each

system with a time step of 1 fs. At least three independent MD runs of each system were carried out for obtaining results with statistical significance.

3.4.3 Trajectory analysis

All trajectory analyses, except for the calculations of solvation free energy and DFT optimization, were performed using TCL scripts in VMD. Unless otherwise specified, MD trajectories were extracted from the production phases during the last 20 ns of the simulations. We have selected a rather small part of the trajectories in asymptotic limit (last 20 ns) out of a relatively long run (100-200ns). This is primarily to make sure that our system has reached thermodynamic equilibrium fully and that the last 20 ns simulation is sufficient with least deviation to extract structural features.

- *RMSD, RMSF and R_g*

The root-mean-square deviation (RMSD), root-mean-square fluctuation (RMSF) and the radius of gyration (R_g) as a function of simulation time were computed to investigate the flexibility characteristics of HA polymer chains. The RMSDs relative to the initial structure were calculated for heavy atoms of HA chains. The RMSFs were computed with respect to the average structure of the last 20 ns of the production phases. The R_g as a function of time was computed throughout MD trajectory to show the conformational flexibility and variability. In addition, the radius of gyration (R_g) averaged over the trajectory was analyzed to illustrate structural variability in polymer shape.

- *Conformational variation, hydration and interaction with ions*

From MD trajectories, ensembles of HA conformations at the glycosidic linkages were analyzed in terms of the distribution of glycosidic torsion angles, ϕ_{13} , ψ_{13} , ϕ_{14} and ψ_{14} [21]. These rotatable torsion angles are also used to quantify the flexibility of the HA polymer based on the pattern of the (ϕ , ψ) distribution. We used k-mean clustering algorithm to group similar conformations on the basis of the

distributed torsion angles and to find representative conformations of the clusters for DFT calculations.

An analysis of hydrogen bonding (H-bond) was focused on the disaccharide unit across glycosidic linkages. The geometric criteria for determining a H-bond includes the distance between hydrogen donor and acceptor atoms ($X\cdots X$) of less than 3.5 Å and the $X\hat{H}X$ angle of greater than 120 degrees ($180^\circ \pm 60^\circ$). The percentage occupancy of H-bond was computed over all frames of the last 20 ns.

For an analysis of the hydration structure, the probability of finding water molecules surrounding the HA chain was analyzed in terms of radial pair distribution function ($g(r)$). The hydration number was obtained by counting numbers of water within the first shell of $g(r)$ plots. The $g(r)$ analysis between HA and sodium or chloride ions were carried out to investigate possible binding sites of HA for counter ions [51].

- *Solvation free energy*

We employed the Molecular Mechanics - Generalized Born Surface Area (MM-GBSA) method to estimate the solvation free energies of HA [56]. For the MM-GBSA calculations, snapshots of the systems were extracted from the last 20 ns of MD trajectories, and the explicit water molecules and ions were removed. For each snapshot, the solvation free energy was calculated as follows:

$$\Delta G_{solv} = \Delta G_{GB} - \Delta G_{NP}$$

where ΔG_{GB} defines the polar solvation energy calculated by the generalized Born implicit solvent methods. ΔG_{NP} describes the nonpolar component which is estimated based on the solvent-accessible surface area (SASA) as follows:

$$\Delta G_{NP} = \gamma SASA + \beta$$

where the SASA surface tension (γ) and the offset (β) was set the standard values of 0.005420 kcal mol⁻¹ Å⁻² and 0.8 kcal mol⁻¹, respectively. The dielectric constant of the solvent was set 78.5 and the ionic strength was set to 0.3. All the MM/GBSA calculations were carried out using CHARMM36 carbohydrate force field parameters [39]. Solvation free energies were calculated by NAMD software [52].

- DFT geometry optimization

In order to evaluate the conformational energies of $\beta(1,3)$ and $\beta(1,4)$ isomers, the geometry optimization was performed using density functional theory (DFT) calculations. The calculation is a section of only one disaccharide unit which is taken from the equilibrium structure of the simulations of HA chains. The k-mean clustering analysis of ϕ and ψ distribution was employed for the selection of the representative unit of the populated ensemble in the MD trajectory. The full geometry optimization was carried out using DFT/B3LYP method at 6-31G* basis set level in the presence of water CPCM solvent model [57]. Single point calculations were performed on these structures before and after DFT optimization. This process was repeated for three independent runs and we selected the structure with lowest energy from three runs to analyze. All the DFT computations were performed by using Gaussian 09 package [53] and Gauss-View molecular visualization programs.

3.5 Transfer of HA across membranes

The skin permeation of HA has been experimentally studied, and it is observed that low molecular weight of HA can penetrate skin [25, 58]. This study aims to explore whether the transfer of small hyaluronic acid through the lipid bilayer is passive or active. The work consists of two approaches. The first approach was to perform MD simulations of HA in a hydrophobic environment. The two smallest units of HA used in the thesis were chosen for conducting the research. In the second approach, a transfer of the HA across membranes was demonstrated in terms of the free energy. Details of the method is described below.

3.5.1 Setup of a membrane simulation system

Only HA1 and HA5 were chosen for examining the stability of hyaluronic acid in biological membranes. The simulations were carried out by placing the center of mass of HA at two different locations in membrane, (1) at the center of membrane and (2) at the interface between water and membrane regions (Figure 3.3). The initial

structures of HA5 are random-coil configuration selected from trajectories of MD simulations in gas phase. All the carboxyl groups are also fully ionized. Each model system was immersed in a pre-equilibrated 1-Palmitoyl-2-Oleoyl-sn-Glycero-3-Phosphocholine (POPC) lipid and TIP3P water molecules in a rectangular box with 0.1 M NaCl. In addition, a control MD simulation of non-polar molecules, benzene and (+)-limonene, in biological membranes was carried out for comparison. The simulation box size and number of atoms used in each system are summarized in [Table 3.2](#). The process for setting up the membrane systems was achieved through TCL scripts in VMD 1.9.3 [51].

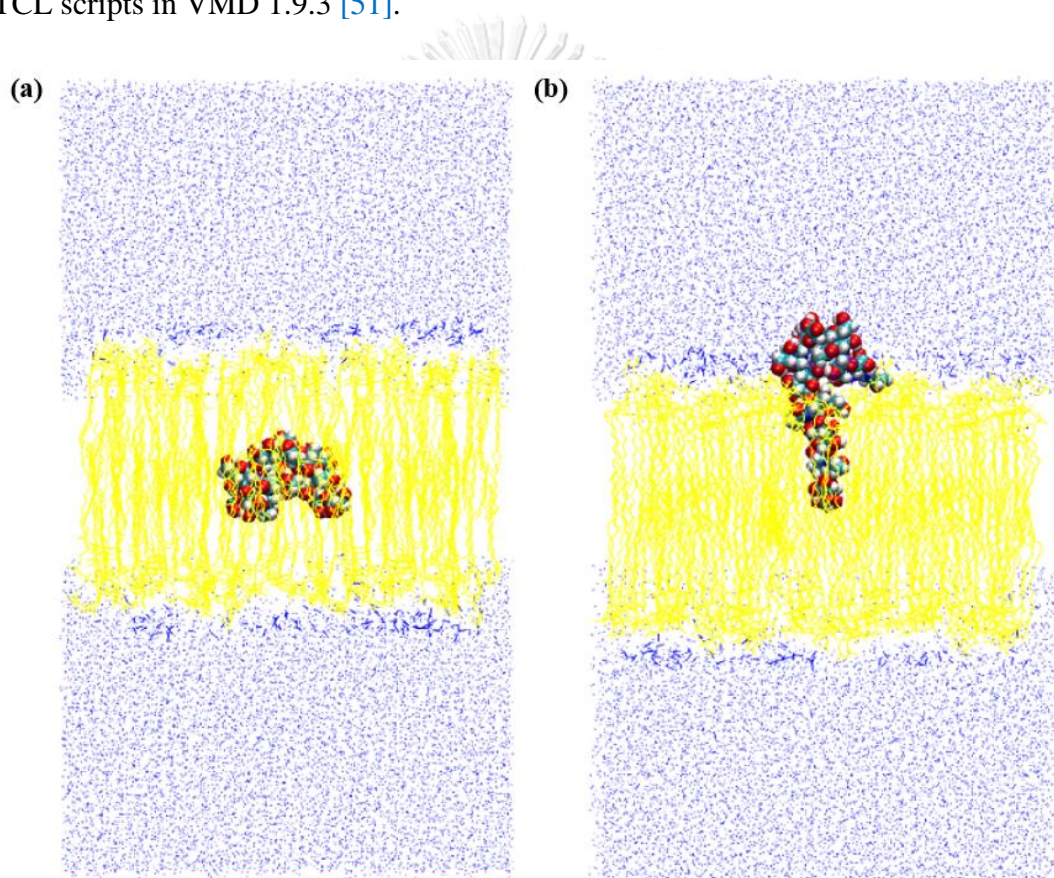


Figure 3.3 (a) Model of HA5 in center of membrane and (b) Model of HA5 in membrane interface, yellow structure and blue point are lipid and water, respectively.

Table 3.2 The simulated systems, initial position of the HA center of mass, periodic boundary sizes and number of atoms for MD simulations.

System	Initial position of HA	Box size (Å ³)	Total number of atoms
HA1-β(1,3)	membrane center	65 × 65 × 90	27,928
	membrane interface	65 × 65 × 100	30,627
HA1-β(1,4)	membrane center	65 × 65 × 90	27,928
	membrane interface	65 × 65 × 100	30,627
HA5	membrane center	80 × 80 × 140	77,561
	membrane interface	80 × 80 × 140	78,400
Benzene	membrane center	65 × 65 × 90	27,067
	membrane interface	65 × 65 × 100	30,785
(+) -Limonene	membrane center	65 × 65 × 90	26,953
	membrane interface	65 × 65 × 100	30,664

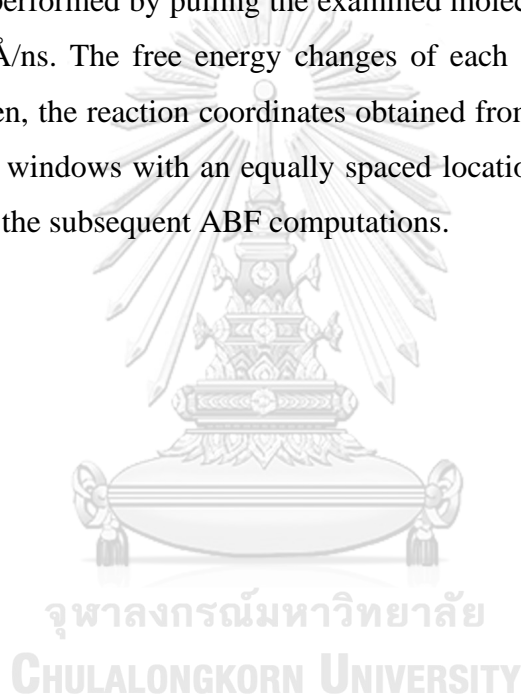
3.5.2 MD simulations

MD simulations were carried out using NAMD software [52] with CHARMM36 force field parameters for both carbohydrate and lipid [38-39]. Other algorithms are same with MD simulation in water. The temperature of all systems is 300 K. Energy minimization was performed to remove bad contacts between atoms. The HA chains were initially kept fixed to their initial positions while water and counterion were allowed to equilibrate for about 1 ns. Then, the systems were equilibrated by 2 ns MD simulations with position restraints on atoms of HA, lipid and water. Subsequently, 100ns of MD simulations were performed for each system with a time step of 1 fs. At least three independent MD runs of each system were carried out for obtaining results with statistical significance.

For an analysis of MD trajectory, RMSD relative to the starting structure and the distance (between the center of mass of the studied molecule and the membrane center) projected onto the z-axis were computed. Both quantities were monitored as a function of simulation time to illustrate the stability within the membrane.

3.5.3 Free energy of membrane penetration [44]

The free energy profile of HA across the membrane has been explored by calculating the potential of mean force (PMF). This step consists of two main parts. Initially, a steered molecular dynamics (SMD) simulation is performed to generate the membrane permeation pathway to HA molecule. Subsequently, the PMF is determined by exploring the SMD pathway with Adaptive Bias Force (ABF) method. To conduct SMD, a snapshot taken from equilibrium MD simulations of the two HA1 isomers, benzene and (+)-limonene were used to build the starting systems. The SMD simulations were performed by pulling the examined molecule through the membrane at a speed of $1.0\text{\AA}/\text{ns}$. The free energy changes of each molecules were shown by PMF diagram. Then, the reaction coordinates obtained from the SMD trajectory were divided into small windows with an equally spaced location (1\AA in length) and used as initial states for the subsequent ABF computations.



CHAPTER 4

RESULTS AND DISCUSSION

4.1 MD simulation in water

4.1.1 Conformational flexibility of the two glycosidic linkers

The RMSD, RMSF and R_g curves as a function of time for HA1 systems indicate that the structures of the two isomers are in relatively stable states (Figure 4.1). For the smallest HA1 unit, the structure of the $\beta(1,3)$ isomer is very stable with a narrow range of fluctuation. The $\beta(1,4)$ isomer exhibited more structural variant. The $\beta(1,3)$ RMSD rises at around 30 ns and 80 ns, and shifts back to its equilibrium value within a very short time. On the other hand, the larger variation of RMSD values is observed for $\beta(1,4)$. This suggests that the saccharide rings joined by the $\beta(1,4)$ linkage is more flexible in conformation than the $\beta(1,3)$ conformer.

Additionally, the glycosidic torsion angles, ϕ and ψ , during the last 20ns of MD trajectories illustrated the different flexibility between the two isomers. The (ϕ , ψ) distribution shows that the conformation of HA1 $\beta(1,3)$ isomers distributed in one cluster (Figure 4.2a). However, the distribution of $\beta(1,4)$ isomer is more spread out than that of $\beta(1,3)$ isomer (Figure 4.2b). The centroid point of the cluster for the $\beta(1,3)$ conformation corresponds to ϕ_{13} of $46.5^\circ \pm 0.6^\circ$ and ψ_{13} of $-7.6^\circ \pm 0.4^\circ$. The ϕ_{14} and ψ_{14} at the centroid point of the $\beta(1,4)$ cluster are $50.3^\circ \pm 8.4^\circ$ and $6.7^\circ \pm 4.9^\circ$, respectively. The values of torsion angles are in good agreement with the data reported previously [15-17, 21]. The results suggested that the two monosaccharide rings joined together with the $\beta(1,4)$ linkage are more mobile than those of the $\beta(1,3)$ linkage.

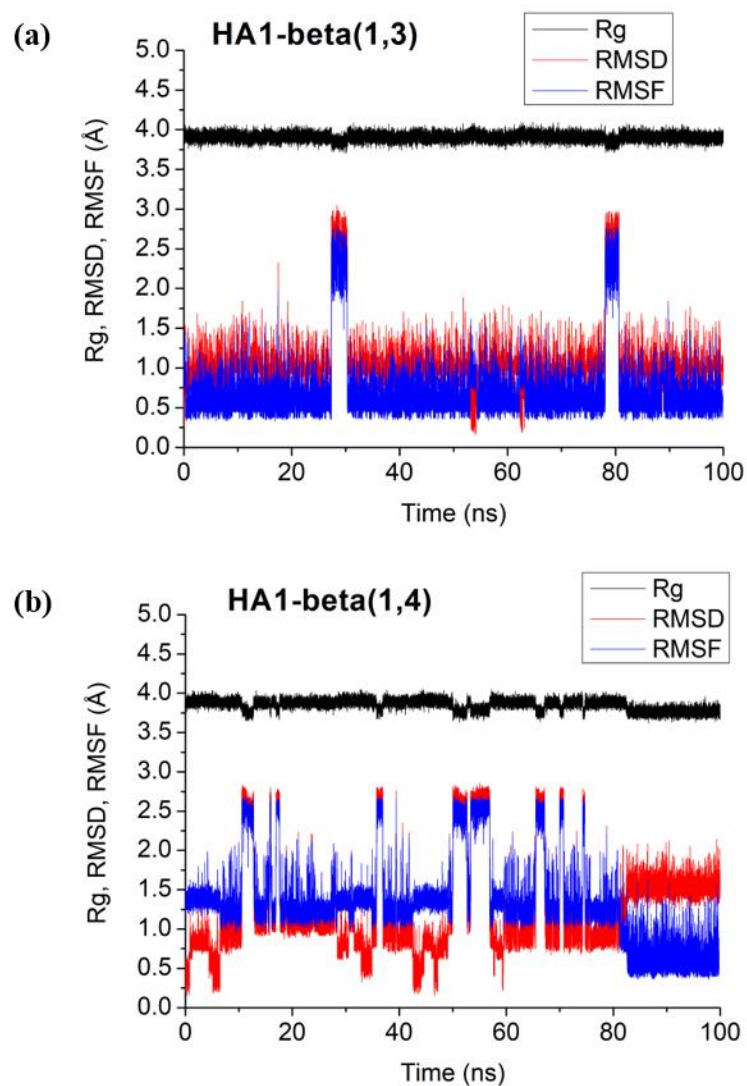


Figure 4.1 RMSD relative to the starting structure, RMSD and Rg as a function of time for HA1 chains for (a) $\beta(1,3)$ isomer and (b) $\beta(1,4)$ isomer.

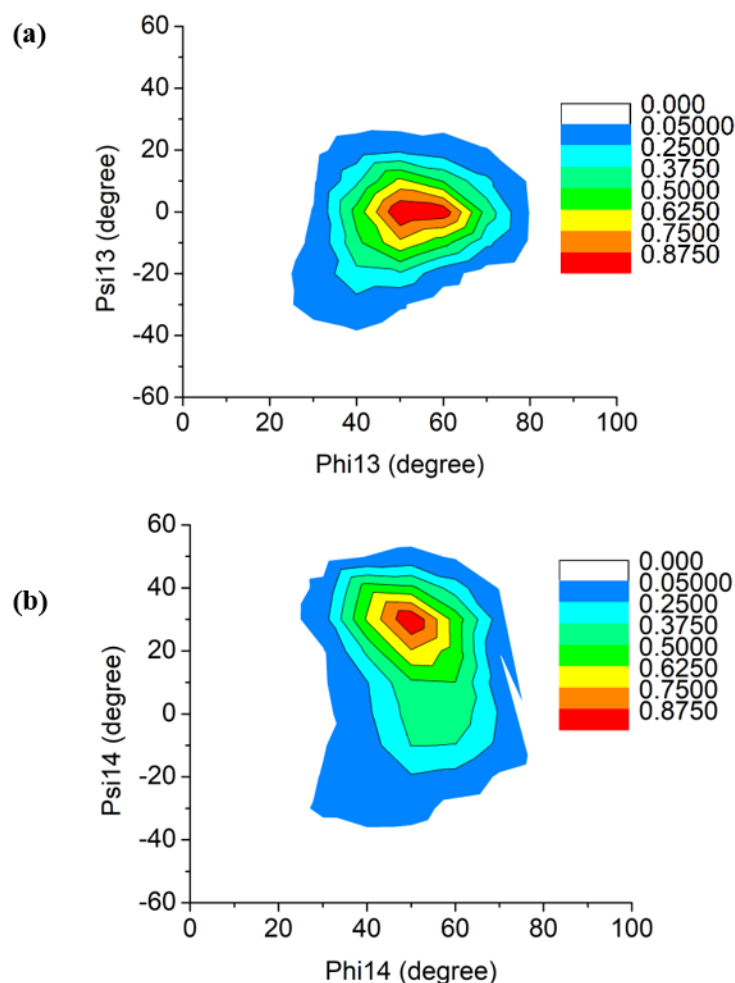


Figure 4.2 The (ϕ , ψ) distribution plots showing the favorable region of the conformation at glycosidic linkages **(a)** $\beta(1,3)$ linkage and **(b)** $\beta(1,4)$ linkage, both graph were extracted from 10,000 snapshots of HA1 and the populated fraction is indicated by contour colors.

Moreover, a difference in the conformational flexibility of the two isomers may additionally be described by H-bond between the two saccharide rings at the glycosidic bond. The stability of H-bond is associated with its percentage occupancy from MD trajectory. Thus, we calculated the percentage occupancy of inter-saccharide H-bond at glycosidic linkages with the criteria described in Method section. [Figure 4.3a](#), [4.3b](#) illustrate the possible H-bonds and its occupancy averaged over three independent simulations.

We found that the H-bond between O4–H(GlcNAc)···O5(GlcA) was the major contributor to the stability of the $\beta(1,3)$ conformation with the occupancy of 63%, whilst the H-bond occupancy of O3–H(GlcA)···O5(GlcNAc) was less with 38% for $\beta(1,4)$ isomer (Figure 4.3). Other pairs of H-bonds showed the occupancy of less than 3% for $\beta(1,3)$ and 10% for $\beta(1,4)$ isomers, suggesting minor or weak H-bonds. The occupancy of the major H-bond in $\beta(1,3)$ isomer was apparently greater than that in $\beta(1,4)$ isomer. This indicated the $\beta(1,3)$ H-bond is stronger than the $\beta(1,4)$ H-bond. Thus the conformation of the $\beta(1,3)$ linker is more rigid than that of $\beta(1,4)$. The H-bonds results strongly supported the conformational flexibility difference between the flexible $\beta(1,4)$ and the rigid $\beta(1,3)$ observed from the RMSD, R_g and the torsion distribution described previously. Therefore, the strength of H-bonds at the glycosidic linkers contributes structural flexibility of HA molecules.

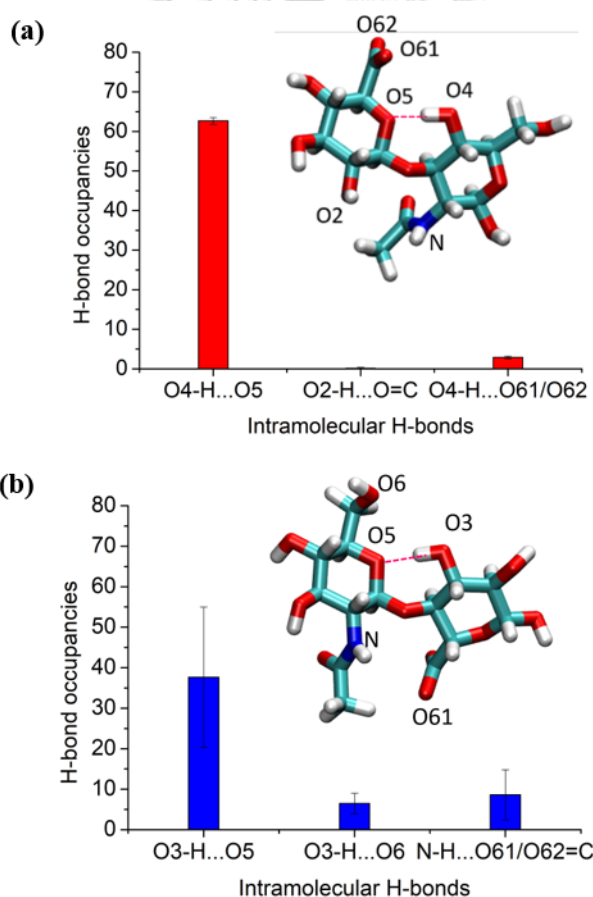


Figure 4.3 The occupancies of H-bonds between two saccharide rings connected together via glycosidic bonds of HA1 (displayed in stick representation) (a) $\beta(1,3)$ and (b) $\beta(1,4)$ isomers.

The strength of hydrogen bond is strongly dependent on the geometry of the hydrogen bond donor and acceptor. The average distances and angles of hydroxyl and carboxylate groups involved in H-bonds are summarized in [Table 4.1](#). We found that the H-bond geometry of the O3–H···O5 and O4–H···O5 pairs are closer to their optimal geometry of the H-bond criteria than those of other H-bonds. Moreover, O4–H···O5 has the better H-bond geometry than O3–H···O5. Based on the above results, it is inferred that the strength of intra-saccharide hydrogen bonds of $\beta(1,3)$ isomer are greater compared to that of $\beta(1,4)$ isomer. These H-bonds restrict movements of disaccharides rings. These explain why the disaccharide unit with $\beta(1,4)$ linkage is more flexible compared to that with the $\beta(1,3)$ linkage.

To provide further evidence for the different flexibility of the two glycosidic linkers, the low-energy conformation of HA1 with $\beta(1,3)$ and $\beta(1,4)$ isomers is determined by highly accurate ab initio calculations. The DFT geometric optimization was performed on at least three representative structures taken from the trajectories. The results showed that the energy of the HA1 conformation with the $\beta(1,4)$ linkage is +29.67 kJ/mol higher than the $\beta(1,3)$ energy ([Table 4.2](#)). This suggested that the $\beta(1,3)$ linkage has a more stable conformation than the $\beta(1,4)$. More details will be discussed in section 3.5. The distances of O4–H···O5 and O4–H···O61/O62 became shorter than its initial values and fell within the H-bond criteria after the geometry optimization ([Table 4.1](#)). The DFT results supported the conformational rigidity in $\beta(1,3)$ glycosidic bond is greater than that in $\beta(1,4)$ linkage.

Table 4.1 Distances and angles of inter-saccharide H-bonds at glycosidic bonds of HA1 obtained from MD simulations and from DFT geometry optimizations. X = H-bond donor or acceptor atoms

Systems	Interactions	From simulations		After DFT optimizations	
		X...X (Å)	XHX (°)	X...X (Å)	XHX (°)
$\beta(1,3)$	O4-H...O5	2.92 ± 0.27	128.7 ± 33.2	2.76 ± 0.01	142.5 ± 3.7
	O2-H...O=C	4.90 ± 0.56	110.9 ± 34.4	4.57 ± 0.33	83.7 ± 32.5
	O4-H...O61/O62	4.63 ± 0.64	120.5 ± 24.0	3.11 ± 0.05	138.6 ± 2.4
$\beta(1,4)$	O3-H...O5	3.17 ± 0.62	113.1 ± 43.7	2.87 ± 0.03	157.8 ± 0.3
	O3-H...O6	4.58 ± 1.04	104.5 ± 35.6	4.87 ± 0.11	154.7 ± 1.6
	N-H...O61/O62	4.44 ± 0.77	95.1 ± 36.0	3.91 ± 0.82	105.2 ± 44.4

4.1.2 Structure and flexibilities of HA chains

The RMSD, RMSF and R_g curves as a function of time for all systems (Figure S2) indicate that the HA structures of the studied sizes are in a relatively stable state for a small unit of disaccharides (HA1-HA10), but highly fluctuated for a larger unit (HA20-HA50). The RMSD, RMSF and R_g profiles of a short chain shown in Figure 4.4a revealed the stability of the conformation during the course of simulations whereas structural variant became more apparent for a long chain (Figure 4.4b). The structure deviation and the degree of R_g fluctuation indicated that the straight-chain conformations of HA5 as well as of HA10 (Figure S2c) are less affected compared to the long chain polymer. The changes in the rod-like structure during the equilibration are rather small. On the contrary, the time evolutions of RMSD, RMSF and R_g of HA30 shown in Figure 4.4b and of the long chain HA (Figure S2e-S2g) revealed a large change in conformation of the polymer. It should be noted that an increase in R_g for the long chain HA is not uncommon. The simulations with long HA chain (HA20, HA30, HA40 and HA50) started with a pre-folded conformation, which was taken from a vacuum simulation. Therefore, the conformational adjustment has been taken place to accommodate the solvent molecules. It is more importantly to note that the degree of fluctuations in R_g and RMSD values apparently increased as the size of HA increased, supporting a more structural variability with the chain length.

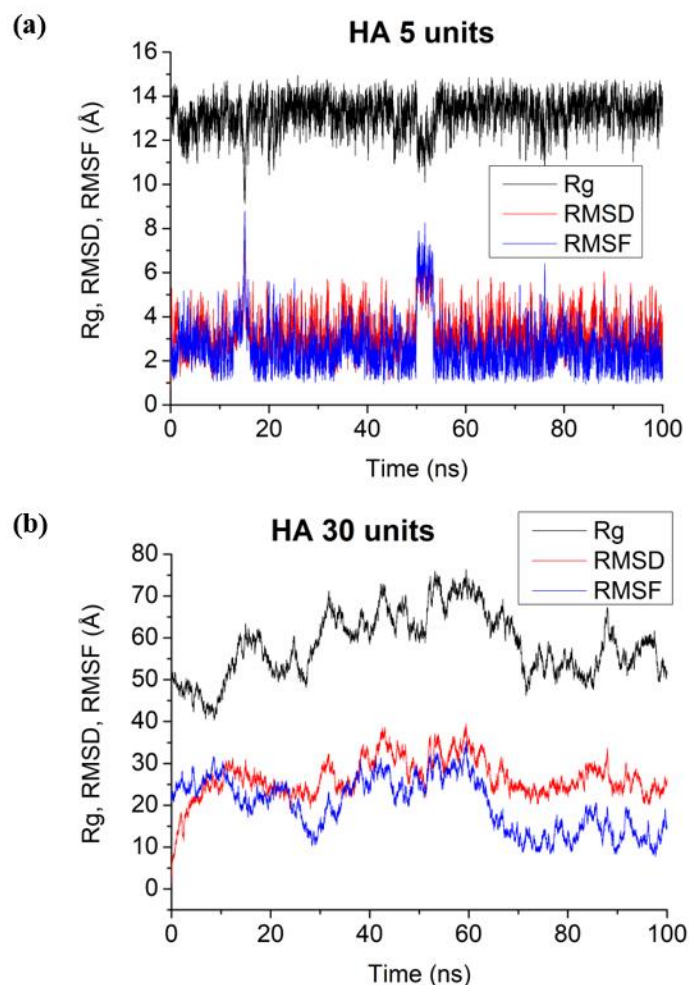


Figure 4.4 (a) and (b) show the structure fluctuations during the simulations of HA5 and HA30, respectively.

To demonstrate a tendency of the shape transformation of the polymer in association with the chain length, we plotted the average R_g value against the number of disaccharide units. Figure 4.5a showed the ratio of the R_g of the equilibrium structure to that of the HA straight-chain structure. HA1 is the smallest system and therefore the R_g ratio is approximately 1.0. For HA5 and HA10, the average ratios are 0.90 and 0.87, respectively. Apparently, the ratio decreases as the HA chain length increases. A meaningful insight can be developed by estimating the scaling exponent (ν) from the power-law scaling, $R_g \propto N^\nu$ where N is numbers of repeating unit i.e. monomers [59]. The value of ν closed to 1.0 implies a rod-like conformation of the polymer chain and a random-coil conformation with $\nu \sim 0.6$. The significance of

random coil shape is that segments of the polymer chain have a tendency to entangle with each other. Figure 4.5b showed the best-fitting straight line for two separate data sets. The first dataset includes R_g of HA with short chain lengths, i.e. $N = 1-20$ units and the second dataset covers R_g for $N=20-50$. The scaling exponents obtained by linear regression between $\ln R_g$ and $\ln N$ is 0.80 for the first dataset and 0.65 for the second dataset. This indicated that the overall conformation of the first dataset (short chains) are between rod-like and coil shape. On the other hand, ν of 0.65 for the second dataset (longer chains) suggested that the structures of HA with disaccharide units more than 20 are in favor of random coil conformations [22-24].

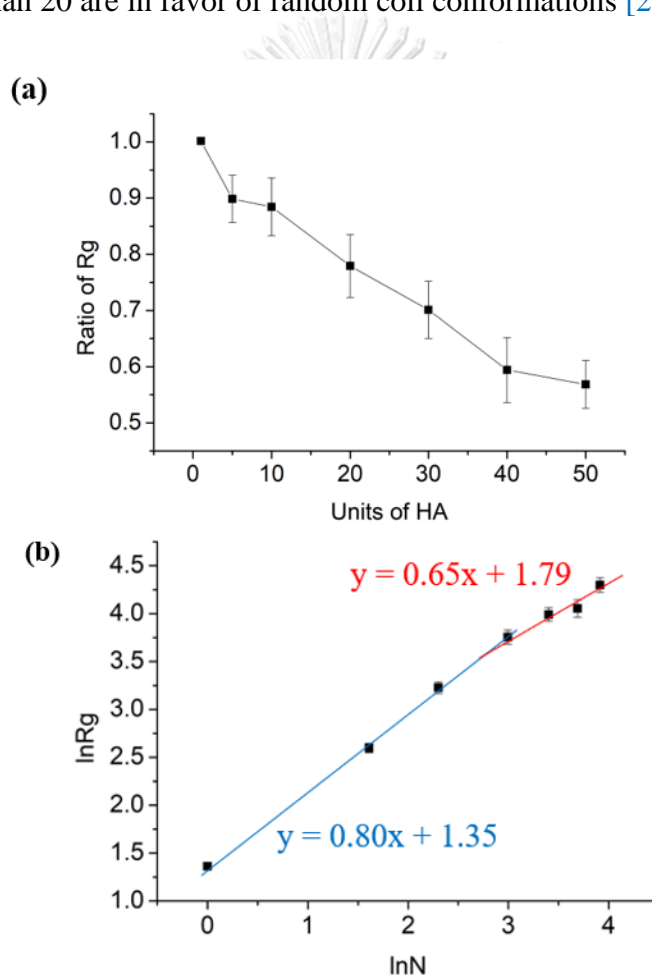


Figure 4.5 (a) The ratio of the R_g of equilibrated structures to the straight-chain conformation (b) The linear regressions between $\ln R_g$ and $\ln N$ ($N =$ units of HA) fitted with two datasets: HA1-HA20 and HA20-HA50.

In addition, the plot between RMSF and the number of disaccharide unit (Figure 4.6a) indicated that conformational mobility of the HA poly-disaccharide increases as the chain-length of the polymer increases. The HA polymers tend to adopt preferentially random coil shapes as the polymer increases in size. An analysis of the percentage occupancy of the major inter-saccharide H-bonds, O4–H···O5 for the $\beta(1,3)$ and O3–H···O5 for $\beta(1,4)$ glycosidic bonds is shown in Figure 4.6b. The percentage occupancy for the H-bond for $\beta(1,3)$ and $\beta(1,4)$ is approximately the same throughout the studied HA models. This suggests that H-bond is independent of the chain length of the HA polymer. However, the strength of the $\beta(1,4)$ H-bond is not as strong as the $\beta(1,3)$ H-bond.

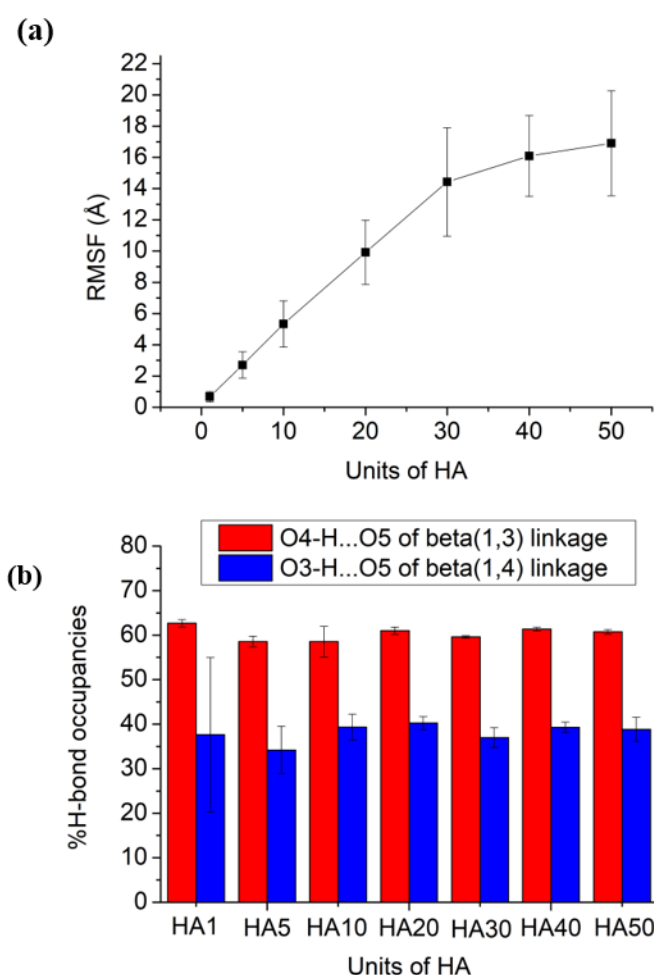


Figure 4.6 (a) The average RMSF compared to average structure of HA from last 20 ns for all systems. (b) The occupancies of the $\beta(1,3)$ and $\beta(1,4)$ major H-bonds for all HA systems.

4.1.3 Hydrations and solvation energy

Hydroxyl groups of HA are capable of forming H-bonds with water molecules. To illustrate interactions between HA and solvated water, we calculated the normalized radial pair distribution functions ($g(r)$) of water molecules around HA. The $g(r)$ plots were obtained over all selected pairs between hydrogen of water (H_w) and oxygen of HA (O_{HA}) for [Figure 4.7a](#) and between oxygen of water (O_w) and hydrogen of hydroxy group of HA (HOHA) for [Figure 4.7b](#) in all frames. Both graphs showed the amplitude of the peaks in the $g(r)$ decreases as the size of HA increases, but the shape of the $g(r)$ remains the same. The first hydration shell is indicated by the first sharp peak of the $g(r)$ at distance about 1.90 Å for the $H\cdots O$ in all chain sizes. This indicates that HA can be both hydrogen-bond donor and acceptor molecule. The first peak is the signature of the H-bond in the first shell while the second broad peak about 3.5 Å describes water in the second hydration shell having water exchange to bulk solution. We noted that the first peak of the $g(r)$ of HA1 is highest in amplitude, suggesting a maximum adsorption capacity of water. This result is as expected, since the solvent-exposed surface is limited for HA5-HA50.

Hydration property and free energy of solvation are linked to the water adsorption ability of HA polymers. It is clear that there are water molecules present in the first coordination shell of HA. Number of the first shell water increases with the chain length. The hydration number was determined by counting a total number of water molecules within the first RDF peak (1.5-2.8 Å) of HA and averaging over the last 20ns trajectory. [Figure 4.7c](#) shows the hydration number per disaccharide unit together with the MM/GBSA free energy of solvation (ΔG_{solv}) for all studied sizes. From the results, HA1 exhibited the highest hydration number and the lowest ΔG_{solv} . However, this is attributed by the presence of two additional OH groups in the two ending sugars, producing the “terminal end effect”. It is clear that the end effect is reduced with the size of the chain. As can be seen in [Figure 4.7c](#), the hydration number and ΔG_{solv} tend to converge towards a constant value as the HA size increases. The results were in good agreement with previous reports [26, 28, 60-61].

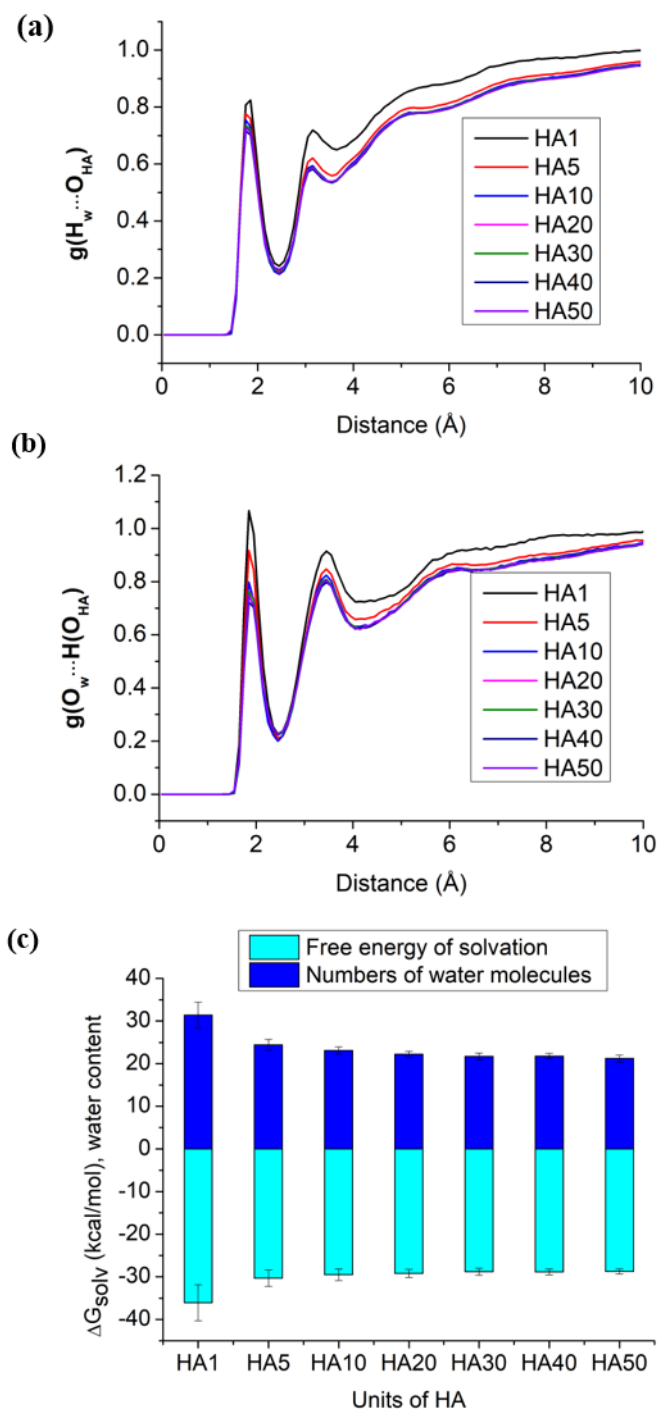


Figure 4.7 The normalized radial pair distribution functions between all sizes of HA and water that were calculated by (a) hydrogen of water and oxygen of HA and (b) oxygen of water and hydrogen from hydroxy group of HA. (c) The number of hydrated water molecules per disaccharide unit and free energies of solvation of HA per disaccharide unit

4.1.4 Cation binding

Due to a dissociation of carboxylic groups, HA exists in anionic form that can attract positively charged counter ions through an electrostatic interaction. The effect of ionic strength on the intrinsic viscosity has long been recognized by the well-known classic study of chain stiffness in polyelectrolytes introduced by Smidsrød and Haug [62]. Electrostatic interaction between polysaccharide chains and mobile ions affect its conformational and rheological properties. The binding of Na^+ and Cl^- to the HA was quantitatively described in terms of HA-ion radial distribution function. The $g(r)$ plots of $\text{Na}^+\cdots\text{carboxylate}$ oxygen of GlcA and $\text{Na}^+\cdots\text{hydroxy}$ oxygen of GlcNAc are shown in Figure 4.8a, b. The first peak of $g(\text{Na}^+\cdots\text{OOC})$ and $g(\text{Na}^+\cdots\text{OH})$ was located at 2.3 Å for HA structures of all studied sizes. It should be noted that there is only one carboxylate group and four hydroxy groups per disaccharide unit. From the magnitude of $g(r)$, the degree of binding to Na^+ at the GlcA carboxylates was much greater than the GlcNAc hydroxyls. This suggested the probability of the cation binding to the GlcA carboxylate is much higher than the hydroxyl groups.

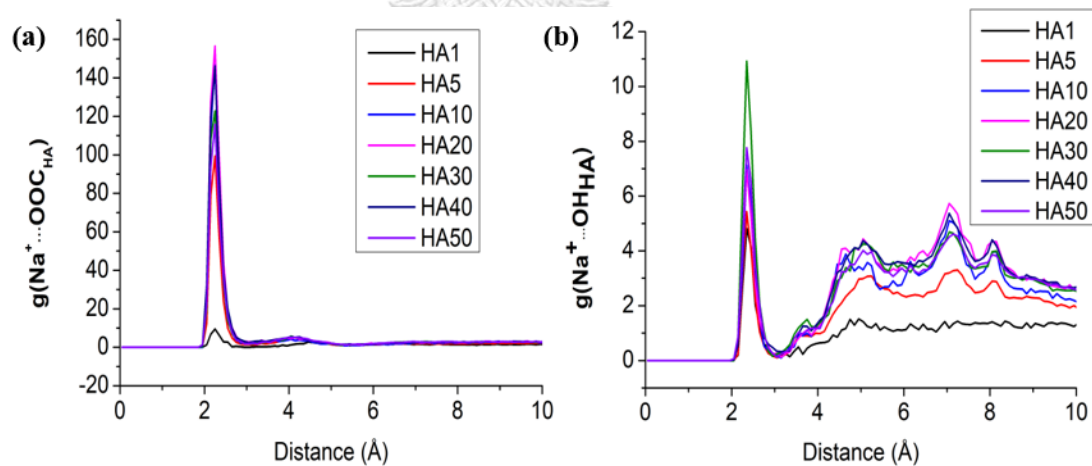


Figure 4.8 The radial pair distribution functions of (a) Na-COO of HA and (b) Na-OH of HA of all studied systems.

In addition, the probability of binding of HA to Na^+ was considerably high whilst that to Cl^- was very low (Figure 4.9a). This implies that Na^+ was able to bind to HA whereas the Cl^- did not. Each disaccharide unit of HA contains only one carboxylate, however, not all carboxylate sites were bound to Na^+ . Thus, we computed the number of Na^+ per disaccharide unit binding to HA by counting the number of Na^+ within 3 Å of HA, then dividing by the total disaccharide units of HA polymers, and averaging over the last 20ns MD trajectory. The results are shown in Figure 4.9b. The interpretation of the graph is as follows. For HA1, only 0.05 of Na^+ was obtained. This implied that Na^+ was actually not bound to HA. For HA10, the average Na^+ per unit was 0.17, indicating approximately 2 Na^+ was present in the molecule with ten carboxylate-binding sites. From Figure 4.9b, the number of Na^+ per disaccharide unit was in average ~ 0.15 Na^+ per unit for the HA chains ranging from 5 to 50 units. This demonstrated that Na^+ was always presented with about 15% of the binding sites for HA polymers of this range.

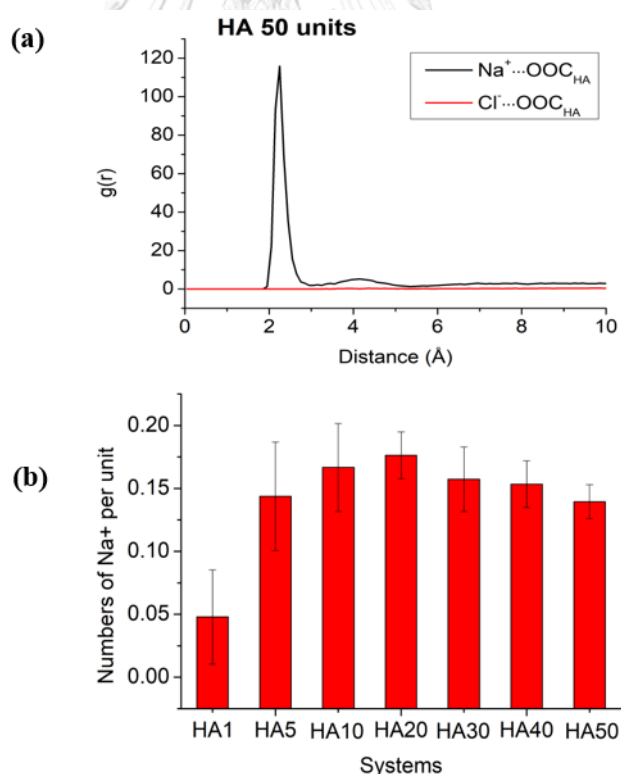


Figure 4.9 (a) Na^+ -COO and Cl^- -COO for HA50 (b) The numbers of Na^+ per disaccharide unit counted within 3 Å of HA, the value of HA1 is mean from both isomers.

Based on the $g(r)$ results, we showed that Na^+ always interacts with GlcA carboxylates at some sites present in both $\beta(1,3)$ and $\beta(1,4)$ glycosidic linkers (Figure 4.10a, b). In $\beta(1,3)$ configuration, Na^+ interacts with the O4 of hydroxyl group and O61/O62 of carboxylate group which substitutes the O4-H \cdots O5 H-bond (Figure 4.10a), the major contribution to the H-bond of the $\beta(1,3)$ glycosidic linkers. In contrast, Na^+ binds to O61/O62 of carboxylate group and an oxygen of amide group in $\beta(1,4)$ configuration which does not significantly disrupt the O3-H \cdots O5 H-bond (Figure 4.10b). The binding of Na^+ to HA at $\beta(1,4)$ site has been previously studied using DFT method [19-20]. Such binding geometry gave the lowest energy of the complex. As shown in Figure 4.10c, about 60-70% of Na^+ are bound to $\beta(1,4)$ configuration whereas binding of Na^+ in $\beta(1,3)$ configuration is only 30-40%. Thus the $\beta(1,4)$ binding site is more favorable than the $\beta(1,3)$ configuration for the binding of Na^+ . In other words, the affinity of Na^+ is higher for the $\beta(1,4)$ site than that for the $\beta(1,3)$ site.

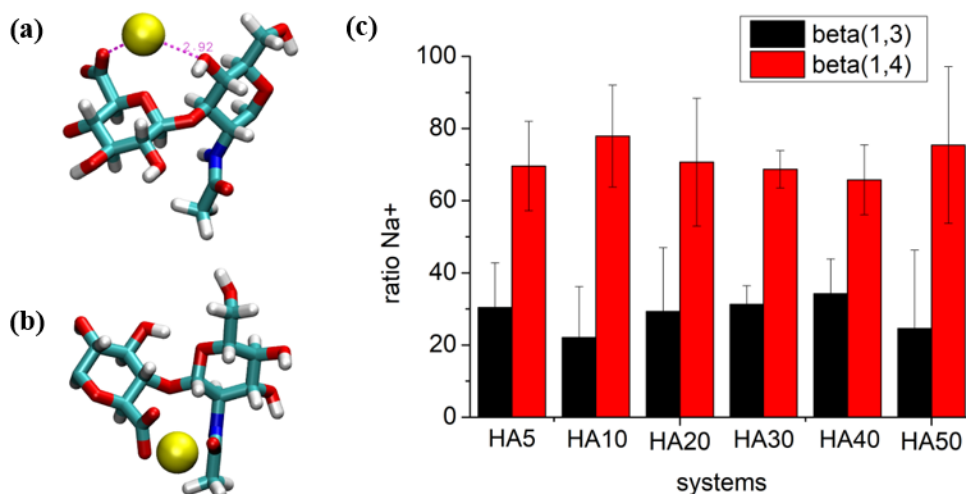


Figure 4.10 The binding mode of the $\beta(1,3)$ (a) and $\beta(1,4)$ (b) isomers to Na^+ . (c) The percent proportion of Na^+ found within 5 Å of glycosidic oxygen atom.

4.1.5 Distribution of torsion angles

As has been shown for HA1, the conformational flexibility appears to be associated with the variation of torsion angles at the $\beta(1,4)$ glycosidic bond. Therefore, the glycosidic torsion angles can provide an insight into the conformational variation in the HA poly-disaccharide. All MD data of the HA systems with multiple disaccharide units ranging from 10 to 50 units were used to generate conformational ensembles for extracting ϕ and ψ values. It was found that the plot of $\beta(1,3)$ glycosidic torsion angles (ϕ_{13} , ψ_{13}) exhibits only one cluster with a narrow range of distribution similar to that observed in HA1 (Figure 4.2a, 4.11a). The $\beta(1,4)$ linker of disaccharide units, on the other hand, showed a more variety of conformations. The distribution was spread out more than one region, which can be clustered into four regions, A–D (Figure 4.11b). Region A centered around $(\phi, \psi) \sim (60^\circ, 0^\circ)$, is the most populated conformations whereas the other regions have a lower population (Table 4.2).

The different (ϕ, ψ) distributed regions of the $\beta(1,4)$ linker was involved with different H-bond interactions. Analysis of H-bond showed that the O3-H \cdots O5 H-bond was frequently observed in the A region. The B region is centered around $(30^\circ, -30^\circ)$ where the O3-H \cdots O5 H-bond was rarely formed. The O3-H \cdots O6 and O6-H \cdots O3 H-bonds were detected instead (Figure 4.11b, c). In addition, the N-H \cdots O61/O62=C H-bond was found in both region A and B. The distribution in the C region has a centroid around $(50^\circ, 150^\circ)$ with the H-bond between O6H and carboxylate group (Figure 4.11b,c) while the D region is centered at $(70^\circ, -150^\circ)$ with no H-bond. The distributions of the torsion angles are in good agreement with a previous study for a long HA chain using Monte-Carlo simulations [22]. It is unfortunate that no experimental NMR structure is available for large size HA. Therefore, we cannot make a direct comparison with the experiment. However, an NMR structure of a small HA molecule with only 4 units of disaccharide is available with PDB code 2bvk. To verify, we measure the phi-psi angles of the NMR structure (PDB 2bvk) and made a comparison by taking the ϕ - ψ distribution from the simulation of HA of similar size (5 units). The result still shows a good agreement between the experiment and simulation data (Figure S4).

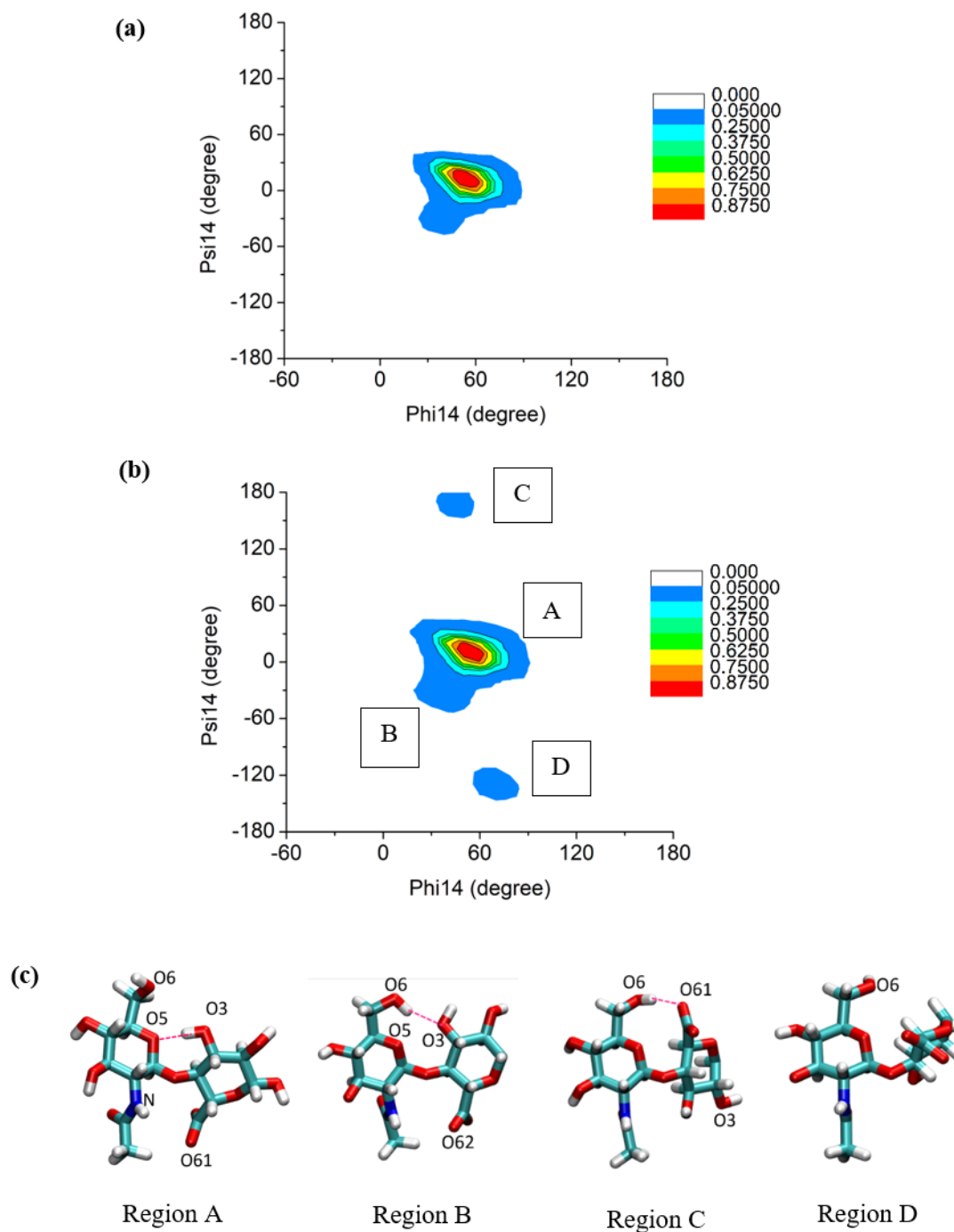


Figure 4.11 The (ϕ , ψ) distribution of all positions of $\beta(1,4)$ linker of (a) HA5 (50,000 data) and (b) HA40 (400,000 data) (c) Representative conformations of region A, B, C and D.

The regions A–D are further evaluated by calculating conformational energy based on DFT. A single point energy calculation was carried out before and after DFT geometry optimization of the structure taken from MD snapshots. In this calculation, structures consisting only one disaccharide unit from the HA10-HA50 polysaccharide systems were used in a similar manner to those which were done on the HA1 model. The conformations for DFT calculation were prepared by cutting only one disaccharide unit from the whole structure of the HA poly-disaccharide systems. The selected conformations were based on the ϕ , ψ values corresponding to the centroid of each cluster of the plots shown in [Figure 4.11b](#). Thus, we have a representative conformation for the $\beta(1,3)$ isomer and four representative conformations corresponding to regions A–D for the $\beta(1,4)$ isomer. In overall, a total of five HA models (denoted as **1**, **2**, **3**, **4** and **5**) was subjected to DFT optimizations at B3LYP/6-31G* in implicit water CPCM solvent. Results of three independent runs are shown in [Table 4.2](#). It is clear that the $\beta(1,4)$ model **2**, **4** and **5** are higher in energy than the $\beta(1,3)$ model **1**. In other words, the $\beta(1,4)$ model **2**, **4** and **5** are less stable than the $\beta(1,3)$ model **1**. It should be noted that Na^+ stabilizing conformation in the $\beta(1,4)$ model **2** and **4** was not included in the energy calculation. The presence of Na^+ binding to these models could make the complex being more stable. The $\beta(1,4)$ model **5** is the least stable since there is no hydrogen bonding within the molecule. Interestingly, the $\beta(1,4)$ model **3** had a double H-bond, and thus gave the energy lower than the $\beta(1,3)$ model **1**. However, we found that this conformation was rarely present in the conformational ensembles. One of the two H-bonds in this conformation is not as strong as the $\beta(1,3)$ model **1**. Similarly, an examination of the MD trajectory revealed that a double H-bond for $\beta(1,3)$ was observed with a low population. The $\beta(1,3)$ isomer formed two inter-saccharide H-bonds, one of which is stronger than the other. The weak H-bond is lost during the simulations because of the interaction with solvent molecules. Moreover, the net atomic charges of hydroxy groups obtained from DFT calculations showed that the oxygen atom (O4) of the $\beta(1,3)$ model **1** has the highest negative charge compared to the other oxygen atoms from all $\beta(1,4)$ models ([Table 4.2](#)). This observation strongly supported the conformation rigidity of the $\beta(1,3)$ linker due to the strength of hydrogen bond.

Table 4.2 Overlay structures before (blue) and after (green) optimization, H-bonds (dash lines), relative energies, net atomic charges and population ratios from 5 representative structure of the clusters

		Representative structure of the clusters				
		$\beta(1,4)$				
		1	2(A)	3(B)	4(C)	5(D)
Overlay structures ^a						
RMSD(Å)		0.584	0.924	0.982	0.347	0.276
Relative energy (kJ/mol) ^b		0	+29.67	-4.54	+24.73	+64.56
Net atomic charges ^c		O4 = -0.709 H = +0.447	O3 = -0.695 H = +0.429	O6 = -0.650 H = +0.426	O6 = -0.649 H = +0.429	-
Population ratio ^d		1.0	0.80	0.13	0.03	0.04

^a Structures before optimization were selected from the centroid of each clusters. RMSD was calculated with all non-hydrogen atom in HA structure.

^b Energies are reported with respect to the model **1**.

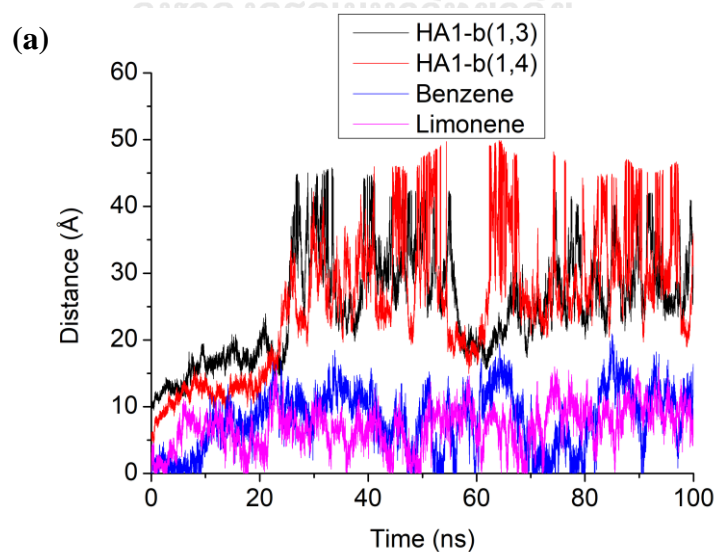
^c Net atomic charges of hydroxy group forming H-bond from each structure.

^d Population ratios averaged over the trajectories of HA20, HA30, HA40 and HA50.

4.2 Transfer of HA across membranes

4.2.1 Stability of HA1 near the membrane center

Stability of HA1 within phospholipid membrane was compared to non-polar molecules such as benzene and (+)-limonene. The RMSD curves as a function of time for HA1 and two non-polar molecules were shown in Figure S6. For the starting position, the center of mass for all studied molecules was placed close to the membrane center ($z=0$). Both isomers of HA1 rapidly moved away from the hydrophobic center as indicated by a sharp increase in distance from 0 to 10 Å at a very beginning of the simulations (Figure 4.12a), and HA molecules have moved from origin position since equilibration phase (Figure 4.12b). Then, the HA1 position gradually increased from 10 to 20 Å for about 25 ns before detaching and re-attaching the membrane (the fluctuation of 20-50 Å distance) afterward until the end of simulations. This suggested that HA1 can be temporarily trapped within the lipid-water interface. From the results, HA1 was not stable when it approaches to the membrane center, but appeared to be relatively more stable near the polar head groups of the lipid and in bulk water. On the other hand, two non-polar molecules, benzene and (+)-limonene, were found to be stable within the hydrophobic region of the membrane.



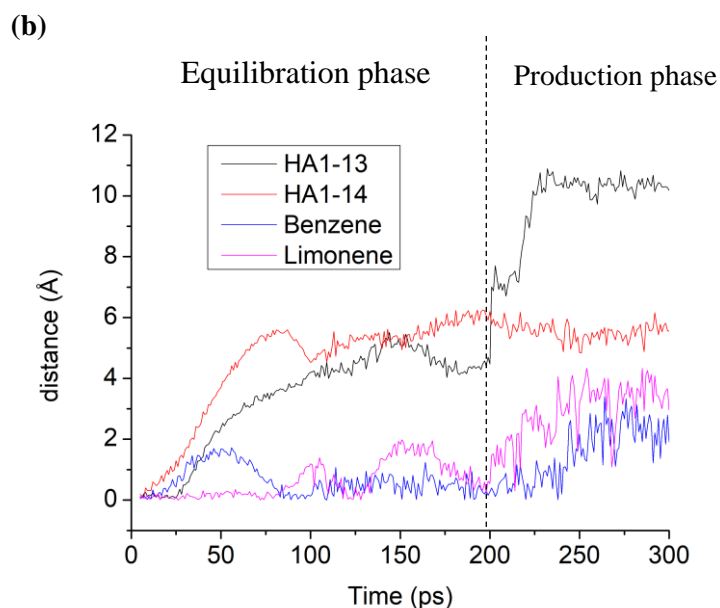


Figure 4.12 (a) Plots of z-position of the center of mass of examined molecules as a function of time and **(b)** the magnified graph showing the first 100 ps from figure (a) including 200 ps from equilibration step, the initial position of the molecules was set at center of membrane. The center of mass of phospholipid bilayers were the origin of the coordinate and the membrane region corresponds to the distance values between -20 to +20 Å.

4.2.2 Stability of HA1 near the lipid-water interface

Next, the examined molecules were placed near the lipid-water interface (the starting distances of about 20 Å). The HA1 position appeared to fluctuate with a distance of about 20-50 Å during the course of simulations. This suggests that HA1 detached and re-attached the polar part of membranes. However, HA1 molecules were not able to move further towards the center hydrophobic due to the steric repulsion. For benzene and (+)-limonene, the distance decreases from 20 Å to 0-10 Å (Figure 4.13). It illustrates that they can passively penetrate deep into the hydrophobic region of the bilayers.

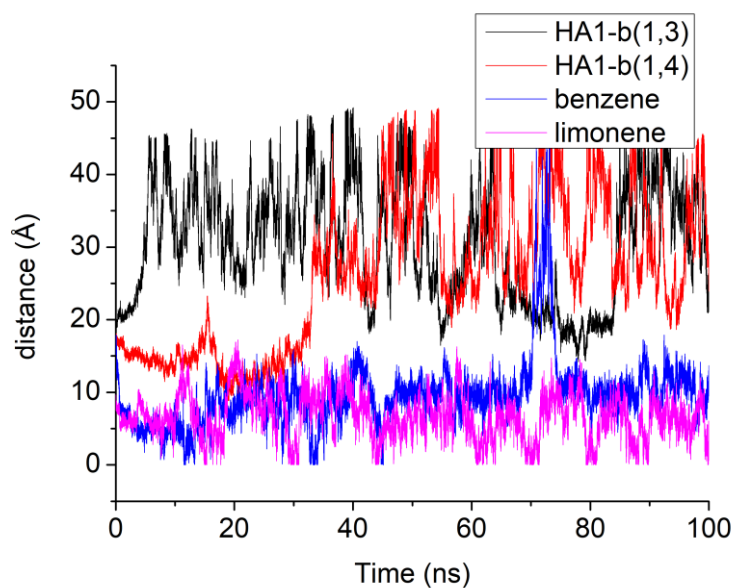


Figure 4.13 Plots of z-position of the center of mass of focused organic as a function of time, the initial position of organic molecules was set at phosphate group or membrane surface (partial membrane region). The center of mass of phospholipid bilayers were the origin of the coordinate and the membrane region corresponds to the distance values between -20 to +20 Å.

4.2.3 Stability of HA5

The MD results of HA5 were similar to those of HA1, in a way that the hydrophobic region of the lipid is unfavorable. It is no matter how HA5 was placed at the membrane center or the interface. HA5 moved away from the membrane center (Figure 4.14).

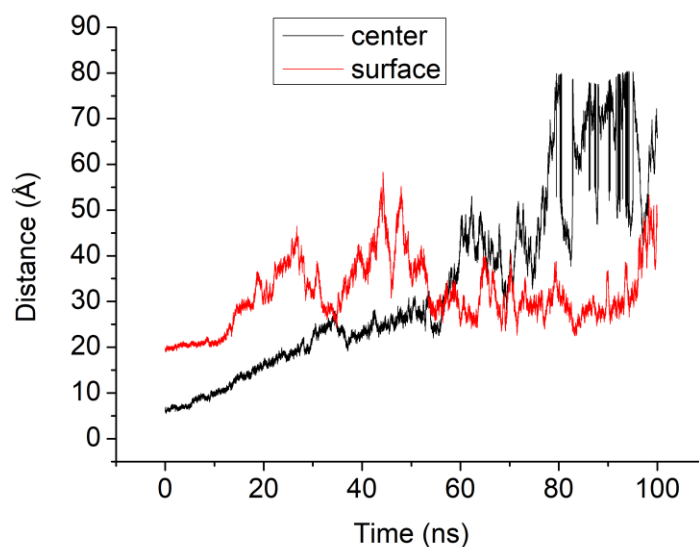


Figure 4.14 Plots of z-position of the center of mass of HA5 as a function of time, the initial positions of HA5 was set at center of membrane (black color) and phosphate group or membrane surface (red color). The center of mass of phospholipid bilayers were the origin of the coordinate and the membrane region corresponds to the distance values between -20 to +20 Å.

4.2.4 Free energy of transfer of HA across membranes.

At the beginning of SMD (-30 to -20 Å), all examined molecules were in aqueous, thus two isomers of HA1 showed an energy barrier lower than benzene and (+)-limonene. Then, the free energy barrier increases as HA1 was transferred from aqueous environment into the phospholipid bilayer whereas the two non-polar molecules exhibited an opposite effect. It was found that the transfer free energy of HA1 through the membrane corresponds to ~40 kcal/mol (Figure 4.15).

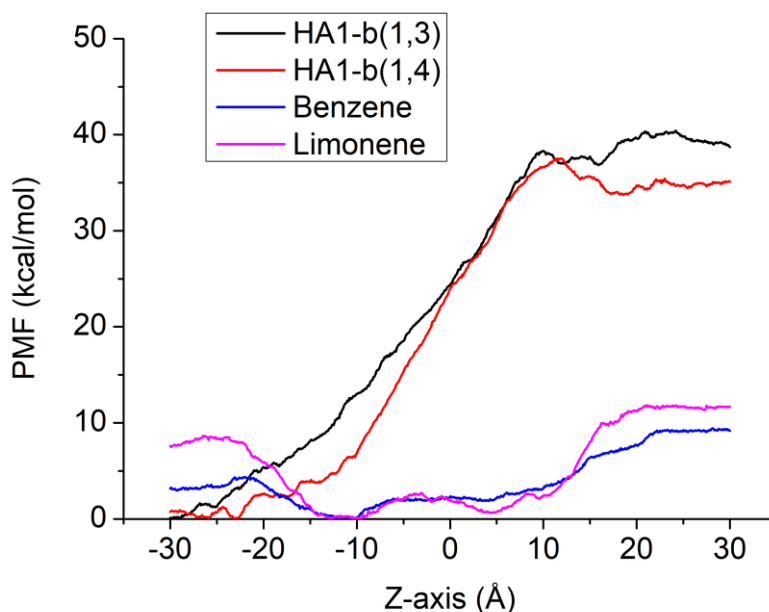


Figure 4.15 PMF of benzene, limonene and HA1

The shape of graphs for benzene and (+)-limonene are similar as the shapes of another non-polar molecules such as toluene, styrene and phenol from previous research [63]. The decrease of free energy of benzene and (+)-limonene after passing aqueous phase without significant barrier at hydrophilic head through hydrophobic phase of membrane indicates ability of passive transport like fullerene [64]. However, shape of graph from HA1 does not look like bell shaped curve or have a symmetry, while other hydrophilic molecules such as ethanol, acetic acid and DMSO behave those [63]. The possible reasons are that HA molecules are quite large and can bring some amount of water that stabilizes HA structures and they cause free energies of HA not to dramatically increase at -20 to -10 Å period and have local maximum at 0 Å. After HA penetrate the membrane to aqueous phase again, they have high energies and are unstable so the periods of +20 to +30 Å are not enough to stabilize HA structure to have the low energies again.

CHAPTER 5

CONCLUSION

5.1 MD simulations in water

MD simulations of low molecular weight hyaluronic acid (LMW-HA) with $N = 1, 5, 10, 20, 30, 40$ and 50 repeating units in aqueous solution have been carried out. Effect of the chain size of HA polymer on its conformation, flexibility, shape and hydration were investigated. The preliminary simulations in vacuum illustrate that HA can behave a variety of shape and conformation due to high fluctuation of radius of gyrations (R_g). In addition, the longer chains of HA have greater folds to be random-coil shapes because of lower values of R_g per disaccharide unit. For MD simulation in water, we obtained the scaling exponents of HA by linear regression between $\ln R_g$ and $\ln N$. The conformation of the HA polymer chains appears to be more extended (rod-like) for short length ($N = 1-10$) with scaling exponent equal to 0.80 . With increasing polymer chain length, the magnitude of conformational flexibility increases. A crossover from rod-like shape to random-coil conformations occurs on increasing the molecular weight ($N = 20-50$) with scaling exponent equal to 0.65 . As shown by MD and DFT data, the two alternate glycosidic linkers, $\beta(1,3)$ and $\beta(1,4)$ exhibited different flexibility, which involves the conformation variability of the HA poly-disaccharide. For the studied models, the $\beta(1,3)$ linker has more a conformational rigidity than the $\beta(1,4)$ linker. The conformational fluctuation as well as variation of the radius of gyration are found to be associated with the flexibility at the $\beta(1,4)$ linker.

Radial distribution functions of HA-water indicate larger sizes of HA have lower water content in the first hydration shell and lower magnitudes of free energies of solvation per repeating units. Moreover, Glucuronic carboxylates appear to be a cation interaction site with being more favorable at the $\beta(1,4)$ linkage. Inter-saccharide hydrogen bonding and the cation binding make a contribution to the stability of random coil conformations. This study proposes that $\beta(1,4)$ glycosidic

bonds play a significant role in controlling polymer conformation, flexibility and shape transformation.

5.2 MD simulations in membrane

MD simulations of hyaluronic acid with 1 and 5 disaccharide units (HA1 and HA5) in membrane system were carried out. Both sizes of HA have unstable interaction with phospholipid membrane owing to hydrophilic property. HA at the center of membrane move out to bulk solution at early simulations and HA at the membrane surface cannot penetrate to the core membrane, while non-polar molecules are stable in core membrane. Furthermore, free energy changes of HA1, benzene and (+)-limonene during membrane penetration by SMD simulation correspond to previous results from distance analysis. Thus, this study presents that HA1 and HA5 cannot permeate through membrane by passive transport.

5.3 Limitations and future work

Although our simulations were expected to explain the real systems, there are still some limitations. For example, there was only one HA molecule in a periodic boundary box thus solute-solute interactions were not taken into account from our simulations. In addition, extracellular fluid in human has a variety type of ions but only sodium and chloride ions present in our simulations. We also have limitation of our computational resource. With a limit of computational resources, an all-atom MD simulation of large HA polysaccharides (>HA50) are very time-consuming and really not practical. In our future work, we could extend our study to the systems that include HA-HA interaction and investigate how structural and hydration properties change. The simulations containing other ions in systems are also a challenge because some ions may have roles about membrane permeation of HA.

REFERENCES

1. Fransson, L., Mammalian polysaccharide In: Aspinall O (Ed). The Ploysaccharides Vol. 3. Academic Press, New York: 1985.
2. Robyt, J. F., *Essentials of carbohydrate chemistry*. Springer Science & Business Media: 2012.
3. Stern, R., Devising a pathway for hyaluronan catabolism: are we there yet? *Glycobiology* **2003**, *13* (12), 105R-115R.
4. Necas, J.; Bartosikova, L.; Brauner, P.; Kolar, J., Hyaluronic acid (hyaluronan): a review. *Vet. Med.* **2008**, *53* (8), 397-411.
5. Jiang, D.; Liang, J.; Noble, P. W., Hyaluronan in tissue injury and repair. *Annu. Rev. Cell Dev. Biol.* **2007**, *23*, 435-461.
6. Collins, M. N.; Birkinshaw, C., Hyaluronic acid based scaffolds for tissue engineering—A review. *Carbohydr. Polym.* **2013**, *92* (2), 1262-1279.
7. Murugan, R.; Ramakrishna, S., Design strategies of tissue engineering scaffolds with controlled fiber orientation. *Tissue Eng.* **2007**, *13* (8), 1845-1866.
8. Prestwich, G. D., Hyaluronic acid-based clinical biomaterials derived for cell and molecule delivery in regenerative medicine. *J. Control. Release* **2011**, *155* (2), 193-199.
9. Beasley, K. L.; Weiss, M. A.; Weiss, R. A., Hyaluronic acid fillers: a comprehensive review. *Facial Plast. Surg.* **2009**, *25* (02), 086-094.
10. Farwick, M.; Lersch, P.; Strutz, G., Low molecular weight hyaluronic acid: its effects on epidermal gene expression & skin ageing. *SÖFW J.* **2008**, *134* (11), 17.
11. Sze, J. H.; Brownlie, J. C.; Love, C. A., Biotechnological production of hyaluronic acid: a mini review. *3 Biotech* **2016**, *6* (1), 67.
12. Atkins, E.; Sheehan, J., Structure for hyaluronic acid. *Nature New Biol.* **1972**, *235* (60), 253-254.
13. Atkins, E.; Meader, D.; Scott, J., Model for hyaluronic acid incorporating four intramolecular hydrogen bonds. *Int. J. Biol. Macromol.* **1980**, *2* (5), 318-319.
14. Sheehan, J.; Atkins, E., X-ray fibre diffraction study of conformational changes in hyaluronate induced in the presence of sodium, potassium and calcium cations. *Int. J. Biol. Macromol.* **1983**, *5* (4), 215-221.
15. Holmbeck, S. M.; Petillo, P. A.; Lerner, L. E., The solution conformation of hyaluronan: a combined NMR and molecular dynamics study. *Biochemistry* **1994**, *33* (47), 14246-14255.
16. Almond, A.; Sheehan, J. K.; Brass, A., Molecular dynamics simulations of the two disaccharides of hyaluronan in aqueous solution. *Glycobiology* **1997**, *7* (5), 597-604.
17. Almond, A.; Brass, A.; Sheehan, J., Deducing polymeric structure from aqueous molecular dynamics simulations of oligosaccharides: predictions from simulations of hyaluronan tetrasaccharides compared with hydrodynamic and X-ray fibre diffraction data. *J. Mol. Biol.* **1998**, *284* (5), 1425-1437.
18. Bayraktar, H.; Akal, E.; Sarper, O.; Varnali, T., Modeling glycosaminoglycans—hyaluronan, chondroitin, chondroitin sulfate A, chondroitin sulfate C and keratan sulfate. *J. Mol. Struc-Theochem* **2004**, *683* (1-3), 121-132.
19. Pogány, P.; Kovács, A., Conformational properties of the disaccharide building units of hyaluronan. *Carbohydr. Res.* **2009**, *344* (13), 1745-1752.
20. Pogány, P.; Kovács, A., Theoretical study of hyaluronan oligosaccharides. *Struct. Chem.* **2010**, *21* (6), 1185-1194.

21. Almond, A.; DeAngelis, P. L.; Blundell, C. D., Hyaluronan: the local solution conformation determined by NMR and computer modeling is close to a contracted left-handed 4-fold helix. *J. Mol. Biol.* **2006**, *358* (5), 1256-1269.
22. Furlan, S.; La Penna, G.; Perico, A.; Cesàro, A., Hyaluronan chain conformation and dynamics. *Carbohydr. Res.* **2005**, *340* (5), 959-970.
23. Hargittai, I.; Hargittai, M., Molecular structure of hyaluronan: an introduction. *Struct. Chem.* **2008**, *19* (5), 697-717.
24. Ingr, M.; Kutáľková, E.; Hrnčírřík, J., Hyaluronan random coils in electrolyte solutions—A molecular dynamics study. *Carbohydr. Polym.* **2017**, *170*, 289-295.
25. Cilurzo, F.; Vistoli, G.; Gennari, C. G.; Selmin, F.; Gardoni, F.; Franzè, S.; Campisi, M.; Minghetti, P., The role of the conformational profile of polysaccharides on skin penetration: the case of hyaluronan and its sulfates. *Chem. Biodivers.* **2014**, *11* (4), 551-561.
26. Průšová, A.; Šmejkalová, D.; Chytil, M.; Velebný, V.; Kučerík, J., An alternative DSC approach to study hydration of hyaluronan. *Carbohydr. Polym.* **2010**, *82* (2), 498-503.
27. Hunger, J.; Bernecker, A.; Bakker, H. J.; Bonn, M.; Richter, R. P., Hydration dynamics of hyaluronan and dextran. *Biophys. J.* **2012**, *103* (1), L10-L12.
28. Alber, C.; Engblom, J.; Falkman, P.; Kocherbitov, V., Hydration of hyaluronan: Effects on structural and thermodynamic properties. *J. Phys. Chem. B* **2015**, *119* (11), 4211-4219.
29. Wieland, D. F.; Degen, P.; Zander, T.; Gayer, S.; Raj, A.; An, J.; Dédinaitè, A.; Claesson, P.; Willumeit-Römer, R., Structure of DPPC-hyaluronan interfacial layers—effects of molecular weight and ion composition. *Soft Matter* **2016**, *12* (3), 729-740.
30. Siódmiak, J.; Beldowski, P.; Auge, W. K.; Ledziński, D.; Śmigiel, S.; Gadomski, A., Molecular dynamic analysis of hyaluronic acid and phospholipid interaction in tribological surgical adjuvant design for osteoarthritis. *Molecules* **2017**, *22* (9), 1436.
31. Beldowski, P.; Kruszevska, N.; Yuwan, S.; Dendzik, Z.; Goudoulas, T.; Gadomski, A., Capstan-like mechanism in hyaluronan-phospholipid systems. *Chem. Phys. Lipids* **2018**, *216*, 17-24.
32. Herzog, M.; Li, L.; Galla, H.-J.; Winter, R., Effect of hyaluronic acid on phospholipid model membranes. *Colloid. Surface. B* **2019**, *173*, 327-334.
33. Cramer, C. J., *Essentials of computational chemistry: theories and models*. John Wiley & Sons: 2013.
34. Jensen, F., *Introduction to computational chemistry*. John Wiley & Sons: 2017.
35. Hug, S., Classical molecular dynamics in a nutshell. In *Biomolecular Simulations*, Springer: 2013; pp 127-152.
36. MacKerell Jr, A. D.; Banavali, N.; Foloppe, N., Development and current status of the CHARMM force field for nucleic acids. *Biopolymers* **2000**, *56* (4), 257-265.
37. Patel, S.; Mackerell Jr, A. D.; Brooks III, C. L., CHARMM fluctuating charge force field for proteins: II protein/solvent properties from molecular dynamics simulations using a nonadditive electrostatic model. *J. Comput. Chem.* **2004**, *25* (12), 1504-1514.
38. Klauda, J. B.; Venable, R. M.; Freites, J. A.; O'Connor, J. W.; Tobias, D. J.; Mondragon-Ramirez, C.; Vorobyov, I.; MacKerell Jr, A. D.; Pastor, R. W., Update of the CHARMM all-atom additive force field for lipids: validation on six lipid types. *J. Phys. Chem. B* **2010**, *114* (23), 7830-7843.
39. Guvench, O.; Mallajosyula, S. S.; Raman, E. P.; Hatcher, E.; Vanommeslaeghe, K.;

- Foster, T. J.; Jamison, F. W.; MacKerell Jr, A. D., CHARMM additive all-atom force field for carbohydrate derivatives and its utility in polysaccharide and carbohydrate–protein modeling. *J. Chem. Theory Comput.* **2011**, *7* (10), 3162-3180.
40. Price, D. J.; Brooks III, C. L., A modified TIP3P water potential for simulation with Ewald summation. *J. Chem. Phys.* **2004**, *121* (20), 10096-10103.
41. Isralewitz, B.; Gao, M.; Schulten, K., Steered molecular dynamics and mechanical functions of proteins. *Curr. Opin. Struct. Biol.* **2001**, *11* (2), 224-230.
42. Lemkul, J. A.; Bevan, D. R., Assessing the stability of Alzheimer's amyloid protofibrils using molecular dynamics. *J. Phys. Chem. B* **2010**, *114* (4), 1652-1660.
43. Patel, J. S.; Berteotti, A.; Ronsisvalle, S.; Rocchia, W.; Cavalli, A., Steered molecular dynamics simulations for studying protein–ligand interaction in cyclin-dependent kinase 5. *J. Chem. Inf. Model.* **2014**, *54* (2), 470-480.
44. Roux, B., The calculation of the potential of mean force using computer simulations. *Comput. Phys. Commun.* **1995**, *91* (1-3), 275-282.
45. Becke, A. D., Density-functional exchange-energy approximation with correct asymptotic behavior. *Phys. Rev. A* **1988**, *38* (6), 3098.
46. Becke, A. D., Density-functional thermochemistry. I. The effect of the exchange-only gradient correction. *J. Chem. Phys.* **1992**, *96* (3), 2155-2160.
47. Stephens, P. J.; Devlin, F.; Chabalowski, C.; Frisch, M. J., Ab initio calculation of vibrational absorption and circular dichroism spectra using density functional force fields. *J. Phys. Chem.* **1994**, *98* (45), 11623-11627.
48. Hehre, W. J.; Stewart, R. F.; Pople, J. A., self-consistent molecular-orbital methods. i. use of gaussian expansions of Slater-type atomic orbitals. *J. Chem. Phys.* **1969**, *51* (6), 2657-2664.
49. Brooks, B. R.; Brooks III, C. L.; Mackerell Jr, A. D.; Nilsson, L.; Petrella, R. J.; Roux, B.; Won, Y.; Archontis, G.; Bartels, C.; Boresch, S., CHARMM: the biomolecular simulation program. *J. Comput. Chem.* **2009**, *30* (10), 1545-1614.
50. Jo, S.; Kim, T.; Iyer, V. G.; Im, W., CHARMM-GUI: a web-based graphical user interface for CHARMM. *J. Comput. Chem.* **2008**, *29* (11), 1859-1865.
51. Humphrey, W.; Dalke, A.; Schulten, K., VMD: visual molecular dynamics. *J. Mol. Graphics* **1996**, *14* (1), 33-38.
52. Phillips, J. C.; Braun, R.; Wang, W.; Gumbart, J.; Tajkhorshid, E.; Villa, E.; Chipot, C.; Skeel, R. D.; Kale, L.; Schulten, K., Scalable molecular dynamics with NAMD. *J. Comput. Chem.* **2005**, *26* (16), 1781-1802.
53. Frisch, M.; Trucks, G.; Schlegel, H.; Scuseria, G.; Robb, M.; Cheeseman, J.; Scalmani, G.; Barone, V.; Mennucci, B.; Petersson, G., Gaussian 09, Revision A02. Wallingford: Gaussian, Inc.,–2009.–245 p **2009**.
54. Hess, B.; Bekker, H.; Berendsen, H. J.; Fraaije, J. G., LINCS: a linear constraint solver for molecular simulations. *J. Comput. Chem.* **1997**, *18* (12), 1463-1472.
55. Miyamoto, S.; Kollman, P. A., Settle: An analytical version of the SHAKE and RATTLE algorithm for rigid water models. *J. Comput. Chem.* **1992**, *13* (8), 952-962.
56. Genheden, S.; Ryde, U., The MM/PBSA and MM/GBSA methods to estimate ligand-binding affinities. *Expert Opin. Drug Dis.* **2015**, *10* (5), 449-461.
57. Takano, Y.; Houk, K., Benchmarking the conductor-like polarizable continuum model (CPCM) for aqueous solvation free energies of neutral and ionic organic molecules. *J. Chem. Theory Comput.* **2005**, *1* (1), 70-77.
58. Essendoubi, M.; Gobinet, C.; Reynaud, R.; Angiboust, J.; Manfait, M.; Piot, O.,

Human skin penetration of hyaluronic acid of different molecular weights as probed by Raman spectroscopy. *Skin Res. Technol.* **2016**, *22* (1), 55-62.

59. Rubinstein, M.; Colby, R., Polymer Physics, Oxford University Press. *New York* **2003**.

60. Kaufmann, J.; Möhle, K.; Hofmann, H.-J.; Arnold, K., Molecular dynamics study of hyaluronic acid in water. *J. Mol. Struct-Theochem* **1998**, *422* (1-3), 109-121.

61. Mlčoch, T.; Kučerík, J., Hydration and drying of various polysaccharides studied using DSC. *J. Therm. Analysis* **2013**, *113* (3), 1177-1185.

62. Smidsrød, O.; Haug, A., Estimation of the relative stiffness of the molecular chain in polyelectrolytes from measurements of viscosity at different ionic strengths. *Biopolymers* **1971**, *10* (7), 1213-1227.

63. Gupta, R.; Sridhar, D.; Rai, B., Molecular dynamics simulation study of permeation of molecules through skin lipid bilayer. *J. Phys. Chem. B* **2016**, *120* (34), 8987-8996.

64. Bedrov, D.; Smith, G. D.; Davande, H.; Li, L., Passive transport of C60 fullerenes through a lipid membrane: a molecular dynamics simulation study. *J. Phys. Chem. B* **2008**, *112* (7), 2078-2084.



APPENDICES

Supplementary data

Figure S1. List of RMSD and Rg with time profiles from MD simulations in vacuum for all systems

Figure S2. List of RMSD, RMSF and Rg with time profiles from MD simulations in water for all systems

Figure S3. RDF of Cl⁻ and comparison between RDF of Na-COO and Na-OH

Figure S4. Glycosidic torsion angle distributions for all systems

Figure S5. Comparison of torsion angle distribution between HA5 from our simulation and HA4 from NMR structure (2bvk.pdb)

Figure S6. List of RMSD with time profiles from MD simulations in membrane for HA1, benzene and limonene systems

Figure S7. Distances in z-axis of HA1, benzene and limonene at various force constant from SMD

Table S1. Average RMSD and Rg from simulations in gas phase and water

Table S2. Numbers of water, Na⁺ and Cl⁻ within the first solvation shell for all system

Table S3. H-bond occupancies of all systems

Table S4. Single point energies and torsion angles before and after optimization for each conformation of HA

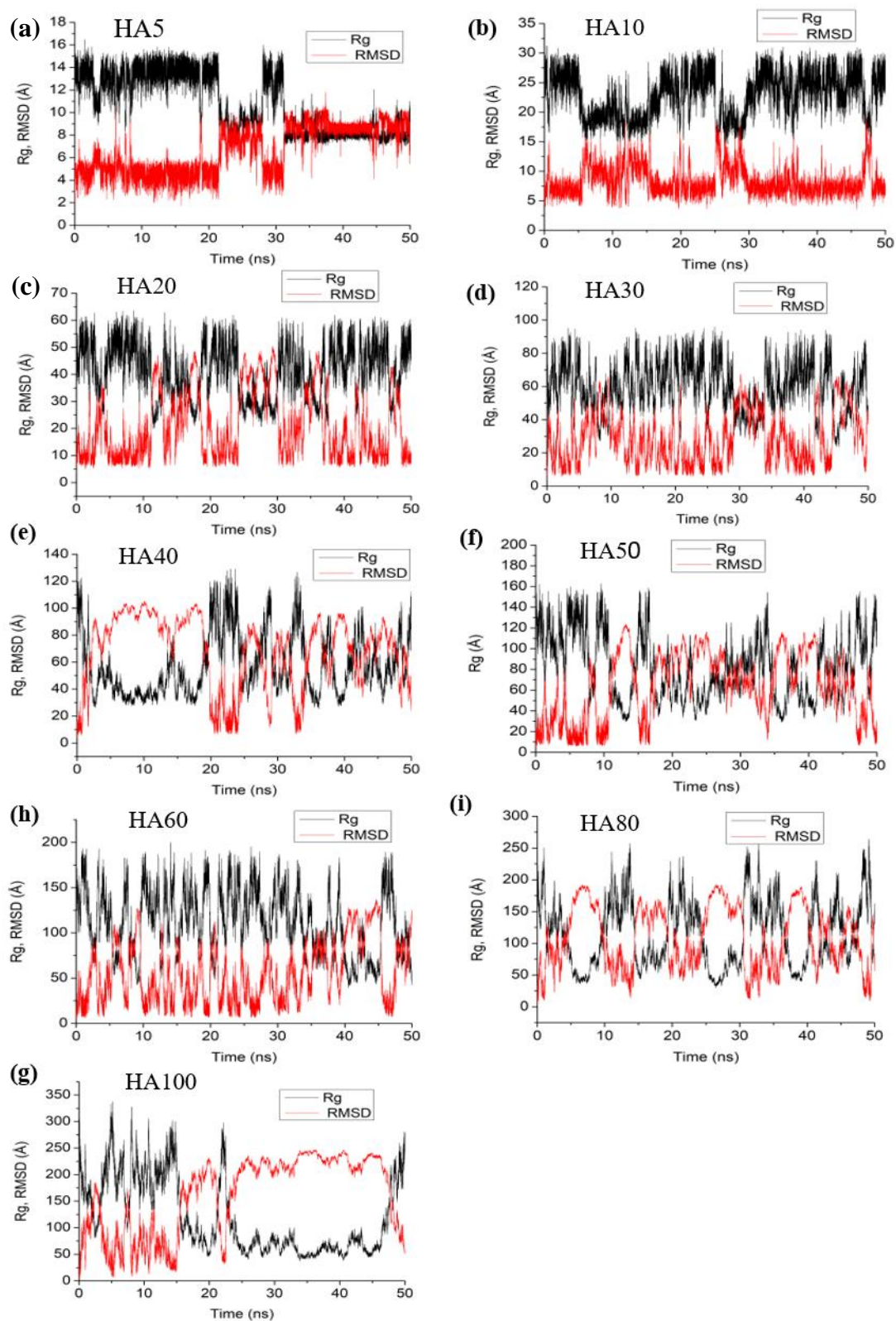
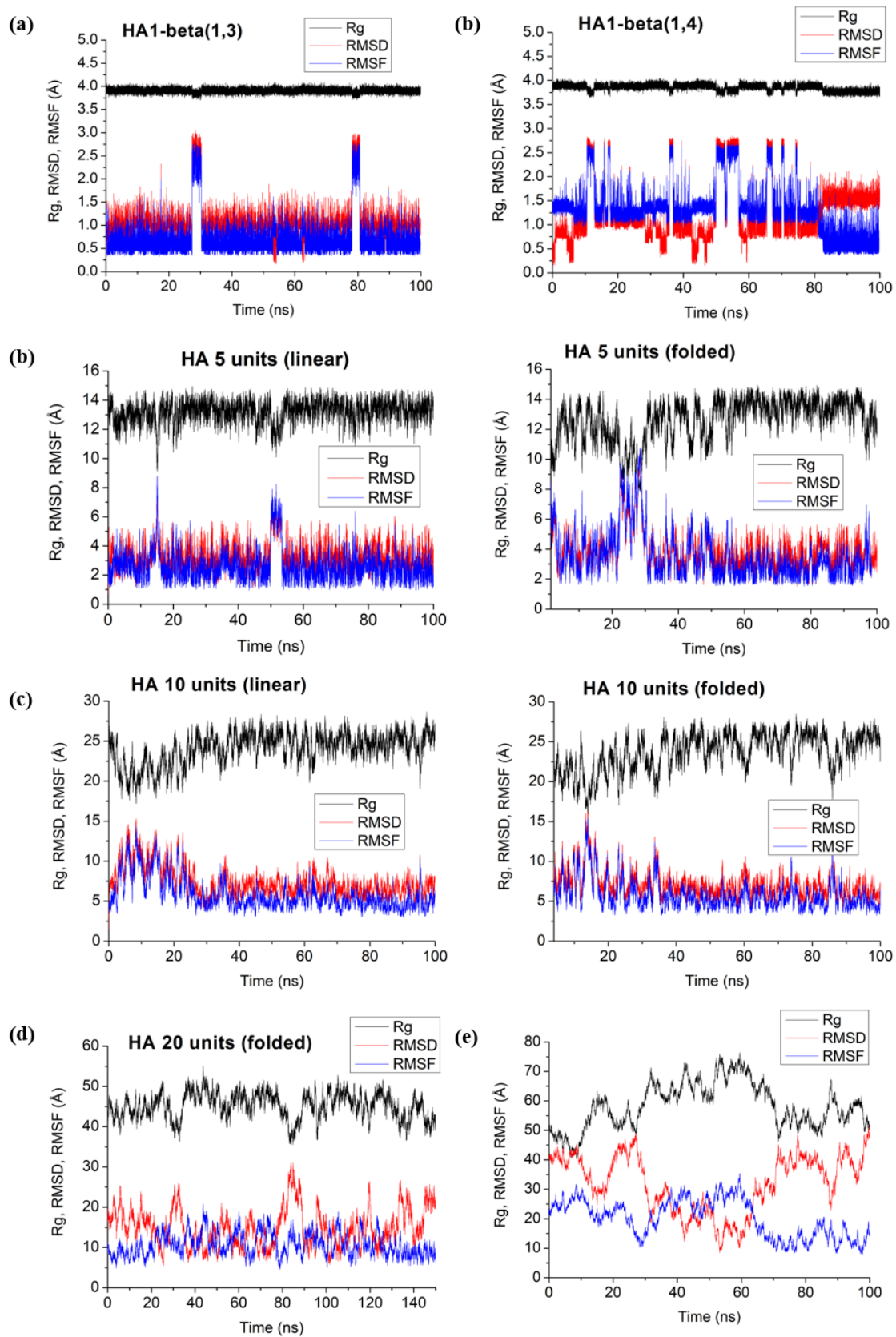


Figure S1. List of RMSD compared to initial structure (linear and Rg with time profiles from MD simulations in water for all systems, showed only one run from three runs. (a), (b), (c), (d), (e), (f), (g), (h) and (i) are HA 5, 10, 20, 30, 40, 50, 60, 80 and 100 units, respectively.



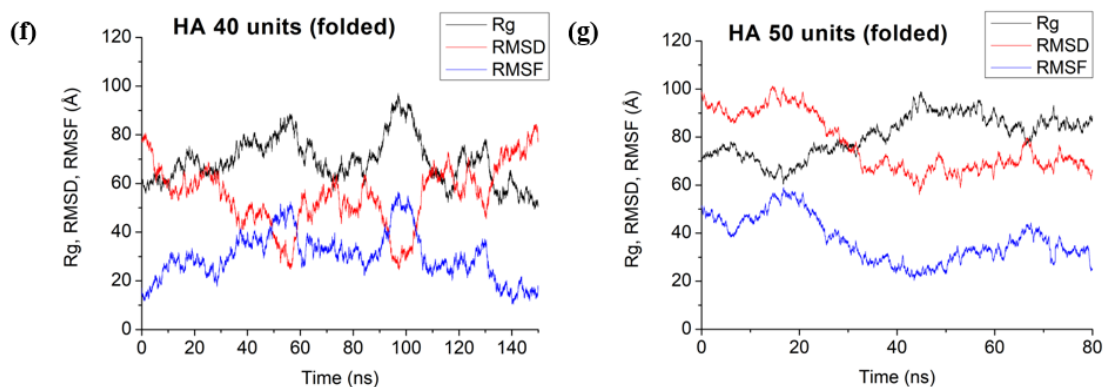


Figure S2. List of RMSD compared to linear structures, RMSF (compared to average structures) and Rg with time profiles from MD simulations in water for all systems, showed only one run from three runs. (a) HA 1 unit: $\beta(1,3)$ linkage (left) and $\beta(1,4)$ linkage (right) (b) HA 5 units that initial structures are linear structure (left) and folded structure (right) (c) HA 10 units that initial structures are linear structure (left) and folded structure (right) (d), (e), (f) and (g) are HA 20, 30, 40 and 50 units, respectively.

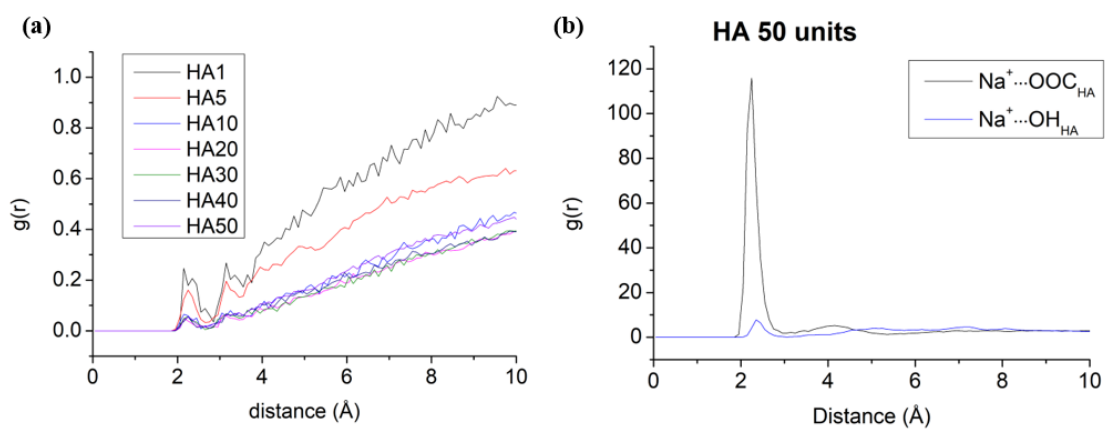
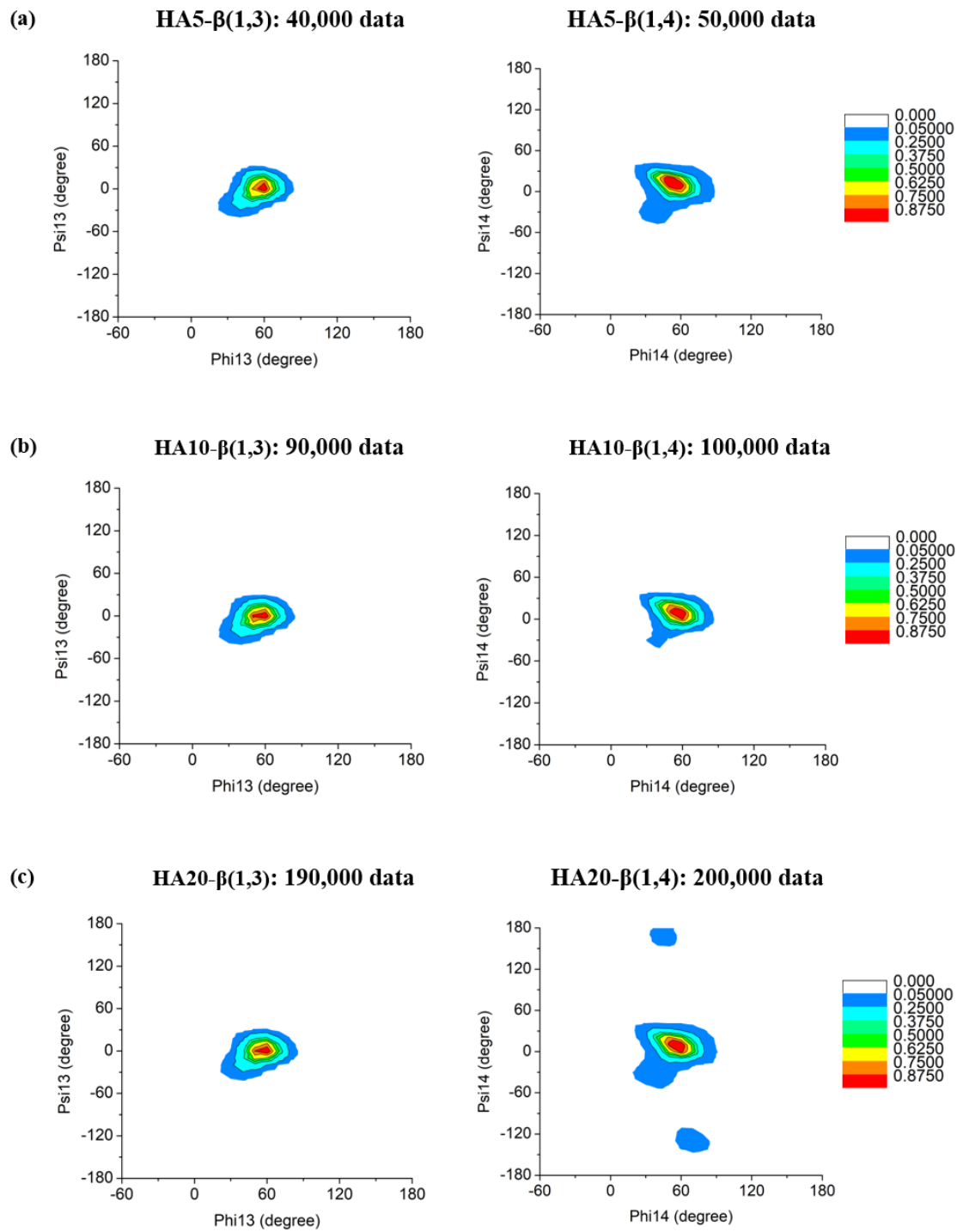


Figure S2. (a) The normalized RDF between Cl^- and whole HA for all systems and (b) comparison of RDF for $\text{Na}^+\cdots\text{COO}$ and $\text{Na}^+\cdots\text{OH}$ from HA 50 units



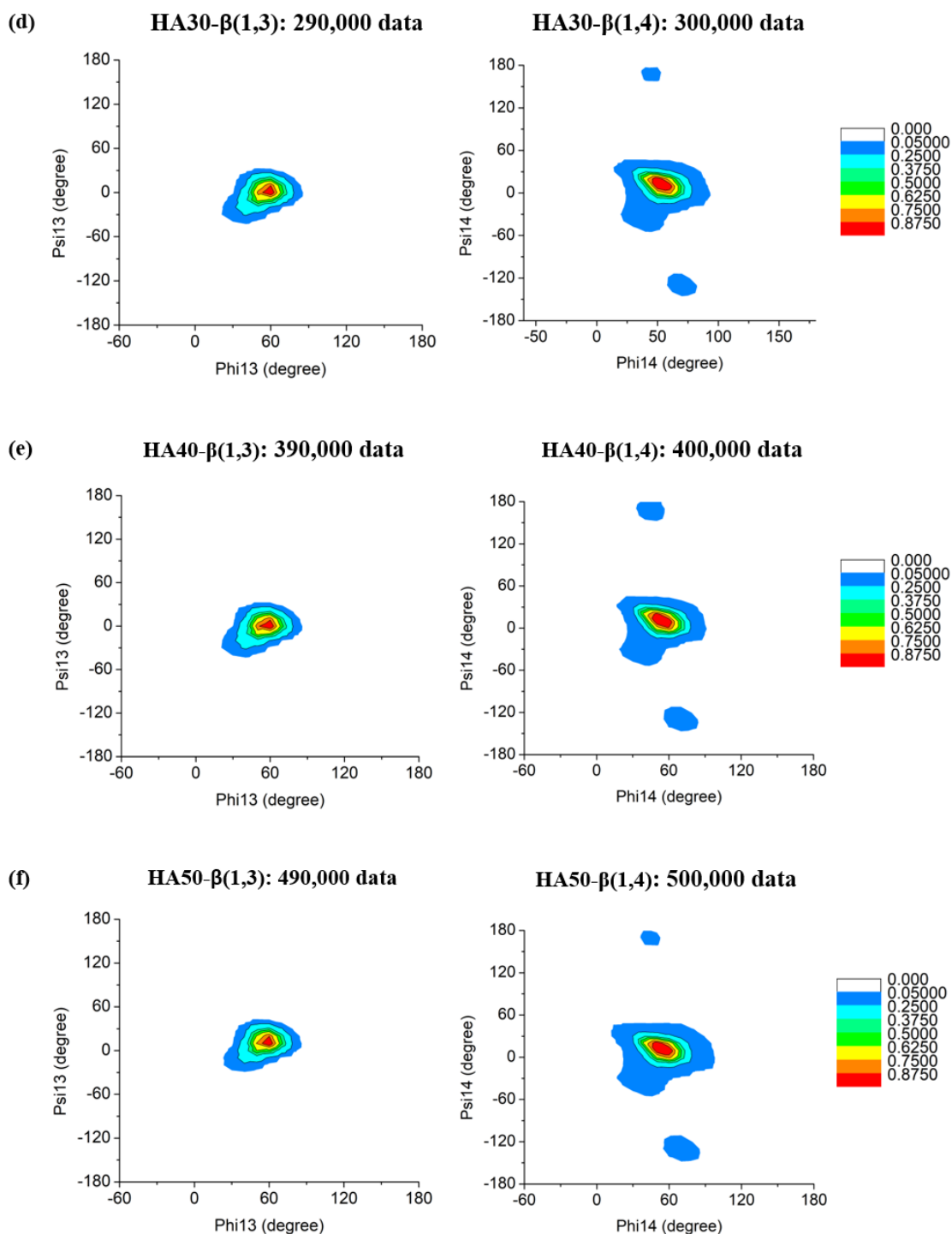


Figure S4. Glycosidic torsion angle distributions for all systems and the amount of data used to generate the contour plots. The data were extracted from last 20 ns of MD trajectories (10,000 snapshots) and one location of glycosidic bond can generate 10,000 data.

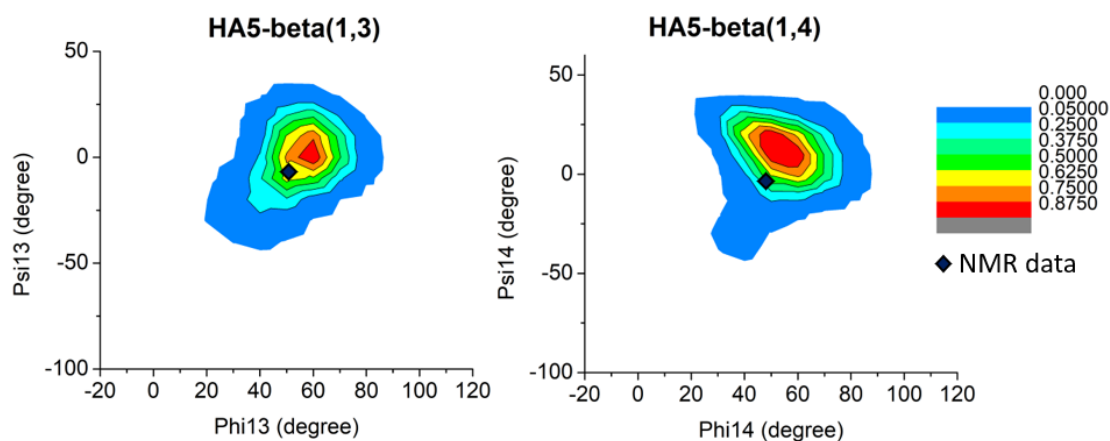


Figure S5. Comparison of torsion angle distribution between HA5 from our simulation and HA4 from NMR structure (2bvk.pdb)

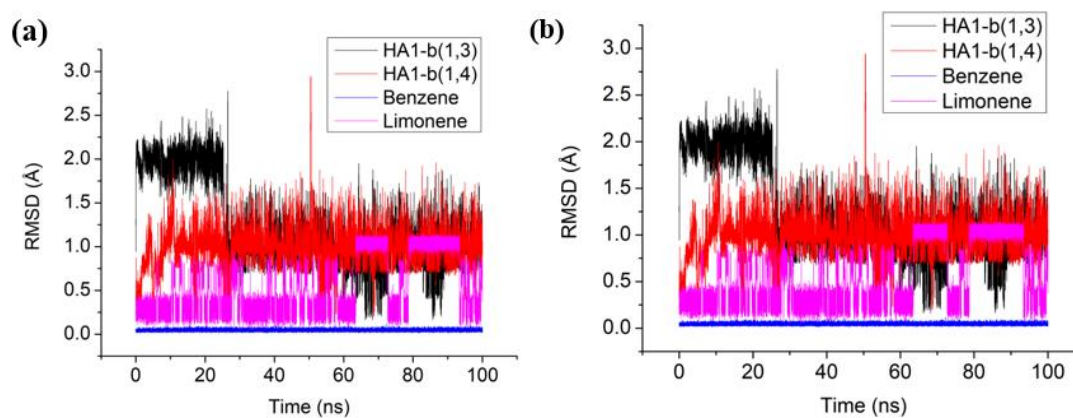


Figure S6. List of RMSD with time profiles from MD simulations in membrane for HA1, benzene and limonene systems where initial positions of molecules are (a) center of membrane and (b) membrane surface

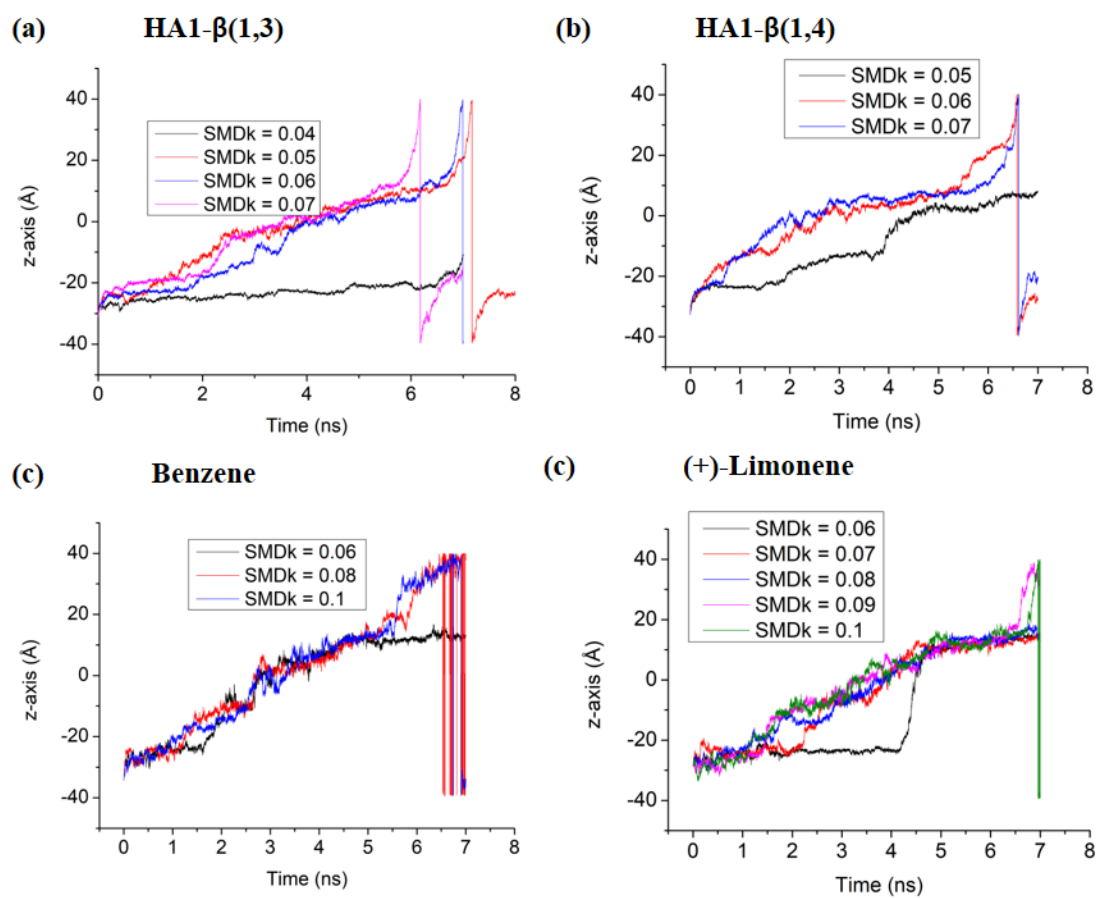


Figure S7. Distances in z-axis of (a) HA1-β(1,3), (b) HA1-β(1,4), (c) benzene and (d) limonene at various force constant ($\text{kcal/mol}/\text{Å}^2$) from SMD

Table S1. Average RMSD compared to linear structures and Rg (last 20 ns) from simulations in gas phase and water

Systems	Initial structures	Gas phase		Aqueous solution		
		Rg (Å)	RMSD (Å)	Rg (Å)	RMSD (Å)	RMSF (Å)
HA1	$\beta(1,3)$	-	-	3.91 ± 0.04	0.99 ± 0.15	0.65 ± 0.38
	$\beta(1,4)$	-	-	3.84 ± 0.07	1.38 ± 0.28	0.69 ± 0.25
HA5	Linear	10.78 ± 2.55	6.62 ± 2.08	13.33 ± 0.67	3.26 ± 0.81	2.37 ± 0.75
	Folded	-	-	13.24 ± 0.77	3.48 ± 0.76	3.04 ± 0.79
HA10	Linear	22.81 ± 3.68	8.32 ± 2.52	24.67 ± 1.44	6.62 ± 1.30	4.88 ± 1.16
	Folded	-	-	24.61 ± 1.72	6.44 ± 1.13	5.78 ± 1.62
HA20	Linear	41.11 ± 9.53	20.68 ± 11.84	-	-	-
	Folded	-	-	43.10 ± 3.19	17.06 ± 3.98	9.92 ± 2.05
HA30	Linear	58.28 ± 15.16	30.50 ± 16.14	-	-	-
	Folded	-	-	55.29 ± 3.94	38.34 ± 5.23	14.43 ± 3.47
HA40	Linear	65.26 ± 23.23	56.26 ± 27.86	-	-	-
	Folded	-	-	57.68 ± 5.59	70.93 ± 8.15	16.09 ± 2.59
HA50	Linear	79.86 ± 31.09	67.27 ± 34.00	-	-	-
	Folded	-	-	73.60 ± 5.51	85.34 ± 10.50	16.91 ± 3.36

Table S2. Numbers of water, Na⁺ and Cl⁻ within the first solvation shell per repeating unit for all system

Systems	Water	Free energy of solvation (kcal/mol)	Na ⁺	Cl ⁻	Ratio of Na ⁺	
					$\beta(1,3)$ site	$\beta(1,4)$ site
HA1- $\beta(1,3)$	31.5 \pm 2.87	-36.34 \pm 4.12	0.0426	0.0095	100%	-
HA1- $\beta(1,4)$	30.2 \pm 2.85	-35.79 \pm 4.35	0.0531	0.0112	-	100%
HA5	24.1 \pm 1.28	-30.30 \pm 1.92	0.1437	0.0074	30.4% \pm 12.4%	69.6% \pm 12.4%
HA10	23.1 \pm 0.82	-29.49 \pm 1.36	0.1667	0.0035	22.1% \pm 14.1%	77.9% \pm 14.1%
HA20	22.2 \pm 0.69	-29.21 \pm 0.99	0.1763	0.0020	29.3% \pm 17.7%	70.7% \pm 17.7%
HA30	21.7 \pm 0.8	-28.79 \pm 0.81	0.1573	0.0022	31.3% \pm 5.2%	68.7% \pm 5.2%
HA40	21.8 \pm 0.6	-28.85 \pm 0.70	0.1534	0.0022	34.2% \pm 9.7%	65.8% \pm 9.7%
HA50	21.2 \pm 0.84	-28.72 \pm 0.62	0.1394	0.0024	24.6% \pm 21.7%	75.4% \pm 21.7%

Table S3. Each of H-bond occupancies (%) for all systems and average net atomic charge at donor group of each H-bond from DFT optimization

Systems	O4-H...O5	O4-H...O=C	O3-H...O5	N-H...O=C	O3-H...O6	O6-H...O3	O6-H...O=C
HA1- β (1,3)	62.66 \pm 0.84	2.89 \pm 0.32	-	-	-	-	-
HA1- β (1,4)	-	-	37.63 \pm 17.36	8.62 \pm 6.21	6.47 \pm 2.51	2.22 \pm 0.27	0.39 \pm 0.45
HA5	58.55 \pm 1.20	1.61 \pm 0.13	34.20 \pm 5.36	30.03 \pm 1.00	2.28 \pm 0.36	1.36 \pm 0.10	0.42 \pm 0.57
HA10	58.52 \pm 3.43	14.42 \pm 11.99	39.34 \pm 2.90	38.38 \pm 15.01	4.72 \pm 1.80	2.67 \pm 0.90	2.37 \pm 0.91
HA20	61.01 \pm 0.81	5.02 \pm 4.54	39.92 \pm 1.45	22.63 \pm 15.51	6.65 \pm 5.03	4.23 \pm 3.41	7.65 \pm 4.75
HA30	59.60 \pm 0.29	2.14 \pm 0.60	36.00 \pm 2.23	30.15 \pm 1.68	2.21 \pm 0.30	1.56 \pm 0.11	2.08 \pm 1.56
HA40	61.36 \pm 0.39	2.15 \pm 0.40	39.31 \pm 1.14	29.74 \pm 1.90	2.37 \pm 0.38	1.73 \pm 0.10	2.43 \pm 0.92
HA50	60.74 \pm 0.52	1.88 \pm 0.02	38.84 \pm 0.27	30.93 \pm 0.29	1.78 \pm 0.09	1.58 \pm 0.02	1.11 \pm 0.27
Net atomic charge	O4 = -0.709 H = +0.447		O3 = -0.695 H = +0.429	N = -0.667 H = +0.413	O3 = -0.685 H = +0.428	O6 = -0.650 H = +0.426	O6 = -0.649 H = +0.429

Table S4. Single point energies and torsion angles before and after optimization for each conformation

Systems	runs	Single point energy (Hartree)		Torsion angle (ϕ, ψ)	
		Before optimization	After optimization	Before optimization	After optimization
1: $\beta(1,3)$	1st	-1504.20762	-1504.29461	(49.28°, -9.94°)	(38.17°, -33.02°)
	2nd	-1504.21023	-1504.29534	(46.49°, -8.82°)	(39.87°, -30.51°)
	3rd	-1504.20650	-1504.29451	(59.04°, 1.70°)	(39.25°, -34.08°)
	Average relative energy (kJ/mol)	0	0		
2: $\beta(1,4)$ at (ϕ, ψ) ~ (50°, 0°)	1st	-1504.19455	-1504.28206	(49.48°, -9.94°)	(38.16°, -33.01°)
	2nd	-1504.19603	-1504.28404	(45.91°, 13.01°)	(30.08°, -26.80°)
	3rd	-1504.20850	-1504.28375	(48.25°, -3.38°)	(30.51°, -27.70°)
	Average relative energy (kJ/mol)	+18.56 ± 26.42	+30.29 ± 2.39		
3: $\beta(1,4)$ at (ϕ, ψ) ~ (30°, -30°)	1st	-1504.19345	-1504.29559	(31.72°, -43.22°)	(32.55°, -19.48°)
	2nd	-1504.20900	-1504.29666	(33.48°, -39.88°)	(31.21°, -25.99°)
	3rd	-1504.19624	-1504.29707	(31.89°, -40.10°)	(31.54°, -25.66°)
	Average relative energy (kJ/mol)	+1.68 ± 18.25	-4.26 ± 2.34		
4: $\beta(1,4)$ at (ϕ, ψ) ~ (50°, 150°)	1st	-1504.20603	-1504.28592	(39.74°, 167.48°)	(35.75°, 169.55°)
	2nd	-1504.20455	-1504.28360	(40.00°, 167.66°)	(35.49°, 167.44°)
	3rd	-1504.20645	-1504.28520	(40.89°, 168.57°)	(35.78°, 169.82°)
	Average relative energy (kJ/mol)	+4.37 ± 16.08	+27.16 ± 3.62		
5: $\beta(1,4)$ at (ϕ, ψ) ~ (70°, -150°)	1st	-1504.18878	-1504.26883	(57.86°, -152.14°)	(55.54°, -151.37°)
	2nd	-1504.19956	-1504.27075	(59.82°, -155.29°)	(52.03°, -148.61°)
	3rd	-1504.18977	-1504.26618	(59.99°, -156.74°)	(54.28°, -150.91°)
	Average relative energy (kJ/mol)	+92.00 ± 36.73	+69.28 ± 5.14		

Publication from Current Trends in Polymer Science

Topic: Linear response to conformational collapse of a polymer chain with monomer-monomer interaction

Panyakorn Taweecat¹, Natthiti Chiangraeng², Piyarat Nimmanpipug², Pornthep Sompornpisut¹, R.B. Pandey³

¹*Center of Excellence in Computational Chemistry, Department of Chemistry, Chulalongkorn University, Bangkok 10330, Thailand*

²*Department of Chemistry and Cluster of Excellence on Biodiversity based Economic and Society (B.BES-CMU), Chiang Mai University, Chiang Mai 50200, Thailand*

³*Department of Physics and Astronomy, University of Southern Mississippi, Hattiesburg, MS 39406, USA*

Abstract: Conformational response of a polymer chain is examined as a function of monomer-monomer (attractive and repulsive) interactions. The multi-scale dynamics of the monomer and that of the center of mass of the polymer chain is found to depend strongly on the magnitude of attractive monomer-monomer interactions and less sensitive to their repulsive interactions. The scaling analysis of (a) the radius of gyration with the molecular weight and (b) that of the structure factor with the wave vector show: the polymer chain conforms to a random-coil with neutral to repulsive and weak attractive monomer-monomer interactions and collapses to a globular configuration on increasing the strength of attractive interaction. The radius of gyration of the polymer chain is found to decay slowly but linearly on reducing the repulsive monomer-monomer interactions and collapse on increasing attractive interactions.

Structure and dynamics of a polymer chain [1] is critical in assessing its utility in many applications, i.e. viscoelastic properties of a complex melt to morphological evolution of their self-assembly [2] with desirable pore sizes. For example, a biopolymer such as hyaluronic acid (HA) with a range of molecular weight

distribution provides elasticity to skin and fluidity in living organism and offers a great potential as a drug carrier and lubricant for preserving a healthy skin [3-5]. HA is a homo-polymer chain of disaccharide monomers, the global structure of which may depend of the interaction of monomers with the underlying matrix, temperature, etc. There has been enormous interest in understanding the structure of HA polymers via all-atom molecular dynamics simulations which are very insightful in understanding the small scale structural evolution [3-5]. Ingr et al [6] have analyzed the hyaluronan random coils in electrolyte solutions by Molecular Dynamics simulation based on randomly selecting pieces of an equilibrated oligosaccharide and found a ‘striking agreement with experimental data’ on the radius of gyration. While all atom molecular dynamics is very useful in understanding the structural details, it is difficult to analyze large HA polymers with realistic computing resources. For example, in an all-atom MD simulation of a HA polymer with 80 monomeric units, the fluctuation in radius of gyration is too large in a 50 ns simulation (see figure 1). In order to reduce the fluctuations and reach steady-state, it require enormous computing resources (months to a year of CPU) particularly for large polymer chains. Therefore, it would be desirable to explore conformation of such polymer chains by coarse-grained methods.

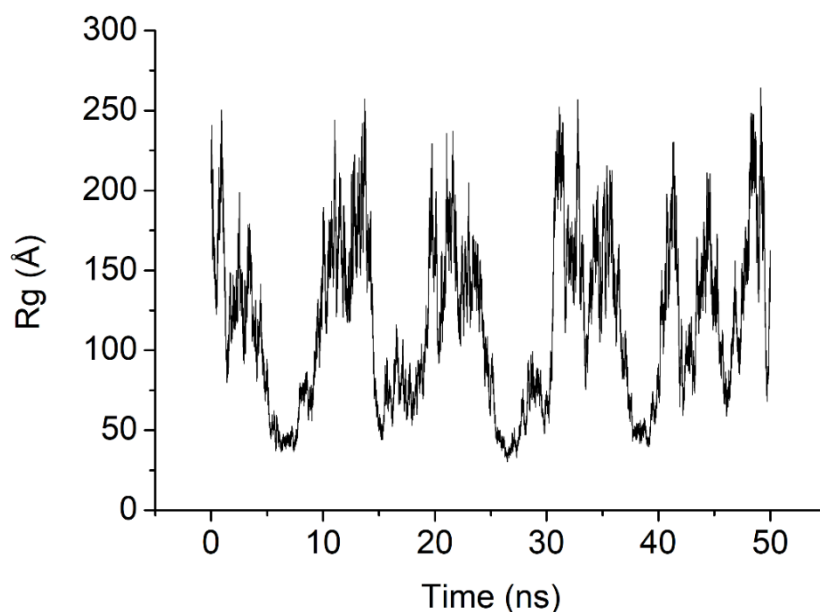


Figure 1. Variation of the radius of gyration with the time in all atom MD simulation.

The bond-fluctuation method for a coarse-grained polymer chain provides an efficient and effective tool to assess the dependence of the structural evolution of a polymer chain on its molecular weight [7]. It is worth pointing out that Manka, Nowicki, and Nowicka [8] have performed Monte Carlo simulations to examine the effectiveness of local moves on a cubic lattice. This method [8] is efficient to gain some insight into the conformations of a polymer chain, however, the local moves are adhoc and selecting their probability can be arbitrary. Efficiency and effectiveness of a discrete lattice with ample degrees of freedom can be captured by the bond-fluctuation method [7] used here. Instead of considering explicit solvent which is useful for examining specific systems [9], one may vary the monomer-monomer interaction in an effective medium approximation to assess general characteristics of a polymer chain first. Competition between the monomer-monomer interaction and thermal agitation generally controls the equilibrium structure of a polymer. Conformation of a coarse-grained polymer chain is examined as a function of monomer-monomer interaction by a bond-fluctuation Monte Carlo method.

A polymer chain is represented by a set of N nodes (monomers) tethered together by flexible bonds on a cubic lattice. A node (monomer) occupies a unit cubic cell and the bond length between consecutive nodes varies between 2 and $\sqrt{10}$ in unit of lattice constant. A node can move to neighboring cubic cells with ample degree of freedom (26 neighboring adjacent cells of a cube in a cubic lattice) for the connecting covalent bonds to fluctuate [7]. The polymer chain is initially placed in a random configuration. Each monomer interacts with surrounding monomers with Lennard-Jones potential within a range of interaction r_c i.e., the interaction potential between a monomer at a site i and another monomer at site j separated by a distance r_{ij} is given by

$$U_{ij} = -\epsilon \left[\left(\frac{\sigma}{r_{ij}} \right)^6 - \left(\frac{\sigma}{r_{ij}} \right)^{12} \right], r_{ij} \leq r_c \quad (1)$$

where ϵ is the interaction strength and $\sigma = 1$ in unit of lattice constant, $r_c = \sqrt{8}$. Each monomer performs its stochastic movements with the Metropolis algorithm in which a randomly selected monomer say at a site i is attempted to move to one of its randomly selected neighboring site j . The monomer is moved from site i to site j , subject to constraints imposed by the excluded volume and limits on the bond length,

with the Boltzmann probability $\exp(-\Delta E_{ij}/T)$, where $\Delta E_{ij} = E_j - E_i$ is the change in energy between its old (E_i) and new (E_j) configurations and T is the temperature in reduced unit of the Boltzmann constant (k_B). Attempts to move each node once define the unit Monte Carlo step (MCS) time. Simulations were performed for sufficiently long time steps (typically 10 million time steps) to make sure that system has reached its steady state equilibrium with a number of independent samples (100–5000) to estimate the average values of the physical quantities such as root mean square (RMS) displacement of the monomer and that of the center of mass of the chain, its radius of gyration (R_g), structure factor etc. A range of lattice sizes, $100^3 - 500^3$, are considered with chain lengths $N = 50 - 350$, at $T = 0.30$, for attractive $\epsilon = 0.00 - 0.75$ and repulsive (negative ϵ) monomer-monomer interactions.

Figure 2 shows a typical snapshot of the polymer chain with a range of monomer-monomer attractive interaction $\epsilon = 0.00 - 0.75$. As expected, for high attractive monomer-monomer interaction ($\epsilon = 0.60, 0.75$) the polymer chain collapses into a solid (globular) structure. While the chain retains its ideal open conformation in absence of interaction ($\epsilon = 0.00$), onset of the segmental consolidation seems to appear on introducing attractive monomer-monomer interaction.

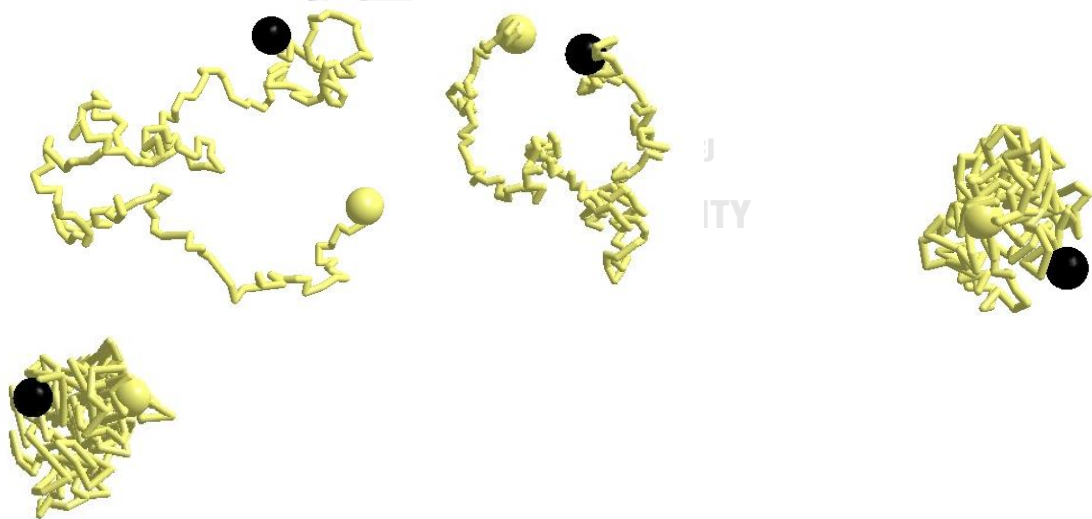


Figure 2. Snapshot of the polymer chain (black sphere represents the first node, the golden sphere represents the last monomer $N = 200$). Attractive interaction $\epsilon = 0.00, 0.50, 0.60, 0.75$ are used in snapshots from left to right.

How does the polymer chain move as its monomer performs its stochastic movements? The dynamics of individual monomer provides insight into the multi-scale characteristics of the polymer segments. The global dynamics of the polymer chain resulting from the collective movement of each monomer describes its overall conformational response. To examine short-to-long time dynamics, it is good to examine the dynamics of both, a monomer and the center of mass of the polymer chain. Figure 3 shows the variation of the RMS displacement of the monomer (R_n) and that of the center of mass of the chain (R_c) with the time steps (t) for an ideal chain (with only hard-core monomer-monomer interaction and that of a chain with attractive monomer-monomer interaction ($\epsilon = 0.60$)). The power-law dependence of the RMS displacement (R) with the time step (t) can be described by $R \propto t^\nu$ with an exponent ν which characterizes the type of dynamics (i.e. $\nu = 1/2$ for a typical diffusion). From the variations of the RMS displacement we see that the dynamics of a monomer differs dramatically from that of the center of mass of the chain in the short time and that the dynamics of both the monomer and the polymer chain converge to its diffusive motion in the asymptotic limit. Because of the covalent bonds constraints, the monomer moves with a slower dynamics in short time regime (i.e. $\nu \sim 1/3$) which is close to Rouse dynamics ($\nu \sim 1/4$) of an idea chain (well-known in polymer texts [1, 7]); note that for a chain on the lattice (with limited degrees of freedom) this estimate is not bad with only excluded volume interaction ($\epsilon = 0.00$). The magnitude of the exponent ν of the monomer increases with the time steps before converging approximately to its diffusive value. Note that long-time simulations are needed to reach such asymptotic dynamics. The dynamics of both, the monomer and that of its center of mass changes on increasing the monomer-monomer interaction. The polymer chain continues to perform its asymptotic diffusive motion with repulsive and lower attractive monomer-monomer interactions. The dynamics of the chain becomes sub-diffusive at high attractive interaction (i.e., $\epsilon = 0.75$).

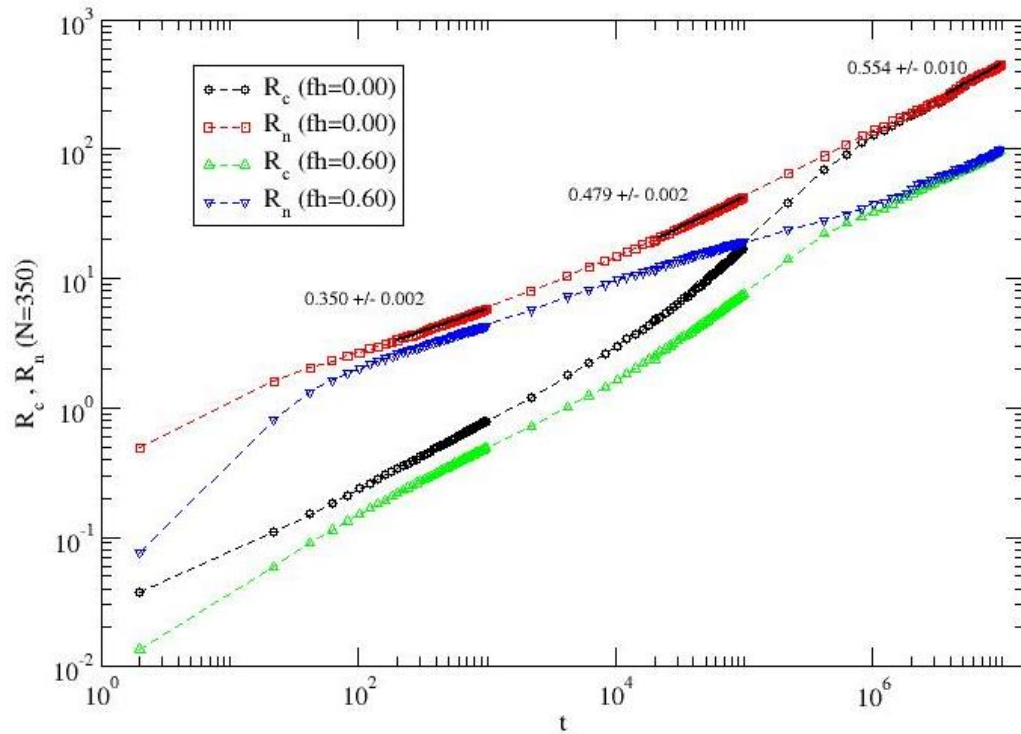


Figure 3. Root mean square (RMS) displacement of the center node (R_n) and that of the center of mass (R_c) of the polymer chain versus time steps (MCS) for a polymer chain of length $N=350$ with ϵ (fh) = 0.00, 0.60. Simulation box of size 500^3 is used with 100 independent samples.

As pointed out above, the simulation is carried out for a sufficiently long time steps for chain to reach its steady-state equilibrium (verified from the analysis of its radius of gyration R_g with the time steps). Variation of the equilibrium radius of gyration of the polymer chain with the molecular weight (N) is presented in figure 4 on a log-log scale for various monomer-monomer interactions (neutral to attractive). For a power-law scaling $R_g \propto N^\gamma$, one can easily evaluate the exponent γ which is about 0.58 with repulsive, neutral, and low attractive monomer-monomer interactions. The magnitude of the power-law exponent begins to decrease (appear to become non-linear with larger chains) on increasing the attractive monomer-monomer interaction ($\epsilon = 0.60, 0.75$) as the conformation of the chain collapses.

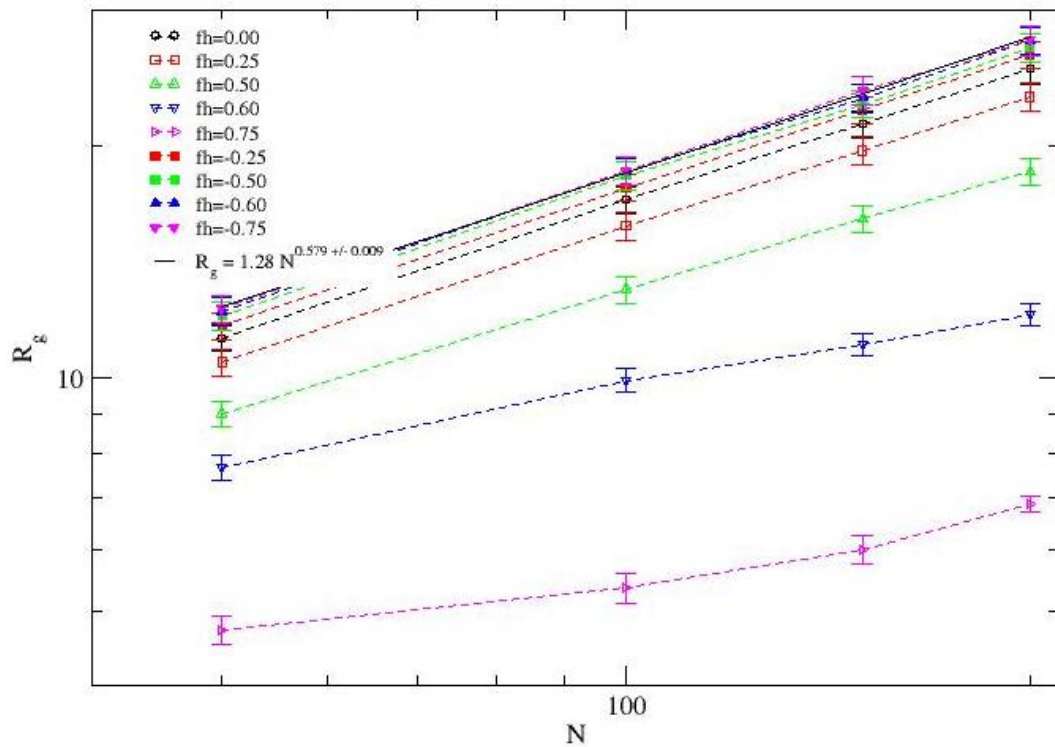


Figure 4. Average radius of gyration with the chain length (N) on a log-log scale. Sample size 100^3 – 270^3 are used with 100 independent samples.

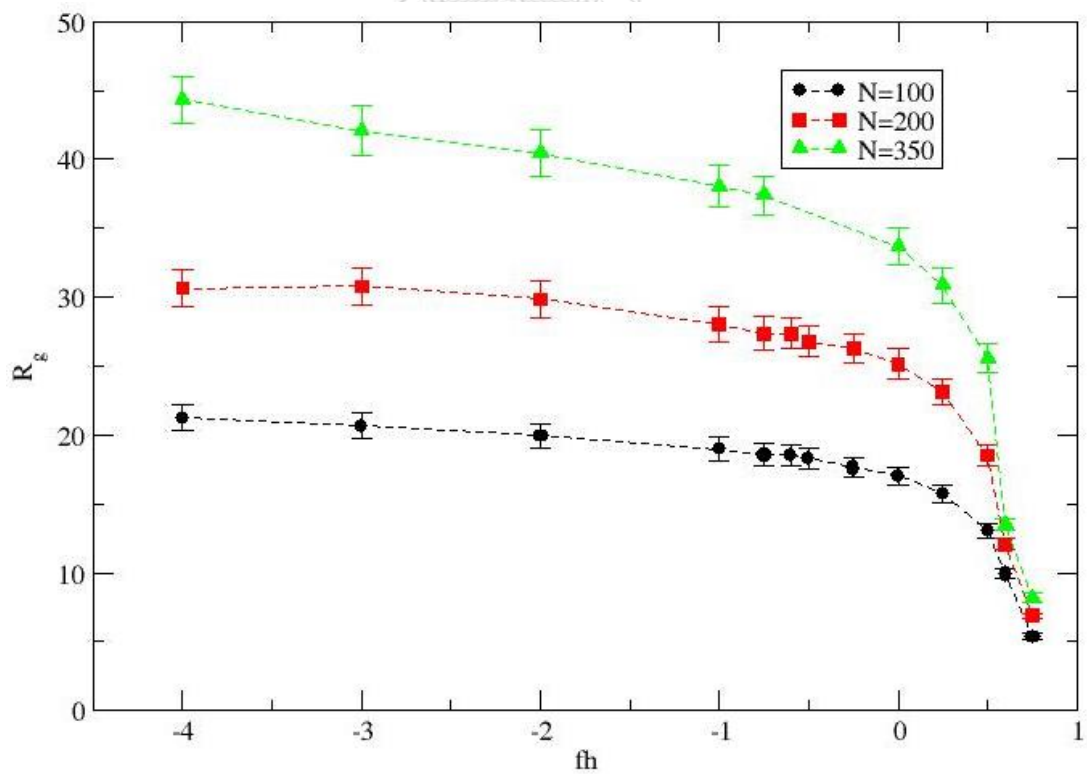


Figure 5. Variation of the radius of gyration of the polymer chain with the monomer-monomer interaction $\epsilon = -4.00$ to -0.75 .

Obviously, the monomer-monomer interactions affect the average conformation of the polymer chain. To address this question, we have analyzed the variation of the radius of gyration of the polymer chain for a wide range of attractive and repulsive monomer-monomer interactions ($\epsilon = -4.00$ to 0.75) as presented in figure 5. The radius of gyration decreases slowly on reducing the repulsive interaction ($\epsilon = -4.00$ to 0.00) followed by a rapid decay with on increasing the attractive interaction in a narrow range. It is difficult to say whether collapse of the polymer chain stay continuous or becomes abrupt (1st order, discontinuous) with the interaction. Nevertheless, it does give an idea how to control the size of the chain by selecting appropriate monomer or effective solvent that leads to such monomer-monomer interactions.

The overall spread of the polymer chain can also be analyzed by examining the structure factor

$$S(q) = \left\langle \frac{1}{N} \left| \sum_{j=1}^N e^{-i\vec{q} \cdot \vec{r}_j} \right|^2 \right\rangle_{|\vec{q}|} \quad (2)$$

where r_j is the position of each monomer and $|q| = 2\pi/\lambda$ is the wave vector of wavelength λ . Using a power-law scaling of the structure factor with the wave vector, i.e.,

$$S(q) \propto q^{-1/\gamma}, \quad (3)$$

one may be able to estimate effective dimension D of the monomer distribution, $N \propto \lambda^D$ where $D \sim 1/\gamma$. Variation of the structure factor S with the wavelength λ for the polymer chain of length $N=200$ is presented in figure 6 for a range of neutral to attractive monomer-monomer interactions. Fitting the data with wavelength comparable to radius of gyration clearly shows how the monomers consolidate on increasing the attractive interaction, from a random coil chain ($D \sim 1.79$ for $\epsilon = 0.00, 0.25$) to a globular solid ball ($D \sim 3$ for $\epsilon = 0.60, 0.70$).

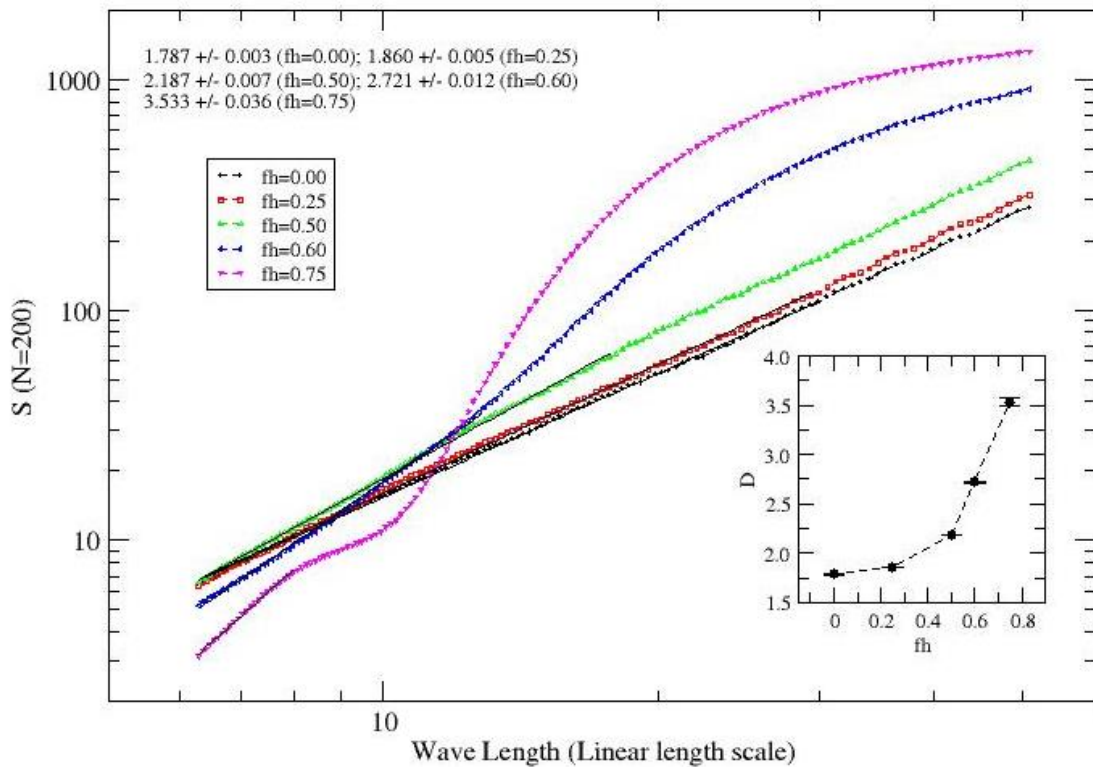


Figure 6. Variation of the structure factor S with the wave length of the polymer chain of size $N = 200$ with $\epsilon = 0.00 - 0.75$. Inset is the variation of the effective dimension of the polymer chain with the monomer-monomer interaction $\epsilon = fh$.

In summary, the structural variation of the polymer chain conformation with the monomer-monomer attractive and repulsive interactions is studied via (a) scaling of the radius of gyration with the molecular weight and (b) that of the structure factor of the chain with the wave vector. The average conformation of the chain is less sensitive to repulsive monomers where the radius of gyration decreases slowly on reducing the interaction strength. Dynamics of monomer and that of the center of mass of the chain depends strongly on the strength of attractive monomer-monomer interaction with diffusion to subdiffusion in asymptotic regimes with low to high values of interaction. Multi-scale (small to large scale) dynamics of the monomer is also sensitive to interaction strength. The polymer chain conforms to a random-coil conformation with neutral to weak attractive monomer-monomer interaction but collapses to a globular structure on increasing the attractive interaction. Scaling of the radius of gyration and structure factor of the chain is useful in quantifying the

conformational spread of the polymer chain. We hope this analysis may help in identifying the desirable polymer chain conformations by selecting appropriate monomers.

Acknowledgement: This research has been supported by the Ratchadaphiseksomphot Endowment Fund, Chulalongkorn University to PS. Support from Chulalongkorn University for the visiting professorship is gratefully acknowledged by RBP. The authors acknowledge HPC at The University of Southern Mississippi supported by the National Science Foundation under the Major Research Instrumentation (MRI) program via Grant # ACI 1626217.

References:

1. 'Polymer Physics' by M. Rubinstein and Ralph H. Colby, Oxford University Press; 1 edition (2003)
2. N. Chiangraen, V. S. Lee and P. Nimmanpipung, Coarse-grained modeling and temperature effect on the morphology of PS-b-PI copolymer, *Polymers* 11, 1008 (2019).
3. S. Furlan, G. La Penna, A. Perico, and A. Cesaro, Hyaluronic chain conformation and dynamics, *Carbohydrate Research* 340, 959-970 (2005)
4. J. Siodmiak et al. Molecular dynamics analysis of hyaluronic acid and phospholipid interaction in tribological surgical adjuvant design for osteoarthritis, *Molecules* 22, 1436 (2017).
5. P. Smith, R.M. Ziolek, E. Gazzarrini, D.M. Owen, and C.D. Lorenz, On the interaction of hyaluronic acid with synovial fluid lipid membranes, *Phys. Chem. Chem. Phys.* 21, 9485-9857 (2019).
6. M. Ingr, E. Kutalkova, and J. Hrnčirik, Hyaluronan random coils in electrolyte solutions – a molecular dynamics study, *Carbohydrate Polymers* 170, 289-295 (2017).
7. 'Monte Carlo and Molecular Dynamics Simulations in Polymer Science' edited by Binder K, Oxford University Press (1995).
8. A. Manka, W. Nowicki, and G. Nowicka, Monte Carlo simulations of apolymer chain conformation. The effectiveness of local moves algorithms and estimation of entropy, *J. Mol. Model* 19, 3659-3670 (2013).
9. V.S. Rathee, H. Sidky, B.J. Sikora, and J.K. Whitmer, Explicit ion effects on the charge and conformation of weak polyelectrolyte

VITA

NAME Mr. Panyakorn Taweecat

DATE OF BIRTH 21 July 1994

PLACE OF BIRTH Chonburi, Thailand

INSTITUTIONS ATTENDED Bachelor Degree of Science in Chemistry, Chulalongkorn University, Bangkok, Thailand

HOME ADDRESS 83-85-87, Soi Lang Wat Hua Lamphong, Sub Road, Kwang Sri Praya, Khet Bangrak, Bangkok, 10500

PUBLICATION

1. Worawalai, W.; Doungwichitkul, T.; Rangubpit, W.; Taweecat, P.; Sompornpisut, P.; Phuwapraisirisan, P., Furofuran lignans as a new series of antidiabetic agents exerting α -glucosidase inhibition and radical scavenging: Semisynthesis, kinetic study and molecular modeling. *Bioorganic chemistry* 2019, 87, 783-793.
2. Taweecat, P.; Chiangraeng, N.; Nimmanpipug, P.; Sompornpisut, P.; Pandey, R. B. Linear response to conformational collapse of a polymer chain with monomer-monomer interaction. *Current Trends in Polymer Science* 2019, 65, 59-65.
3. Taweecat, P.; Pandey, R. B.; Sompornpisut, P. Conformation, flexibility and hydration of hyaluronic acid by molecular dynamics simulations *Carbohydrate Research* 2020, 493, 108026.

AWARD RECEIVED Oral presentation in ANSCSE 22